

**SYNTHESIS OF FUNCTIONALIZED GRAPHENE/  
COPPER OXIDE (CuO) NANOCOMPOSITES  
AND THEIR CATALYTIC ACTIVITY**

**NORAZRIENA BINTI YUSOFF**

**DISSERTATION SUBMITTED IN FULFILLMENT OF  
THE REQUIREMENT FOR THE DEGREE OF  
MASTER OF SCIENCE**

**DEPARTMENT OF PHYSICS  
FACULTY OF SCIENCE  
UNIVERSITY OF MALAYA  
KUALA LUMPUR  
2013**

UNIVERSITI MALAYA

**ORIGINAL LITERARY WORK DECLARATION**

Name of Candidate: **Norazriena Binti Yusoff** (I.C/Passport No: **871017-05-5248**)

Registration/Matric No: **SGR100102**

Name of Degree: **Master of Science (Dissertation)**

Title of Project ~~Paper/Research Report/Dissertation/Thesis~~ ("this Work"):

**SYNTHESIS OF FUNCTIONALIZED GRAPHENE/COPPER OXIDE (CuO)  
NANOCOMPOSITES AND THEIR CATALYTIC ACTIVITY**

Field of Study: **Advanced Materials**

I do solemnly and sincerely declare that:

- (1) I am the sole author/writer of this Work;
- (2) This Work is original;
- (3) Any use of any work in which copyright exists was done by way of fair dealing and for permitted purposes and any excerpt or extract from, or reference to or reproduction of any copyright work has been disclosed expressly and sufficiently and the title of the Work and its authorship have been acknowledged in this Work;
- (4) I do not have any actual knowledge nor do I ought reasonably to know that the making of this work constitutes an infringement of any copyright work;
- (5) I hereby assign all and every rights in the copyright to this Work to the University of Malaya ("UM"), who henceforth shall be owner of the copyright in this Work and that any reproduction or use in any form or by any means whatsoever is prohibited without the written consent of UM having been first had and obtained;
- (6) I am fully aware that if in the course of making this Work I have infringed any copyright whether intentionally or otherwise, I may be subject to legal action or any other action as may be determined by UM.

Candidate's Signature:

Date:

Subscribed and solemnly declared before,

Witness's Signature:

Date:

Name: **Dr. Huang Nay Ming**

Designation: **Senior Lecturer**

## **ABSTRACT**

Graphene sheets incorporated with inorganic metal oxides are emerging as a new class of exciting materials. Nanostructured CuO-based materials have been widely investigated because they are inexpensive, non-toxic, and have unique features such as narrow band gap and high solar absorbency. The focus of this research is to fabricate and characterize copper oxide (CuO) nanostructures, functionalized graphene oxide (FGO) and functionalized graphene/copper oxide (FG/CuO) nanocomposite as well as a study of their catalytic activity. Such a study is important in order to predict the suitability of the FG/CuO nanocomposite as a catalyst for the treatment of wastewater contained dyes. Firstly, CuO nanostructures were synthesized using hydrothermal, reflux, ultrasonication and two steps heating process. The as-prepared CuO, which were characterized by Field Emission Scanning Electron Microscopy (FESEM) and Transmission Electron Microscopy (TEM) shows that nanorods, nanoflowers and nanofibrils had been formed. It was found that in the presence of hydrogen peroxide and rod-like CuO synthesized by hydrothermal method, the degradation rate of methylene blue (MB) reached up to 87.5 % after irradiation for 10 hours. This is the highest among all the methods due to the highest crystallinity as observed in X-ray diffraction and well organized structure with high capacity of particles that ensure more active surface site for the degradation of MB. Next, GO was fabricated using simplified Hummers' method, which was silanized with N-(trimethoxysilylpropyl) ethylenediamine triacetic acid (EDTA-silane) in order to form FGO. Finally, FG wrapped CuO particles hybrid materials were synthesized through hydrothermal method. A series of nanocomposites with varying amount of FGO was prepared to study the morphological changes of CuO crystals on the FG sheets and the effects on the catalytic performance. As seen from the FESEM and TEM images, FG sheets had been decorated with aggregation of needle-like CuO with average size of 20 nm. The

average size of CuO reduced to 15 nm and less than 15 nm with addition of 20 and 30 mg of FGO. The distribution of CuO nanoparticles were also become more uniform as the amount of FGO is increased due to more nucleation sites on the FGO sheets that can be accommodated by  $\text{Cu}^{2+}$  ions, simultaneously hindering the agglomeration of nanoparticles. The micro Raman spectrum clearly shows the blue-shift of G peak position from  $1600\text{ cm}^{-1}$  for nanocomposites with 2 mg FGO to  $1605\text{ cm}^{-1}$  and  $1608\text{ cm}^{-1}$  as the amount of FGO was increased to 20 mg and 30 mg, respectively. This result confirms that there is a strong interaction between CuO and FG as the interaction will be stronger in line with the shift towards higher wavenumbers. The catalytic activity of the nanocomposites was also ascending as higher amount of FGO was used. The sample with 2 mg of FGO shows 87.5 % of dye decomposed after 10 hours. While the degradation percentage is 95.08 % and 99.06 % for nanocomposites with 20 mg and 30 mg FGO, respectively. In summary, the mass ratio of FG:CuO and the electronic interaction between them acted as one of the important parameters that control the CuO particle size and catalytic performance, respectively.

## **ABSTRAK**

Lembaran graphene yang digabungkan dengan oksida logam bukan organik muncul sebagai bahan baru yang menarik dalam kelasnya yang tersendiri. Kuprum oksida (CuO) berstruktur nano telah dikaji secara meluas kerana ia tidak mahal, bukan toksik, dan mempunyai ciri-ciri unik seperti selar jalur yang sempit dan kadar resapan solar yang tinggi. Fokus kajian ini adalah bagi menghasilkan dan mencirikan kuprum oksida (CuO) nanostruktur, oksida graphene terfungsi (FGO) dan graphene terfungsi / kuprum oksida (FG / CuO) komposit nano serta mengkaji aktiviti pemangkin. Kajian ini adalah penting untuk meramal kesesuaian komposit nano FG / CuO sebagai pemangkin bagi rawatan sisa air berwarna. Dalam langkah pertama, CuO berstruktur nano disintesis dengan menggunakan hidroterma, refluks, ultrasonikasi dan proses pemanasan dua langkah. Hasil CuO yang telah dicirikan oleh Mikroskopi Elektron Daya Imbasan (FESEM) dan Mikroskopi Penghantaran Elektron (TEM) menunjukkan bahawa rod, bunga dan fiber yang bersaiz nano telah terbentuk. Kadar degradasi metilena biru (MB) mencecah sehingga 87.5 % selepas penyinaran selama 10 jam dengan kehadiran hidrogen peroksida dan CuO berbentuk rod yang terhasil melalui kaedah hidroterma. Ini merupakan yang tertinggi diantara semua kaedah lain kerana penghabluran yang tinggi sepertimana yang dibukti melalui analisis pembelauan sinar-X dan seragam serta struktur terancang dengan kapasiti zarah yang tinggi bagi menyediakan tapak permukaan yang lebih aktif untuk kemusnahan MB. Kemudian, oksida graphene (GO) dihasilkan menggunakan kaedah ringkasan Hummers yang seterusnya disilanasikan dengan asid N-(trimethoxysilylpropyl) etilenadamina triasetik (EDTA-silane) untuk mendapatkan FGO. Seterusnya, FG dibaluti dengan zarah CuO yang disintesis melalui kaedah hidrotermal. Satu siri komposit bersaiz nano dengan jumlah FGO yang berbeza telah dihasilkan untuk mengkaji perubahan morfologi hablur CuO pada lembaran FG dan bagaimana ia mempengaruhi prestasinya sebagai pemangkin. Seperti yang dapat

dilihat dari imej-imej FESEM dan TEM, helaian FG telah dihiasi dengan CuO berbentuk jarum dengan saiz purata 20 nm. Purata saiz zarah CuO mula berkurang kepada 15 nm dan kurang daripada 15 nm apabila FGO ditambah sebanyak 20 dan 30 mg. Taburan zarah CuO juga menjadi lebih seragam apabila jumlah FGO meningkat disebabkan lebih banyak tapak penukleusan disediakan oleh FGO yang boleh menempatkan ion  $\text{Cu}^{2+}$ , pada masa yang sama menghalang pengumpulan partikel nano. Spektrum Raman mikro jelas menunjukkan peralihan kedudukan puncak G dari  $1600 \text{ cm}^{-1}$  bagi komposit nano dengan 2 mg FGO kepada  $1605 \text{ cm}^{-1}$  dan  $1608 \text{ cm}^{-1}$  apabila jumlah FGO peningkatan kepada 20 mg dan 30 mg. Analisis ini mengesahkan bahawa terdapat interaksi kuat antara CuO dan FG dan interaksi ini akan menjadi lebih kuat sejajar dengan peralihan ke arah nombor vektor yang lebih tinggi. Aktiviti pemangkin bagi komposit nano juga meningkat apabila jumlah FGO bertambah. Sampel dengan 2 mg FGO diperhatikan menunjukkan 87.5 % penurunan pewarna selepas 10 jam. Peratusan penurunan adalah 95.08 % dan 99.06 % bagi komposit nano dengan masing-masing mengandungi 20 mg dan 30 mg FGO. Secara ringkasnya, jisim nisbah FG:CuO dapat bertindak sebagai salah satu parameter penting yang mengawal saiz zarah CuO dan juga prestasi sebagai pemangkin. Interaksi elektronik antara zarah CuO dan lembaran FG memainkan peranan yang penting dalam pemangkinan.

## **ACKNOWLEDGEMENT**

Alhamdulillah. Thanks to Allah for giving me the opportunity to complete my dissertation and giving me some strength and patience to face off all the challenges and difficulties throughout this journey. Finally, two years of hard work have come to an end now with this thesis is the evidence of all the effort I had put into for accomplishing the goal of my research. This thesis would not have been possible unless by the support and guidance from several peoples around me.

Firstly, I owe my deepest gratitude to my supervisor, Dr. Huang Nay Ming, for his guidance, encouragement and opportunities to learn something new in order to develop an understanding of the project throughout my years under his supervision. Infinite thanks for lending me some of your precious time to teach me from the beginning without feeling tired as I am still new in this field. It is my honor to work with such a great and inspiring teacher and I will not reach to this stage now without your help.

Next, I would like to show my gratitude to all my group members at Low Dimensional Materials Research Centre especially Ms. Marlinda AR Rahman, Ms. Fadhilah, Mrs. Mazlinda Zainy, Ms. Betty Chang and Dr. Vijay for their helpful discussion, guidance and kindness teach and sharing knowledge with me as it has added a lot of value to my work. Your cooperation, contribution and extended valuable assistance really mean a lot to me and will never forget.

I would like to thank other faculty members including Mr. Mohammad Bin Aruf, Mrs. Norlela, Mr. Amir, Mrs. Zurina, Mrs. Saedah, Ms. Aidahani, and Mrs. Endang for providing support and technical services throughout this research. Your kindly help really makes my journey to finish up this research become smooth.

I gratefully acknowledge the financial support from the University of Malaya for the postgraduate research fund (PV039 2011A) which help me a lot in preparing all the stuffs needed to do this research. Also I would like to thank Faculty of Science, UM for providing the financial support for attending the national conference. Without all these financial and moral supports, I believed this research cannot be done successfully.

Last but not the least, I wish to express my warm and sincere thanks to my mother; Che Salia Bt. Yaakob, my father; Yusoff Bin Zakaria and my beloved husband; Mohd. Asraf Bin Aris for your understanding, patience, endless support and believing in me whenever I felt gave up and lost hope. Infinite thanks for taking care of our little baby; Hazim Husaini whenever I'm busy with my research. And most importantly thanks a lot for your love. This dissertation is a gift for you as a sign of appreciation of what you have sacrificed for me.

## TABLE OF CONTENTS

<b>Declaration</b> .....	<b>ii</b>
<b>Abstract</b> .....	<b>iii</b>
<b>Abstrak</b> .....	<b>v</b>
<b>Acknowledgments</b> .....	<b>vii</b>
<b>Table of contents</b> .....	<b>ix</b>
<b>List of figures</b> .....	<b>xiii</b>
<b>List of tables</b> .....	<b>xvii</b>
<b>List of abbreviations</b> .....	<b>xviii</b>
<b>List of publications</b> .....	<b>xix</b>
<b>Chapter 1: Introduction</b>	
1.1 Overview of research studies .....	<b>1</b>
1.2 Focus and objectives of this research .....	<b>4</b>
1.3 Outline of the dissertation .....	<b>6</b>
<b>Chapter 2: Literature review</b>	
2.1 Introduction .....	<b>8</b>
2.2 Carbon materials: An introduction .....	<b>8</b>
2.3 A journey from GO to graphene .....	<b>10</b>
2.3.1 Review on several methods of preparing graphene .....	<b>15</b>
2.3.2 Properties and application of graphene .....	<b>18</b>
2.3.3 Functionalized graphene (FG) .....	<b>20</b>
2.4 The introduction to CuO .....	<b>21</b>
2.4.1 Properties and application of CuO .....	<b>22</b>

2.5	Reviews on several preparation techniques for synthesis of graphene /CuO nanocomposite .....	23
2.5.1	Hydrothermal method .....	24
2.5.2	Solvothermal method .....	24
2.5.3	Microwave-assisted method .....	25

### **Chapter 3: Experimental methods**

3.1	Introduction .....	27
3.2	Material .....	28
3.3	Sample preparation .....	29
3.3.1	Different ways of preparing CuO with different morphologies .....	29
3.3.1.1	Preparation of CuO using reflux method .....	30
3.3.1.2	Preparation of CuO using the hydrothermal method .....	31
3.3.1.3	Preparation of CuO using ultrasonication method .....	32
3.3.1.4	Preparation of CuO using the two steps heating method .....	33
3.3.2	Preparation of GO and FGO .....	34
3.3.2.1	Synthesis of GO using simplified Hummers' method .....	34
3.3.2.2	Synthesis of FGO via silanization process .....	35
3.3.3	Hydrothermal process for synthesized nanocomposite .....	36
3.3.3.1	Synthesis of rGO/CuO nanocomposite by hydrothermal method .....	37
3.3.3.2	Synthesis of FG/CuO nanocomposite by hydrothermal method .....	38
3.4	Characterization techniques .....	39
3.4.1	Determination of the crystalline structure by XRD.....	40
3.4.2	Determination of amount of weight loss over certain temperature by TGA .....	41
3.4.3	FT-IR for chemical bonding studies .....	42

3.4.4	Structural characteristics determined by micro Raman spectroscopy .....	43
3.4.5	FESEM for morphology and structure study .....	44
3.4.6	Morphology characterization using TEM .....	45
3.4.7	Optical properties measured by UV-vis spectroscopy .....	46
3.4.8	Catalytic activity .....	47
<b>Chapter 4: Results and discussion</b>		
4.1	Overview .....	48
4.2	Results for synthesis of CuO nanostructures .....	48
4.2.1	Structural characterization: XRD, micro Raman, and FT-IR analysis .....	48
4.2.2	Morphological characterization: FESEM and TEM analysis .....	57
4.2.3	Formation mechanism of CuO nanostructures .....	62
4.2.4	Catalytic activity of CuO nanostructures .....	71
4.3	Results for synthesis of GO, FGO and FG .....	75
4.3.1	Structural characterization: XRD, micro Raman, FT-IR and TGA analysis .....	76
4.3.2	Morphological characterization: FESEM and TEM analysis .....	87
4.3.3	Optical characterization: UV-vis spectroscopy analysis .....	90
4.3.4	Formation mechanism of GO, FGO and FG .....	92
4.4	Results for synthesis of rGO/CuO and FG/CuO nanocomposites .....	97
4.4.1	Structural characterization: XRD, micro Raman, and TGA analysis .....	98
4.4.2	Morphological characterization: FESEM and TEM analysis .....	106
4.4.3	Formation mechanism of the nanocomposite .....	111
4.4.4	Catalytic activity of rGO/CuO and FG/CuO nanocomposites .....	112

**Chapter 5: Conclusion**

5.1 Conclusion ..... **117**

5.2 Suggestions for future works ..... **119**

**References** ..... **121**

## LIST OF FIGURES

### Chapter 1

**Figure 1.1:** The form of graphene: 0 dimensional buckyball, 1 dimensional nanotube and 3 dimensional stacked graphite (*Geim et al., 2007*). .....1

**Figure 1.2:** The silanization process for producing FGO. The EDTA-silane molecules are added at the both surfaces of GO before reducing it to graphene via the hydrothermal method (*Shifeng Hou et al., 2010*). .....3

### Chapter 2

**Figure 2.1:** Molecular modeling of carbon in the form of (a) graphite, (b) diamond, (c) fullerene (buckyball), (d) nanotube and (e) graphene (*Scarselli et al., 2012*). .....9

**Figure 2.2:** (a) One atom thick graphene in a honeycomb lattice (b) The d-spacing of graphene. ....12

**Figure 2.3:** Timeline of selected events since 2004 that involved in the research of graphene and its nanocomposite. ....14

**Figure 2.4:** Synthesis method for producing graphene.....16

**Figure 2.5:** Schematic drawing of the assembled CVD setup used for the synthesis of graphene films (*Nguyen et al., 2012*). .....17

**Figure 2.6:** The  $sp^2$  hybridize orbitals between the carbon atoms and the  $\pi$  bonds. ....18

**Figure 2.7:** Some applications of graphene. ....20

**Figure 2.8:** The autoclave Teflon vessel used in the solvothermal method. ....25

### Chapter 3

**Figure 3.1:** Research methodology design. ....27

**Figure 3.2:** Flow chart of synthesis of CuO nanostructure via reflux method. ....30

**Figure 3.3:** Flow chart of synthesis of CuO nanostructure via hydrothermal method. .31

<b>Figure 3.4:</b> Flow chart of synthesis of CuO nanostructure via ultrasonication method. .....	<b>32</b>
<b>Figure 3.5:</b> Flow chart of synthesis of fibril-like CuO nanostructure using two steps heating method. ....	<b>33</b>
<b>Figure 3.6:</b> Schematic diagram of synthesizing GO.....	<b>34</b>
<b>Figure 3.7:</b> Schematic diagram of synthesizing FGO. ....	<b>36</b>
<b>Figure 3.8:</b> Schematic diagram for the formation of rGO/CuO nanocomposite. ....	<b>37</b>
<b>Figure 3.9:</b> Schematic diagram for the formation of FG/CuO nanocomposite. ....	<b>38</b>
<b>Figure 3.10:</b> Characterization techniques involved in this research.....	<b>39</b>
<b>Figure 3.11:</b> Philip XRD for crystal structure and composition studies.....	<b>40</b>
<b>Figure 3.12:</b> TG 209 F3 Tarsus thermal analyzer to study the rate of change in weight over temperature or time. ....	<b>41</b>
<b>Figure 3.13:</b> Perkin Elmer Instrument FT-IR version 5.0.1 for chemical bonding studies.....	<b>42</b>
<b>Figure 3.14:</b> Renishaw Raman Microscope for structural characterization. ....	<b>44</b>
<b>Figure 3.15:</b> FEI Quanta 400F FESEM for morphology and structural study. ....	<b>45</b>
<b>Figure 3.16:</b> Hitachi H7100 TEM for morphology study. ....	<b>46</b>
<b>Figure 3.17:</b> Thermo Scientific Evolution 300 ultraviolet-visible (UV-vis) spectrometer for optical characterization.....	<b>47</b>

## **Chapter 4**

<b>Figure 4.1:</b> XRD patterns of (a) standard and CuO nanostructures synthesized using (b) reflux, (c) hydrothermal, (d) ultrasonication and (e) two steps heating methods. ....	<b>49</b>
<b>Figure 4.2:</b> Micro Raman scattering spectra of CuO prepared using (a) reflux, (b) hydrothermal, (c) ultrasonication and (d) two steps heating methods. ....	<b>52</b>
<b>Figure 4.3:</b> FT-IR spectra of CuO preparing using (a) reflux, (b) two steps heating, (c) hydrothermal and (d) ultrasonication methods. ....	<b>54</b>

<b>Figure 4.4:</b> FESEM images of CuO synthesized via reflux method taken at (a) 20K x, (b) 40K x and (c) 80K x magnifications and (d) the EDX result for CuO nanoparticles.....	<b>57</b>
<b>Figure 4.5:</b> FESEM images of CuO synthesized via hydrothermal method taken at (a) 20K x, (b) 40K x and (c) 80K x magnifications and corresponding (d) TEM image. ....	<b>59</b>
<b>Figure 4.6:</b> FESEM images of CuO synthesized via ultrasonication method taken at (a) 20K x, (b) 40K x and (c) 80K x magnifications and corresponding (d) TEM image. ....	<b>60</b>
<b>Figure 4.7:</b> FESEM images of CuO synthesized via two steps heating method taken at (a) 20K x, (b) 40K x and (c) 80K x magnifications and corresponding (d) TEM image.....	<b>61</b>
<b>Figure 4.8:</b> Formation of CuO nanostructures.....	<b>63</b>
<b>Figure 4.9:</b> List of factors that affect the growth behavior of CuO.....	<b>66</b>
<b>Figure 4.10:</b> Growth of a Cu(OH) <sub>2</sub> with the help of CTAB as the surfactant which further reduced to form fibril-like CuO nanostructures ( <i>Filipič et al., 2012</i> ). ....	<b>69</b>
<b>Figure 4.11:</b> UV-vis absorption spectra of an aqueous solution of MB and H <sub>2</sub> O <sub>2</sub> in the presence of CuO nanostructures synthesized using (a) reflux, (b) hydrothermal, (c) ultrasonication and (d) two steps heating methods at different reaction times. ....	<b>72</b>
<b>Figure 4.12:</b> Time profile of MB degradation. ....	<b>73</b>
<b>Figure 4.13:</b> Ambient degradation of MB by CuO with the presence of H <sub>2</sub> O <sub>2</sub> .....	<b>75</b>
<b>Figure 4.14:</b> XRD patterns for (a) GO, (b) FGO and (c) FG.....	<b>77</b>
<b>Figure 4.15:</b> Micro Raman spectrum for (a) GO, (b) FGO and (c) FG.....	<b>79</b>
<b>Figure 4.16:</b> FT-IR spectrum for (a) GO, (b) FGO and (c) FG.....	<b>82</b>
<b>Figure 4.17:</b> TGA thermogram for (a) GO, (b) FGO and (c) FG.....	<b>85</b>
<b>Figure 4.18:</b> (a) FESEM and (b) TEM images for GO.....	<b>87</b>
<b>Figure 4.19:</b> (a) FESEM and (b) TEM images for FGO. ....	<b>89</b>

<b>Figure 4.20:</b> (a) FESEM and (b) TEM images for FG. ....	<b>90</b>
<b>Figure 4.21:</b> UV-vis spectra of (a) GO, (b) FGO and (c) FG. ....	<b>91</b>
<b>Figure 4.22:</b> The oxidation mechanism model of graphite sheets ( <i>Shao et al., 2012</i> ). .	<b>94</b>
<b>Figure 4.23:</b> Formation of FG via hydrothermal method. ....	<b>97</b>
<b>Figure 4.24:</b> XRD patterns of (a) FG, (b) rGO/CuO, (c) 2 mg FG/CuO, (d) 20 mg FG/CuO and (e) 30 mg FG/CuO nanocomposites. ....	<b>98</b>
<b>Figure 4.25:</b> Raman spectra for (a) FG, (b) rGO/CuO, (c) 2 mg FG/CuO, (d) 20 mg FG/CuO and (e) 30 mg FG/CuO nanocomposites. ....	<b>101</b>
<b>Figure 4.26:</b> Enlarged G band for (a) FG, (b) rGO/CuO, (c) 2 mg FG/CuO, (d) 20 mg FG/CuO and (e) 30 mg FG/CuO nanocomposites. ....	<b>102</b>
<b>Figure 4.27:</b> Thermogravimetric curve of (a) FG, (b) rGO/CuO, (c) 2 mg FG/CuO, (d) 20 mg FG/CuO and (e) 30 mg FG/CuO nanocomposites. ....	<b>104</b>
<b>Figure 4.28:</b> (a,b) FESEM and (c,d) TEM images of rGO/CuO nanocomposite. ....	<b>107</b>
<b>Figure 4.29:</b> (a,b) FESEM and (c,d) TEM images of 2 mg FG/CuO nanocomposite. ....	<b>108</b>
<b>Figure 4.30:</b> (a,b) FESEM and (c,d) TEM images of 20 mg FG/CuO nanocomposite. .....	<b>109</b>
<b>Figure 4.31:</b> (a,b) FESEM and (c,d) TEM images of 30 mg FG/CuO nanocomposite. .....	<b>110</b>
<b>Figure 4.32:</b> Formation of FG/CuO nanocomposite by hydrothermal method. ....	<b>112</b>
<b>Figure 4.33:</b> UV-vis absorption spectra of an aqueous solution of MB and H <sub>2</sub> O <sub>2</sub> in the presence of (a) rGO/CuO, (b) 2 mg FG/CuO, (c) 20 mg FG/CuO and (d) 30 mg FG/CuO nanocomposites at different reaction times. ....	<b>113</b>
<b>Figure 4.34:</b> Time profile of MB degradation with the presence of nanocomposites. ....	<b>114</b>
<b>Figure 4.35:</b> The catalytic activity mechanism for degradation of MB over FG/CuO nanocomposite. ....	<b>116</b>

## LIST OF TABLES

### **Chapter 2**

<b>Table 2.1:</b> Summarized of the properties for three types of common allotropes of carbon. ....	<b>9</b>
<b>Table 2.2:</b> The summary of the properties of graphene.....	<b>19</b>
<b>Table 2.3:</b> Review on the method of fabrication of FG.....	<b>21</b>
<b>Table 2.4:</b> The summary of the properties of CuO.....	<b>23</b>

### **Chapter 3**

<b>Table 3.1:</b> List of chemicals that were being used in this work. ....	<b>28</b>
<b>Table 3.2:</b> Overview of methods in synthesizing CuO.....	<b>29</b>

### **Chapter 4**

<b>Table 4.1:</b> Effects of different preparation methods on the micro Raman parameters such as peak position and intensity. ....	<b>52</b>
<b>Table 4.2:</b> Vibrational modes and wavenumbers exhibited by CuO based on our FT-IR result. ....	<b>55</b>
<b>Table 4.3:</b> Properties of GO, FGO and FG obtained by XRD analysis.....	<b>78</b>
<b>Table 4.4:</b> Vibrational modes and wavenumbers exhibited by GO, FGO and FG based on our FT-IR result.....	<b>82</b>
<b>Table 4.5:</b> Properties of rGO/CuO and FG/CuO nanocomposites with an appropriate amount of FGO flakes obtained by XRD analysis.....	<b>100</b>

## LIST OF ABBREVIATIONS

GO	Graphene oxide
FGO	Functionalized graphene oxide
FG	Functionalized graphene
CuO	Copper oxide
FG/CuO	Functionalized graphene/copper oxide nanocomposite
rGO/CuO	Reduced graphene/copper oxide nanocomposite
CNTs	Carbon nanotubes
XRD	X-ray diffraction
FESEM	Field emission scanning electron microscopy
TEM	Transmission electron microscopy
TGA	Thermogravimetric analysis
FT-IR	Fourier transform infrared
MB	Methylene blue
H <sub>2</sub> O <sub>2</sub>	Hydrogen peroxide
Cu(CH <sub>3</sub> COO) <sub>2</sub> ·H <sub>2</sub> O	Copper acetate monohydrate
Cu(OH) <sub>2</sub>	Copper hydroxide
CTAB	Cetyltrimethylammonium bromide
NH <sub>3</sub> ·H <sub>2</sub> O	Ammonia solution
NaOH	Sodium hydroxide
DIW	Deionized water
KMnO <sub>4</sub>	Potassium permanganate
HCl	Hydrochloric acid
H <sub>2</sub> SO <sub>4</sub>	Sulphuric acid
H <sub>3</sub> PO <sub>4</sub>	Phosphoric acid
KBr	Potassium bromide
EDTA-silane	N- (trimethoxysilylpropyl) ethylenediamine triacetic acid

## **LIST OF PUBLICATIONS**

Full-paper (ISI-cited)

1. **N. Yusoff**, N.M. Huang, M.R. Muhamad, S.V Kumar, H.N. Lim, I. Harrison. “Hydrothermal synthesis of copper oxide/functionalized graphene nanocomposites for dye degradation” *Materials Letters* 2013(93); 393-396.
2. Betty Yea Sze Chang, Nay Ming Huang, Mohd Nor An'amt, Abdul Rahman Marlinda, **Yusoff Norazriena**, Muhamad Rasat Muhamad, Ian Harrison, Hong Ngee Lim, and Chin Hua Chia “Facile hydrothermal preparation of titanium dioxide decorated reduced graphene oxide nanocomposite” *International Journal of Nanomedicine* 2012(7); 3379-3387.
3. A.R. Marlinda, N.M. Huang, M.R. Muhamad , M.N. An'amt , B.Y.S. Chang , **N. Yusoff**, I. Harrison, H.N. Lim, C.H. Chia, S. Vijay Kumar “Highly efficient preparation of ZnO nanorods decorated reduced graphene oxide nanocomposites” *Materials Letters* 2012(80); 9-12.
4. S. VijayKumar, N.M.Huang, **N.Yusoff**, H.N.Lim “High performance magnetically separable graphene/zinc oxide nanocomposite” *Materials Letters* 2013(93); 411-414.

## Chapter 1 Introduction

### 1.1 Overview of research studies

In the year of 2010, Geim and Novoselov, physicists from the University of Manchester had won the Nobel Prize in Physics for groundbreaking experiments in discovering the two-dimensional material named graphene (*Geim et al., 2007*). After that, a lot of studies have been done on this almost completely transparent material and researchers are trying harder to understand its unique properties. Graphene has known as a member of the carbon family that composed of  $sp^2$ -bonded carbon atoms arranged in a two-dimensional honeycomb lattice. This honeycomb structure has a d-spacing of about 0.34 nm, making it the thinnest material in the world so far. Graphene consists of one layer of carbon atom that can be wrapped up into zero-dimensional buckyballs, rolled into one-dimensional nanotube or stacked into three-dimensional graphite (**Figure 1.1**). Besides that, graphene exhibits a semimetal behavior proven by the existence of a small overlap between valence and conductance bands in graphene.

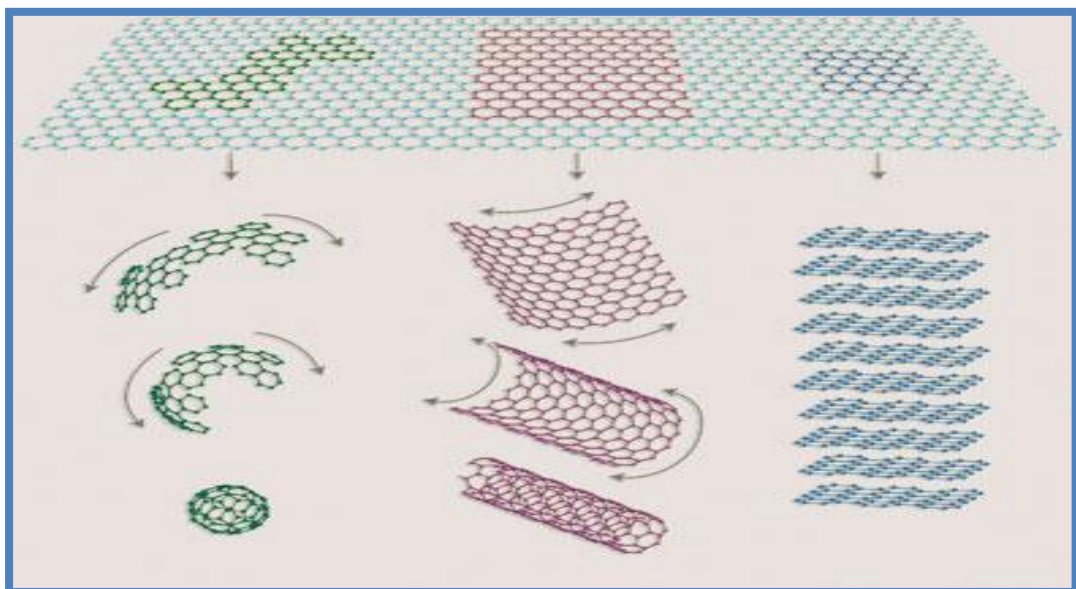


**Figure 1.1:** The form of graphene: 0-dimensional buckyball, 1-dimensional nanotube and 3-dimensional stacked graphite (*Geim et al., 2007*).

One of the reasons why graphene is so worthy to be studied is that graphene has an excellent mechanical properties with a high Young's modulus of almost 1 TPa (*Jiang et al., 2009*) due to the atoms that have covalently locked in place by the C-C bond. Besides that, it also possesses a high mobility of charge carriers of up to 20,000  $\text{m}^2 \text{V}^{-1} \text{s}^{-1}$  at room temperature (*Morozov et al., 2008*) due to its extensive two dimensional  $\pi$ - $\pi$  conjugation net and also has a high specific surface area of up to 2600  $\text{m}^2 \text{g}^{-1}$  (*Yun et al., 2011*). These fascinating properties render graphene a promising candidate for application in electronic devices such as transistor (*Britnell et al., 2012*), solar cell (*Wang et al., 2007*) and etc. Moreover, it is ensured that graphene is an ideal two-dimensional catalyst support to anchor metal and semiconductor catalyst nanoparticles, offering versatile selective catalytic or sensing performances.

However, there is challenging when dealing with graphene that is, it tends to form a precipitated agglomerate when dissolved in water and any organic solvents due to the  $\pi$ - $\pi$  stacking interactions which could limit its applications. In order to overcome this problem, researchers had come with several solution techniques and one of it is by chemically introduced a new functional groups onto the surface of graphene. Functionalization of graphene is believed to be able to enhance the properties of graphene by manipulating the surface of GO to obtain functional groups that serve as precursors for the anchoring of desirable organic/inorganic molecules, as well as to improve its dispersion in solvents. FG will become a platform for the nucleation and growth of nanoparticles, resulting in uniform size distribution and deposition of nanoparticles on the two-dimensional nanosheets. One of the ways to chemically modified GO is by silanization method as shown in **Figure 1.2**.

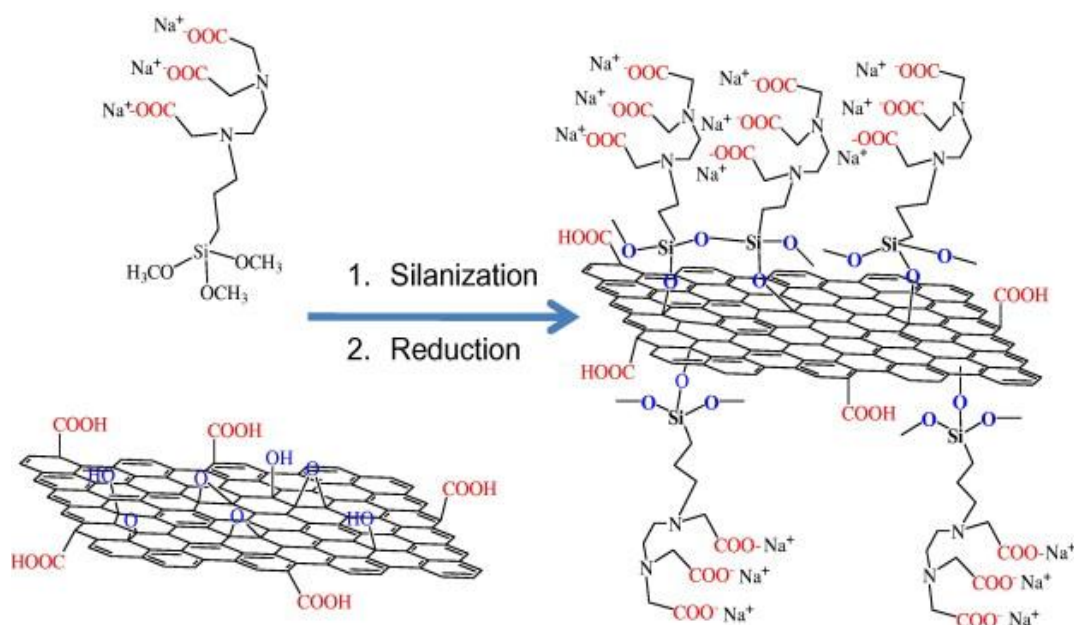


**Figure 1.2:** The silanization process for producing FGO. The EDTA-silane molecules are added at the both surfaces of GO before reducing it to graphene via the hydrothermal method (*Shifeng Hou et al., 2010*).

The study of graphene hybridized with metal oxide nanoparticles have attracted wide attention because this graphene-based nanocomposite has remarkable electrocatalytic (*Dong et al., 2010*), electrochemical sensing (*Wu et al., 2012*) and electrochemical energy conversion (*Wang et al., 2010*) properties, which make it a promising material for a wide range of applications such as gas sensing (*Neri et al., 2012*), catalysts (*Zhang et al., 2009*), electrochemical energy storage devices (*Baojun Li et al., 2011*), lithium-ion batteries (*Lian et al., 2010*), and etc.

For this purpose, CuO has been reported to be one of the best metal oxides that can be grown on graphene sheets. CuO has unique physical and chemical properties such as large specific surface area (*Batchelor-McAuley et al., 2008*), excellent solar light absorbance (*Xiao et al., 2011*), and a narrow band gap ( $E_g \sim 1.2$  eV) (*Vila et al., 2010*), rendering this material useful for many practical applications. CuO has also been

explored in various fields such as optoelectronics (*Manna et al., 2010*), electronics (*Liao et al., 2009*), gas sensing (*Jia et al., 2010*), solar cells (*Darvish et al., 2009*), batteries (*Xiang et al., 2010*) as well as heterogeneous catalysis (*Teng et al., 2008*).

Motivated by this idea, we are intrigued in producing a high quality of CuO decorated FG sheets nanocomposite via hydrothermal method. Beyond that, has been reported before that graphene-metal oxide nanocomposite has the ability to bring light in the environmental application where it has a great potential as a catalyst for dye removal in water waste treatment (*Chandra et al., 2010; Sun et al., 2011*). So it gives us a concrete point to prepare this FG/CuO and try to bring it back to the nature by applying it in the environmental application as a catalyst.

## **1.2 Focus and objectives of this research**

The main focus of this research is to synthesize a FG hybridized with CuO nanoparticles and study its structural and morphological properties using different kinds of characterization tools. The CuO nanostructures will be formed by using four different methods including reflux, hydrothermal, ultrasonication and two steps heating process. The best way to synthesized CuO with excellent catalytic performance will be chosen to fabricate the nanocomposite.

We believed that the hydrothermal method will be the best method to prepare the nanocomposite due to several advantages (*Zhou et al., 2009*) that are: (1) very simple setup, (2) good upward scalability and industrially compatible with batch processing, (3) product gained is intrinsically pure because it utilizes only water, (4) could minimize defects due to the closed system of relatively high temperature and internal pressure which promotes the recovery of  $\pi$ -conjugation after dehydration, and

(5) easy to control the degree of reduction of GO by controlling the parameters of temperature and pressure. Other than that, it also provide a system that allowed the reduction of GO to graphene and copper ions to CuO to happen and at the same time forming the nanocomposite.

Next we intend to study the difference in properties for GO and FGO and observe how this modified GO would help to make a good nanocomposite with CuO and be a promising candidate material that can be widely used in different field of applications especially catalysis. For this work, GO will be obtained by oxidation of graphite flakes via simplified Hummers' method. To silanize GO, EDTA-silane will be added under reflux condition. The final products will be characterized by X-ray diffraction (XRD), transmission electron microscopy (TEM), field emission scanning electron microscopy (FESEM), Fourier transform infrared spectrometer (FT-IR), UV-vis absorption spectroscopy, micro Raman and thermogravimetric analysis (TGA).

Another goal of this dissertation is to examine the potential application of the nanocomposite in the field of catalysis. Catalytic activity is evaluated by examining the degradation of methylene blue (MB) as a model for dye pollutant in water with the assisted of hydrogen peroxide ( $H_2O_2$ ). In comparison with pure CuO and reduced graphene oxide/CuO (rGO/CuO) nanocomposite, FG/CuO nanocomposite presumes can be served as the best catalyst for the degradation of MB due to excellent interface electronic interaction between CuO and FG.

Below are the objectives for this research:

- I. To synthesize CuO nanostructure before proceed with the fabrication of FG/CuO and rGO/CuO nanocomposite for comparison.
- II. To study the structural and morphological properties of both nanocomposites and make comparison for their properties.
- III. To investigate the potential of this nanocomposite to be used as a catalyst for dye removal in water waste treatment.

### **1.3 Outline of the dissertation**

This dissertation is divided into five main chapters including 1. Introduction, 2. Literature review, 3. Experimental methods, 4. Results and discussion and 5. Conclusion. The brief introduction about graphene, CuO, major focus and objectives of this research are introduced in the first chapter.

Further on, one can find a brief discussion and review about graphene and CuO in *Chapter 2, Literature review*. This chapter focuses on describing the properties of CuO nanostructures and graphene especially on structural and morphological properties and also methods of producing nanocomposite such as hydrothermal, solvothermal, and microwave-assisted methods.

The third chapter, *Chapter 3, Experimental methods* discuss on the procedure in preparing samples consisted of CuO, GO, FGO and fabrication of nanocomposite. Besides that, the characterization techniques used in this work are also been described in this chapter.

The *Chapter 4, Results and discussion* are divided into three parts. In the first part, the result of synthesizing CuO using different methods and its catalytic activity is revealed and discussed. The second part of this chapter contains the analytical results and comparison for FG as well as FGO and GO. The study on the nanocomposite and its catalytic performance is also presented in this chapter.

The summarized of analysis and the conclusion on the research findings are presented in *Chapter 5, Conclusion*. Several suggestions regarding methods to improve the present work and also ideas for future work are also included in the last part of this chapter.

## Chapter 2 Literature Review

### 2.1 Introduction

This chapter covers a brief introduction of carbon materials, graphene, FG and CuO including their properties and applications. There are several techniques to synthesize CuO nanoparticles encapsulated by graphene such as hydrothermal, solvothermal and microwave assisted methods. The simple elaboration on each of these techniques will be discussed in this chapter as well.

### 2.2 Carbon materials: An introduction

Represented by the symbol C on the periodic table with the atomic number of six, carbon is one of the abundant elements on earth and plays a unique role in nature. Carbon not only becomes one of the main elements in plants and animals but it is also a part of constituent in various minerals such as limestone and marble as well as coal and petroleum. It can be found mainly in the combined form or in an elemental form. Like in earth's atmosphere, carbon exists as a compound of carbon dioxide which plays a vital role in the carbon life cycle, thought to be one of the reasons why life is depending on this element.

Allotrope is the name given to a various form or chemical structure arises from the modification of the same element. It can have similar or different physical and chemical properties. In the case of carbon, there are three well known allotropes namely diamond, fullerene and graphite (**Figure 2.1**), where each of these are categorized according to the specific hybridization of carbon and the ways its bonding to surrounding atoms.

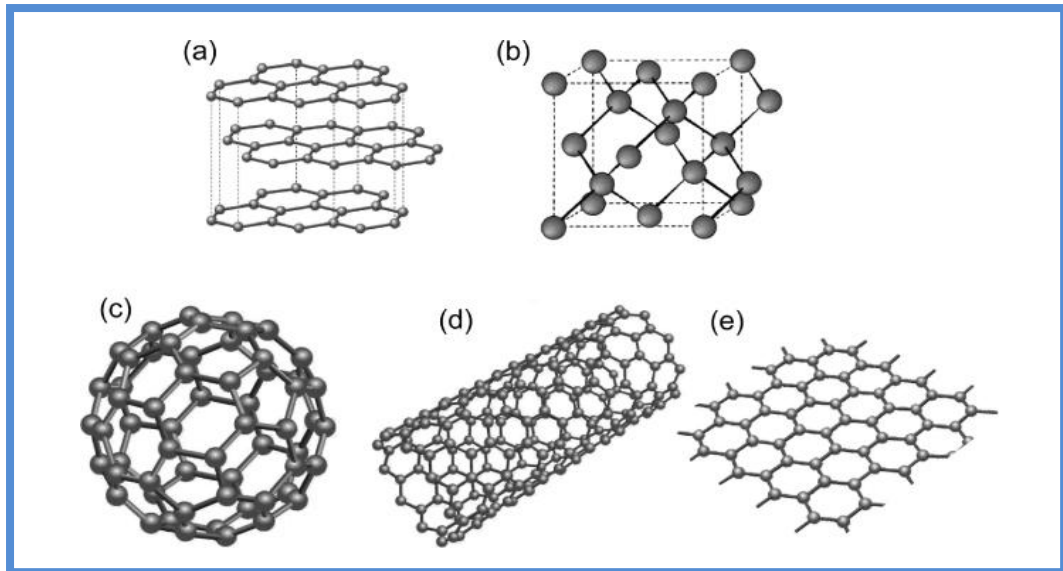


**Figure 2.1:** Molecular modeling of carbon in the form of (a) graphite, (b) diamond, (c) fullerene (buckyball), (d) nanotube and (e) graphene (Scarselli et al., 2012).

Diamond consists of the carbon with  $sp^3$  hybridization that form a tetrahedral structure while graphite and fullerene made up from  $sp^2$  hybridizes carbon but with different ways of packing. In general, carbon can form strong molecules in zero-dimensions of buckyballs, one-dimension of carbon nanotubes, two-dimensions of graphene or stacked graphite and three-dimensions of the diamond. Each of these allotropes owns their unique properties as summarized **Table 2.1**.

**Table 2.1:** Summarized of the properties for three types of common allotropes of carbon.

<i>Properties</i>	<i>Diamond</i>	<i>Fullerene (C<sub>60</sub>)</i>	<i>Graphite</i>
<i>Crystal structure</i>	Cubic	face-centered cubic	hexagonal
<i>Crystal formation</i>	Octahedral	hexagonal, cubic	tubular
<i>C-C length (Å)</i>	1.54	1.455	1.42
<i>Density (g cm<sup>-3</sup>)</i>	3.30	1.65	2.27
<i>Melting point (K)</i>	3700	> 553	3800
<i>Conductivity</i>	Insulator	semiconductor	conductor
<i>Resistivity (ohm m)</i>	$1 \times 10^{18}$	$1 \times 10^{14}$	$1.37 \times 10^{-5}$
<i>Bulk modulus(G Pa)</i>	1200	9.1	207

### 2.3 A journey from GO to graphene

In 1859, Brodie (*Brodie, 1859*) had unintentionally discovered a method to prepare a material so called graphitic acid. It is called so because it is insoluble in acids and saline solution but dispersed well in pure water and alkalines. His method is based on the ideas of graphite undergo an oxidation process by treating it with a strong acidic mixture containing potassium chlorate and fuming nitric acid. At first, Brodie had done several experiments toward graphite as he was keen to study the structure of graphite. From the first attempt of oxidizing the graphite, he found that i) the final substance form as a peculiar compound of carbon with its weight larger than that graphite ii) the final substance changed to light yellow color substance composed of transparent plates after fourth or fifth times of treatments.

Following experiments had changed his initial interest from study the structure to molecular formula of graphite and its discrete molecular weight. His investigation has revealed that i) the product obtained consists of mainly carbon, hydrogen and oxygen with a net molecular formula of  $C_{2.19}H_{0.80}O_{1.00}$  ii) the atomic weight of graphite is 33 iii) carbon in the form of graphite functions as a distinct element where it forms a distinctive system of combination (*Brodie, 1859*). Brodie finally named this substance as graphon, thus becomes the starting point that led to the current research of graphene.

This idea was expanded by another researcher such as Staudenmaier in 1898 where he used concentrated sulfuric and nitric acids with potassium chlorate to oxidize the graphite flakes. The gradual increase amount of potassium chloride in this method was designed to accelerate the rate of oxidation of graphite without having to repeat the same process as what was done by Brodie. As a result, the degree of oxidation of graphite was similar as Brodie's method which the ratio of carbon to oxygen is almost

equal to 2:1. Despite this method is more practical but hazardous. In 1958, Hummers and Offeman (*Hummers Jr et al., 1958*) modified this method by developing a safety procedure of oxidizing graphite flakes that took less than two hours to be completed. They were treating graphite flakes with a water-free mixture of concentrated  $\text{H}_2\text{SO}_4$ , sodium nitrate and  $\text{KMnO}_4$ , resulting in the similar level of oxidation.

Since then, the Hummers' method was used as a reference to produce GO, with some modification as to avoid generating toxic gas and time consuming, thus achieving a higher level of oxidation. In 2010, Marcano *et al.* described an improved method of synthesizing GO by i) excluding the nitric acid ii) increasing the amount of  $\text{KMnO}_4$  iii) performing the reaction in a 9:1 mixture of  $\text{H}_2\text{SO}_4/\text{H}_3\text{PO}_4$ . This improved procedure has been proved to produce a large scale of hydrophilic GO with fewer defects in the basal planes (*Marcano et al., 2010*). Moreover, this process did not generate toxic gases and it improved the graphite oxidation efficiency making it more oxidized as compared to Hummers' method.

Over the past decades, an atom thick layer of crystalline carbon arranges in a honeycomb lattice (**Figure 2.2**) known as graphene have attracted enormous interest due to its remarkable physical and electrical properties that hold great promise for future applications. In 2010, the Nobel Physics Prize was awarded to Andre Geim and Konstantin Novoselov from University of Manchester concerning a new finding of an experiment with regard to thinnest materials of graphene. Based on this experiment, they used graphite flakes as the starting materials for producing few layer graphene before peel off to isolating the graphene layers from bulk graphite using scotch tape. This process is called micromechanical cleavage method which is one of the earlier method that able to produce graphene with millimeter in size.

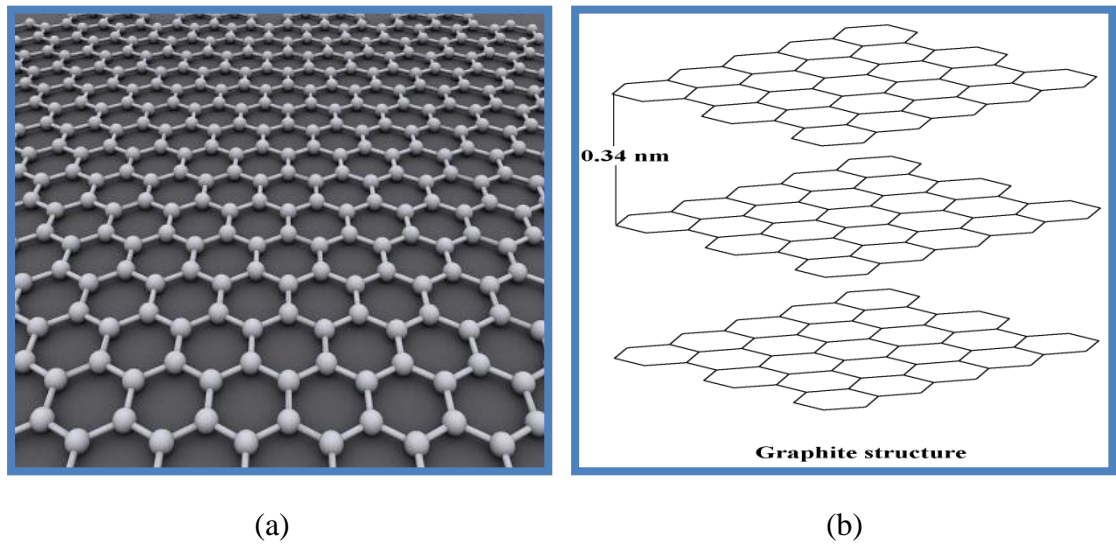


**Figure 2.2:** (a) One atom thick graphene in a honeycomb lattice (b) The d-spacing of graphene.

Since this discovery, the journey of graphene has begins. At first, researchers are interested in finding the best method for the synthesis of single layer graphene and up to dates there are several methods had been reported can be used to prepared graphene such as chemical vapor deposition (*Bautista et al., 2011*), rapid thermal reduction (*Chen et al., 2010*) and others. Next, they started to hybridize this graphene sheets with other polymers (*Carotenuto et al., 2012*), metal (*Xu et al., 2008*) and metal oxide (*Zou et al., 2011*) as they believed that by anchoring these materials on the graphene sheet can enhance its properties as an interesting material to be applied in a wide field of application.

Unfortunately, graphene has the hydrophobic properties toward water and other organic and inorganic solvent which limits its application. Graphene sheets tend to form irreversible agglomerates and even restocked to form graphite via van der Walls interaction. This arising issue drives the researchers to manipulate graphene properties by introducing new functional groups on the surface of graphene sheets. FG with

hydrophilic groups were then used to prepare nanocomposites with other materials (*Psarras et al.*). Some of the selected events are related to the development of graphene is presented in **Figure 2.3**.

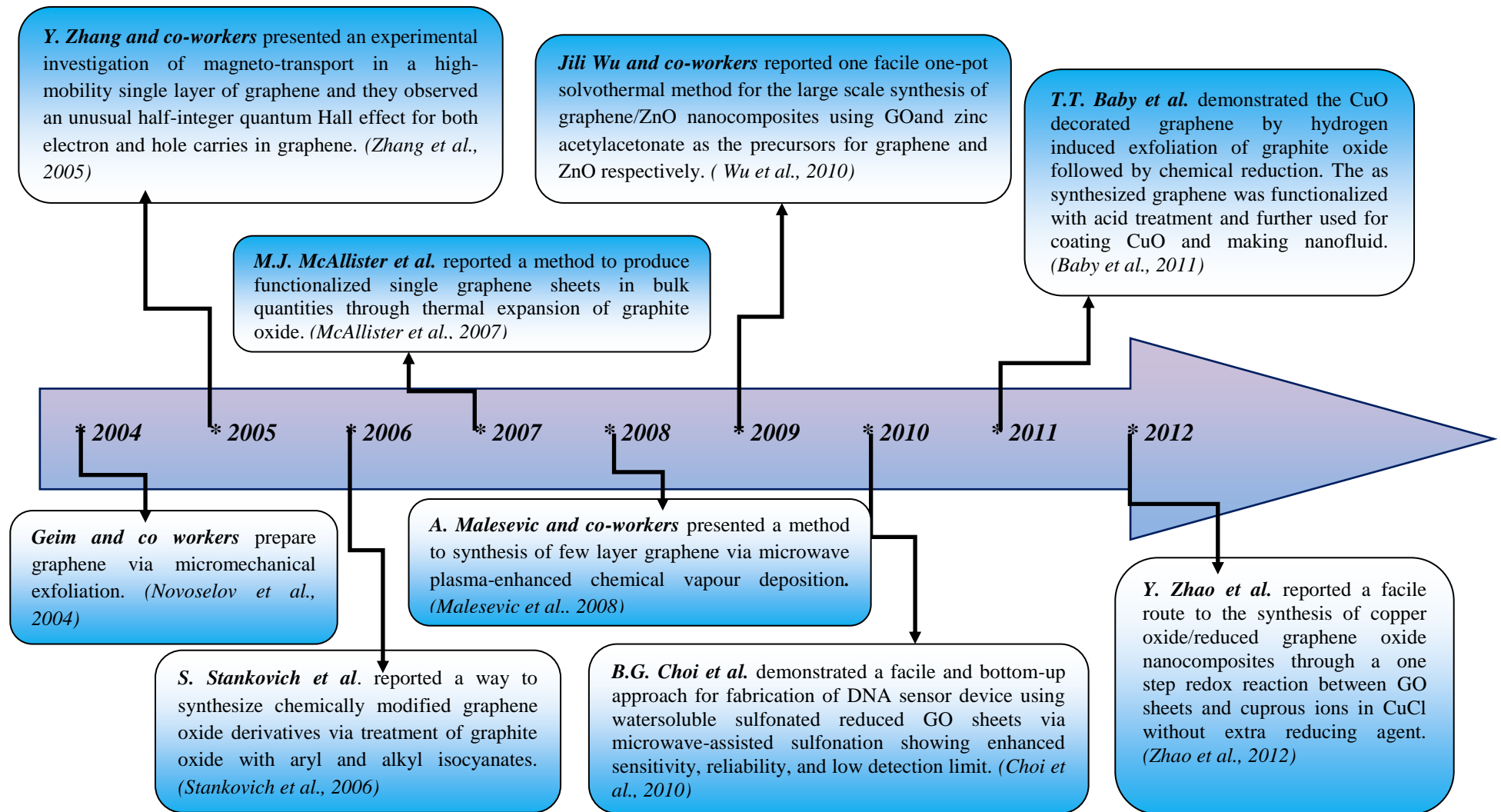


**Figure 2.3:** Timeline of selected events since 2004 that involved in the research of graphene and its nanocomposite.

### 2.3.1 Reviews on several methods of preparing graphene

Recently, there are many experimental methods that had been reported to fabricate single layer graphene sheet. Each of these methods is evaluated based on the different requirements needed by the researcher. The most important aspect emphasized by the researchers is the quality in term of the purity of the graphene which defined by the numbers of defects and degree of oxidation of graphene. Lack in the number of intrinsic defects and higher in the degree of oxidation will lead to the outstanding properties of graphene. The aspect of the number and size of the layers obtained which each of the methods that have been reported is intended to produce multi- or single-layer of graphene with different size of surface area.

Besides that, the amount of graphene that can be produced is another crucial aspect that needs to be take note as most of the methods demonstrated have a low productivity, which makes it unsuitable for large-scale use. Other than that, the complexity also plays an important role in the choosing the best method for production of graphene as method that possess complicated designed machines will wasted researcher time and cost. Complicated method with lack of controllability also will lead to the less reproducible results that can achieved so the ability to control is another aspect that cause the difference exist between each method.

In general, the production of graphene can be approached in two ways named top-down and bottom-up approach (**Figure 2.4**). For top-down approach, the process involves breaking down the macroscopic structures which are the graphite into microscopic structural material that is the single layer graphene. There are two types of method that use the top down approaches that are micromechanical exfoliation of graphite (which also known as the scotch tape or peel off method) and also including

the ultrasonication method. Wang *et al.* reported a way to synthesize a stable high-concentration suspensions of non-oxidized few layers of graphene with micrometer long edges by tip ultrasonication where graphite flakes are directly exfoliated in ionic liquids, such as 1-butyl-3-methylimidazolium bis(trifluoromethanesulfonyl)imide ([Bmim]-[Tf2N]) (Wang *et al.*, 2010). Another type is the creation of colloidal suspensions from graphite oxide or GO. In order to form graphene, these graphite oxide or GO will undergo reduction through chemically or thermally, and currently by microwave assisted (Zhu *et al.*, 2010).

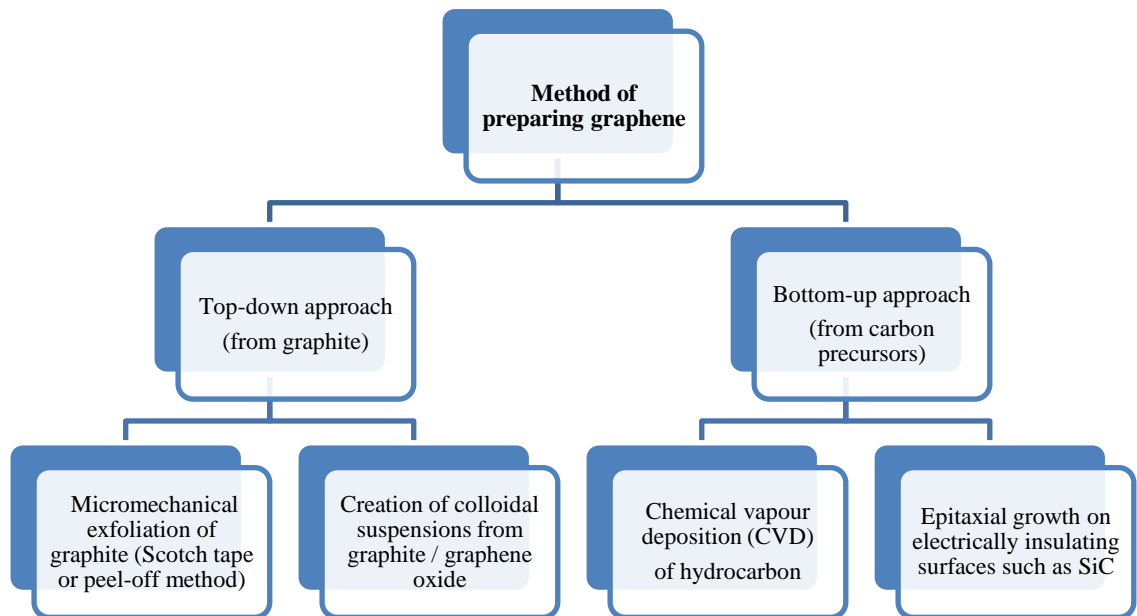


**Figure 2.4:** Synthesis method for producing graphene.

Another approach is the bottom-up approach where graphene is obtained from a carbon material as the precursor which can be grown directly on the substrate surface. The bottom-up approach is divided into two parts that are by chemical vapor deposition (CVD) of hydrocarbon and by epitaxial growth on electrically insulating surfaces such as silicon carbide (SiC). The CVD process involved the exposure of a substrate to a

gaseous compound where then decompose on the surface in order to grow a thin film, whereas the by-products evaporate (**Figure 2.5**). This can be achieved either by heating the sample with a filament or with plasma. Wang and co-worker had successfully synthesized a large scale of substrate free graphene via the CVD of methane over cobalt supported on magnesium oxides at 1000 °C in a gas flow of argon (Wang *et al.*, 2009). They found the presence of localized  $sp^3$  defects within the  $sp^2$  carbon network and small  $sp^2$  domains in the few-layered graphene particles obtained from this method. Meanwhile, Sprinkle *et al.* had demonstrated a way to produce the graphene nanoribbons with self-organized growth on a template SiC substrate using scalable photolithography and microelectronics processing (Sprinkle *et al.*, 2010).

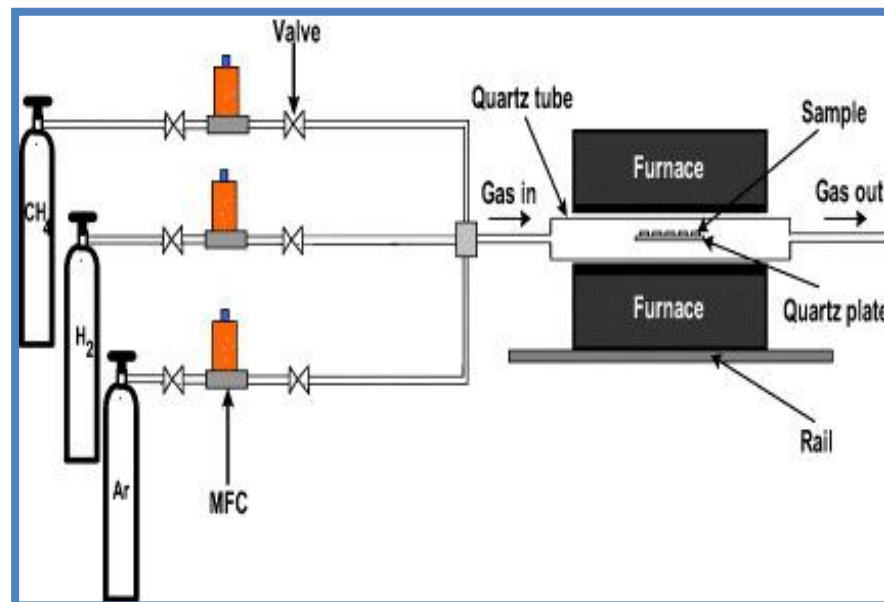


**Figure 2.5:** Schematic drawing of the assembled CVD setup used for the synthesis of graphene films (Nguyen *et al.*, 2012).

### 2.3.2 Properties and application of graphene

Recently, graphene has attract much attention as graphene possess unique properties, which make it as an outstanding material that having a profound impact in many areas of science and technology. It is well known that graphene is built up from the  $sp^2$  bonded carbon atoms that arranged in the 2-D honeycomb crystal lattices. The carbon atoms bonded in  $sp^2$  bonding will bind to three neighbours (**Figure 2.6**), which also known as trigonal hybridization forming planar structures of graphene. Each carbon atom in the lattice has a  $\pi$  orbital that contributes to a delocalized network of electrons.

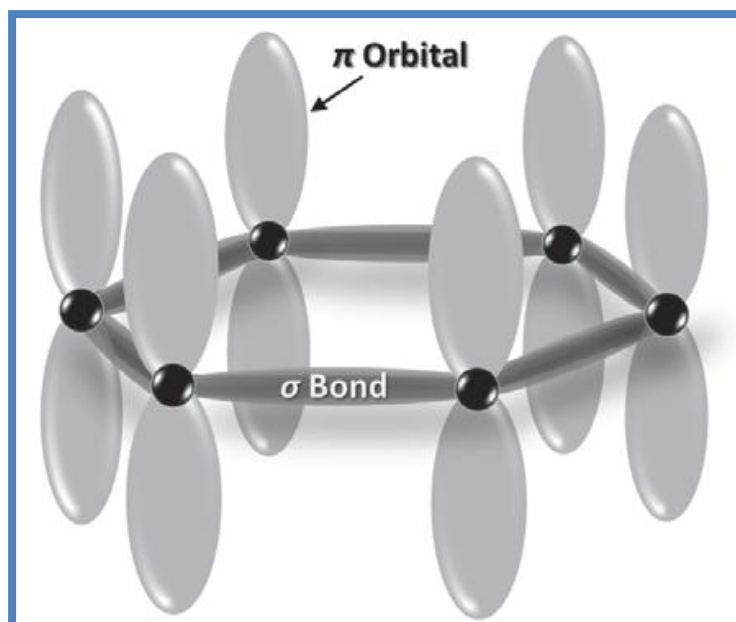


**Figure 2.6:** The  $sp^2$  hybridize orbitals between the carbon atoms and the  $\pi$  bonds.

The C-C covalent bond is one of the strongest bond in nature and well known of its basic constitution of the graphite lattice. The strength of this  $sp^2$  C-C bond gives graphene some exceptional mechanical properties, possibly better than any other material. Moreover, graphene posses extraordinary properties including the high specific surface area, extraordinary electronic properties and electron transport

capabilities, strong mechanical strength and excellent thermal and electrical conductivities as a consequence of its structure. Some of the properties of graphene are summarized in **Table 2.2** below.

**Table 2.2:** The summary of the properties of graphene.

<i>Property</i>	<i>Value</i>	<i>Reference</i>
<b>Structural</b> <i>a)Surface area</i> <i>b)Crystal structure</i>	a) 1256 m <sup>2</sup> /g b) two-dimensional hexagonal	a) (Wang et al., 2012) b) (Katsnelson, 2007)
<b>Electrical</b> <i>a)Electron mobility</i> <i>b)Electrical conductivity</i>	a) > 200,000 cm <sup>2</sup> V <sup>-1</sup> s <sup>-1</sup> b) in the order of 10 <sup>2</sup> S/cm ( $R_s < 1$ k $\Omega$ /square)	a) (Bolotin et al., 2008) b) (Becerril et al., 2008)
<b>Optical</b> <i>a)Optical transmittance</i> <i>b)Bandgap</i>	a) 80 % in 400-1800 nm wavelength range b) 0- 250 meV (Tunable)	a) (Becerril et al., 2008) b) (Zhang et al., 2009)
<b>Mechanical</b> <i>a)Young's modulus</i> <i>b)Fracture strength</i>	a) 1.1 TPa b) 10 GPa	a) (Jiang et al., 2009) b) (Liu et al., 2012)

Due to the remarkable physicochemical properties, graphene offers great potential in various fields of applications ever since its discovery in 2004. These unique physicochemical properties suggest it has great potential for providing new approaches and critical improvements in the field of electrochemistry. For example, the high surface area of electrically conductive graphene sheets can give rise to high densities of attached analyte molecules. This in turn can facilitate high sensitivity and device miniaturization. Besides that, graphene also shows a great performance as a catalyst due to its high surface area that helps to enhance the adsorption and desorption of reactants. The high speed at which electrons in graphene move and facile electron transfer opens up opportunities for built up higher frequency transistors, sensors, solar

cell and many more. Other than that, graphene could also be used to make lithium-ion battery that are rechargeable faster than before due to the presence of defects in the graphene sheet that provide pathways for the lithium ions to attach to the anode substrate. **Figure 2.7** shows some of the applications for graphene as solar cell, transistor, organic light emitting diodes and energy storage.

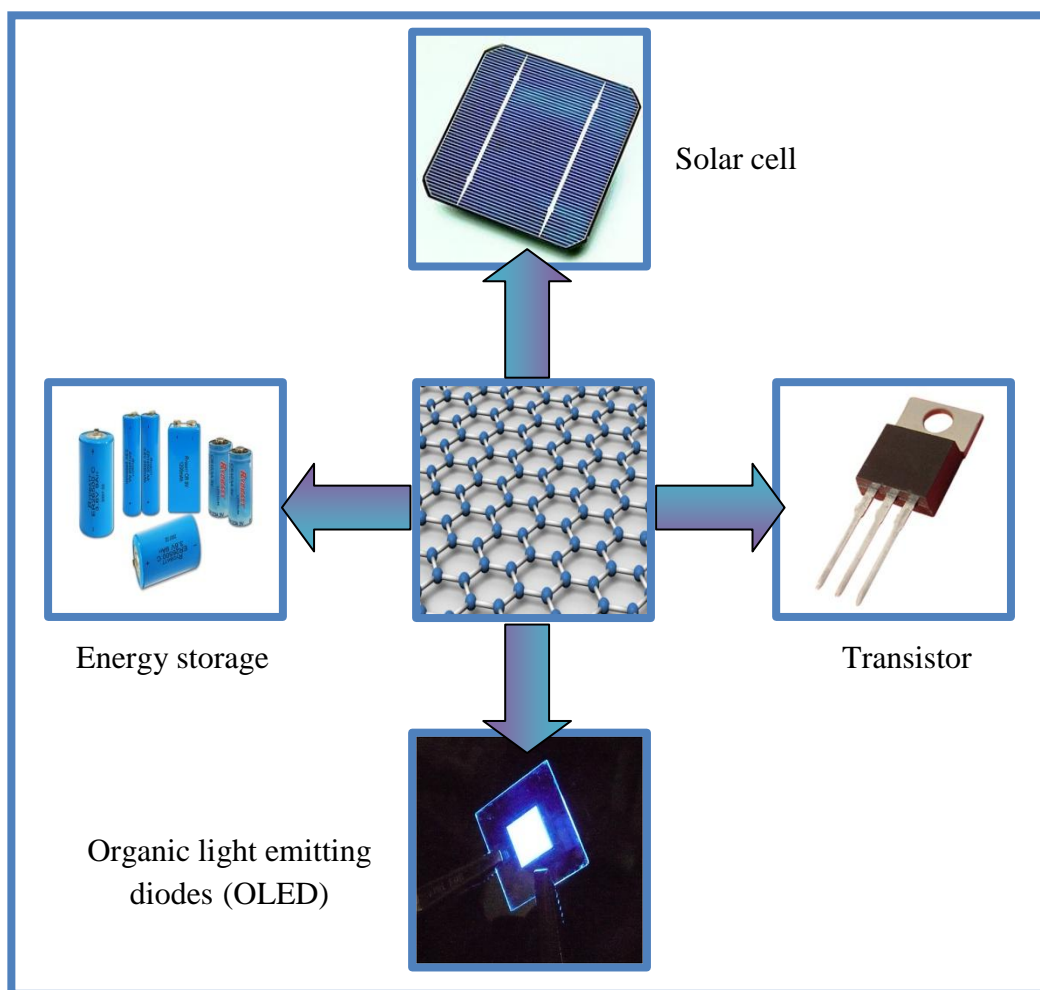


**Figure 2.7:** Some applications of graphene.

### 2.3.3 Functionalized graphene (FG)

FG is defined as graphene that had been modified by introducing a new functional groups linking to its surfaces in order to enhance its potential in desired properties. Functionalization of graphene can be done in many ways such as reactions of graphene (and its derivatives) with organic and inorganic molecules, chemical

modification of the large graphene surface, and the general description of various covalent and noncovalent interactions with graphene (Georgakilas *et al.*, 2012). Functionalization of graphene is believed to be able to enhance the properties of graphene by manipulating the surface of graphene oxide to obtain functional groups that serve as precursors for the anchoring of desirable organic/inorganic molecules, as well as to improve its dispersion in solvents. FG will become a platform for the nucleation and growth of nanoparticles, resulting in uniform size distribution and deposition of nanoparticles on the two-dimensional nanosheets (Paula Marques, 2011). **Table 2.3** shows some review on the method of fabrication of FG.

**Table 2.3:** Review on the method of fabrication of FG.

<i>Year</i>	<i>Review on method to produce FG</i>	<i>Reference</i>
<b>2009</b>	Yang et al. demonstrated a reflux method to synthesized polydisperse graphene nanosheets by amine-terminated ionic liquid via covalent functionalization.	Yang et al. (Yang, Shan, et al., 2009)
<b>2009</b>	Bekyarova and co-worker had studied the chemical modification of epitaxial graphene via covalent attachment of aryl groups to the basal carbon atoms.	Bekyarova et al. (Bekyarova et al., 2009)
<b>2010</b>	Pham et al. successfully fabricate FGO and reduced it into chemically converted graphene by solvothermal reduction of a GO suspension in N-methyl-2-pyrrolidone (NMP).	Pham et al. (Pham et al., 2010)
<b>2011</b>	Xu and co-worker used a convenient single-step sonochemical approach to fabricate the polymer functionalized graphenes using a reactive solvent with appropriate surface tension.	Xu et al. (Xu et al., 2011)

## 2.4 The introduction of CuO

Metal oxide nanostructures such as zinc oxide, titanium dioxide, iron oxide and etc have attracted much attention because of their extraordinary properties in different fields of optics, optoelectronics, catalysts, solar cell materials and sensors. In this regard, copper oxide-based materials with nanostructures have been widely investigated due to their potential applications in chemical, photochemical and electrochemical

fields, particularly in water splitting under visible light irradiation, windows for solar energy conversion and catalytic as well as electrochromic applications (*Gao et al., 2004; Jiang et al., 2002; Xiao et al., 2007; Yang et al., 2007; Yu et al., 2004; Zhou et al., 2006*).

Considerable efforts have been made to synthesize various CuO nano- and microstructures with controllable morphology, as the chemical and physical properties of CuO are dependent on its size and shape. The formation of various CuO nanostructures has been extensively studied using techniques such as thermal decomposition, hydrothermal, self-catalytic growth and solvothermal. Through these methods, CuO nanostructures such as nanorods, nanowires, nanotubes, nanoplatelets, nanodendrites, and nanoflowers have been synthesized.

#### **2.4.1 Properties and application of CuO**

In the current days of science and technology, CuO which is also known as cupric oxide have attracted more attention from researcher because of its unique physical and chemical properties such as high electron communication features, high specific surface area, high solar absorbency and narrow band gap ( $E_g \sim 1.2$  eV). All these unique properties are relative to its diversity of nanostructures. The properties of CuO are summarized in **Table 2.4**.

**Table 2.4:** The summary of the properties of CuO.

<i>Property</i>	<i>Value</i>
<i>Structural:</i> a) <i>stable crystal structure</i> b) <i>lattice constant</i>	a) monoclinic b) a = 4.68 Å, b = 3.42 Å, c = 5.13 Å
<i>Electrical:</i> a) <i>reversible capacity</i> b) <i>hole mobility</i>	a) 630 mA h g <sup>-1</sup> b) 0.1-10 cm <sup>2</sup> / V s
<i>Optical:</i> a) <i>band gap</i> b) <i>refractive index</i>	a) 1.2 eV, direct b) 1.4

Being one of the important narrow band gap semiconductor, CuO has shown an excellent performance, thus could be used in a wide range of practical applications. CuO has been explored in different fields of optoelectronics, electronics, biosensors, solar cells, magnetic storage media, optical switch, and batteries and heterogeneous catalysts. For instance, with the high theoretical lithium storage capacity lift up CuO as an active anode material for lithium ion batteries. Other than that, CuO possess great photoconductive and photochemical properties which making it a potential material for solar cell fabrication. In addition, CuO exhibits higher surface area which relative to its size and morphology, thus may give it an advantage as a catalyst in water treatment for removal of dye.

## 2.5 Reviews on several preparation techniques for synthesis of graphene/CuO nanocomposite

Recently, there are few methods had been reported that can be used to synthesize graphene nanocomposite such as hydrothermal (*Shen et al., 2011*), solvothermal (*Wu et al., 2010*) and microwave (*Lu et al., 2011*) assisted methods. Below are some reviews regarding these three methods of synthesizing graphene hybridized with metal oxide.

### 2.5.1 Hydrothermal method

One of the common ways for the synthesis of graphene nanocomposite is using hydrothermal method as it is a simple and safe procedure as well as environmentally friendly method. Moreover, it is being reported before that GO and metal could be reduced to graphene and metal oxide nanoparticles simultaneously under hydrothermal reaction thus reduced the reaction time. Other than that, hydrothermal method is believed could be used to produce smaller particle up to the nanoscale. Basically, hydrothermal reaction is conducted in stainless steel autoclaves with Teflon liners under controlled temperature and/or pressure. This autoclaves will undergo a heating process via oven or furnace heating. The reaction occurs in aqueous solutions where water acts as the solvent. The temperatures can be elevated above the boiling point of water, reaching the pressure of vapor saturation. The internal pressure produced in this reaction is largely relative to the amount of solution added to the autoclave. Xue *et al.* was using the hydrothermal method with the presence of Na<sub>2</sub>S as the reducing agent and also sulfide source to deposit ZnS nanoparticles on the surface of graphene sheets (Xue *et al.*, 2011).

### 2.5.2 Solvothermal method

Solvothermal is one of the versatile methods to synthesized graphene grown with fine distribution of narrow size nanoparticles on its surfaces. Basically, solvothermal method is almost identical to the hydrothermal method except that the solvent used here is non aqueous. This solvent could play a role as reducing agent at the same time to reduce GO and synthesizing nanoparticles (Wu *et al.*, 2010). Compared to hydrothermal method, the operating temperature can be tuned up to the high boiling point of the chosen solvent. Besides that, this method has a better control than the hydrothermal method of the size and shape distributions of the

nanoparticles. The very high self-generated pressure inside the sealed reaction vessel (autogenous pressure) (**Figure 2.8**) and containment of volatile products rendering solvothermal as a suitable method to form metastable phases. Zhou *et al.* had used the one-pot solvothermal reaction to synthesizing graphene decorated with good distribution of magnetite particles on its surfaces (Zhou *et al.*, 2010). They used ethylene glycol as the solvent and reducing agent. Zhang *et al.* also used facile solvothermal method to prepared zinc oxide/graphene nanocomposite with the Zn-EG-Ac complex and GO as the precursor and ethanol as the solvent and reducing agent (Zhang *et al.*, 2012).



**Figure 2.8:** The autoclave Teflon vessel used in the solvothermal method.

### 2.5.3 Microwave assisted method

Recently, researchers has use microwave heating method as an alternative method to the conventional heating method for preparing a bulk quantity of graphene nanocomposite. This is due to the higher reaction rates and reduction in reaction time. Vadahanambi *et al.* had successfully prepare graphene hybridized with metal

nanoparticles using the microwave assisted method with the addition of chemical foaming agents and green oxidizers (*Vadahanambi et al., 2011*). Under rapid microwave heating, different morphology of CuO nanostructures decorated on graphene could be synthesized by varying the reaction temperature as reported by Lu *et al.* (*Lu et al., 2011*). A petal-like graphene nanosheets/NiO composite was successfully produced by a simple procedure and without any controlling-agent after GO was reduced to graphene and formed the composite with NiO via a microwave-assisted method as reported by Su *et al.* (*Su et al., 2013*).

## Chapter 3 Experimental Methods

### 3.1 Introduction

The purpose of this chapter is to present the research strategy including the methods of synthesizing and characterizing the samples. The content of this chapter is partitioned into two sections with the first section covers the experimental procedures for preparing the samples started from producing CuO until fabricating the nanocomposite. The second section appears to describe the characterization techniques that been used in this work. The research methodology design is shown in **Figure 3.1**.

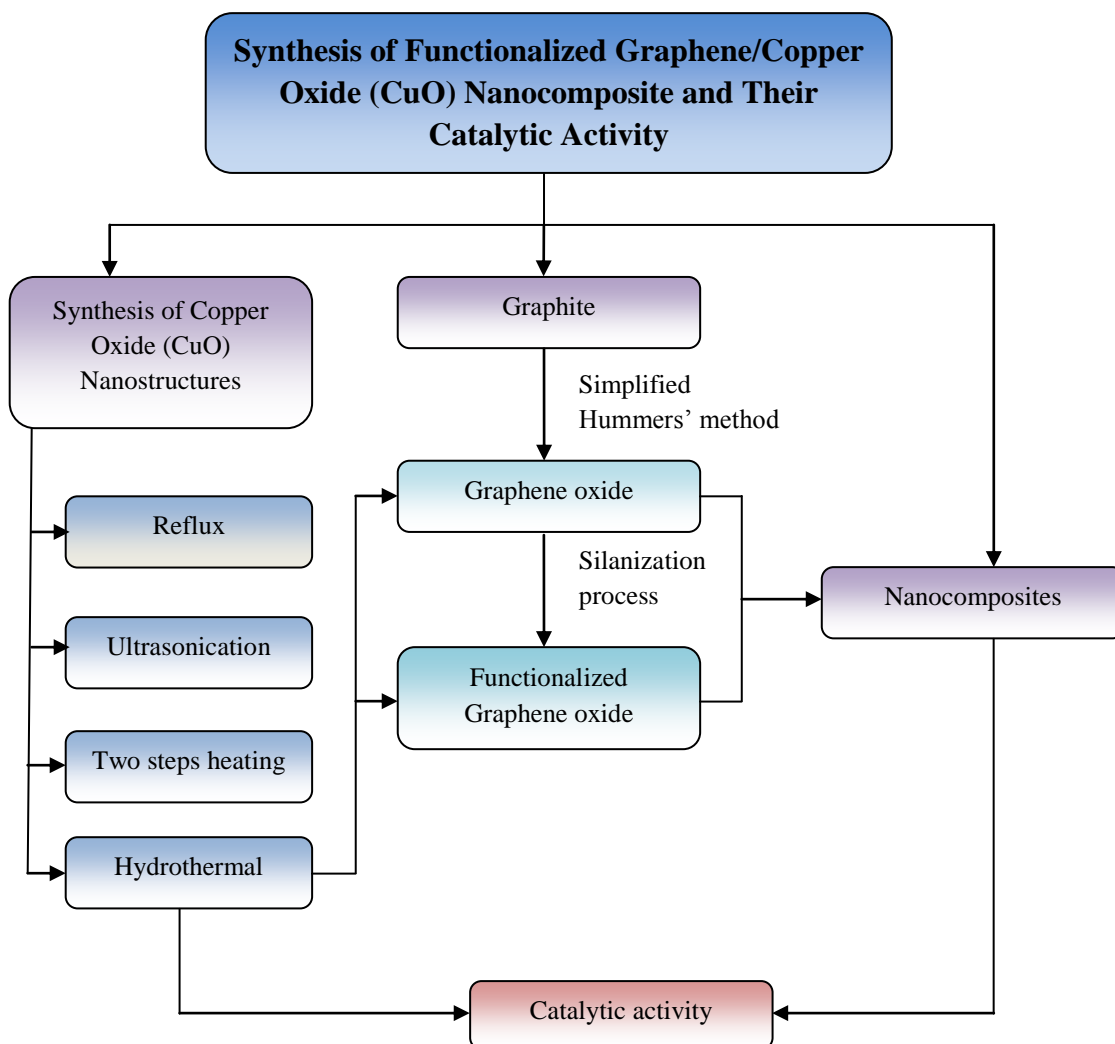


**Figure 3.1:** Research methodology design.

### 3.2 Materials

All of the chemical reagents used were analytical grade and were utilized without further purification in this experiment. The materials used in this work are listed in **Table 3.1**.

**Table 3.1:** List of chemicals that were being used in this work.

<i>Types</i>	<i>Molar mass (g/mol)</i>	<i>Brand</i>
<b>1. Copper acetate monohydrate – powder (Cu(CH<sub>3</sub>COO)<sub>2</sub>·H<sub>2</sub>O)</b>	199.65	Bendosan
<b>2. Potassium permanganate – powder (KMnO<sub>4</sub>)</b>	158.04	R&M Chemicals
<b>3. Cetyltrimethylammonium bromide - powder (CTAB)</b>	364.50	Sigma-Aldrich
<b>4. Sodium hydroxide – pellets (NaOH)</b>	40.00	System
<b>5. Graphite – powder</b>	12.00	Asbury Graphite Mills, Inc.
<b>6. Hydrogen peroxide – liquid (H<sub>2</sub>O<sub>2</sub>, 35 %)</b>	34.01	System
<b>7. Aqueous ammonia – liquid (NH<sub>3</sub>·H<sub>2</sub>O, 25 wt %)</b>	35.05	Riedel-deHaen
<b>8. Sulfuric acid – liquid (H<sub>2</sub>SO<sub>4</sub>, 95-97 %)</b>	98.08	Merck
<b>9. Phosphoric acid – liquid (H<sub>3</sub>PO<sub>4</sub>)</b>	98.00	Fisher Scientific
<b>10. Hydrochloric acid – liquid (HCl fuming, 37 %.)</b>	36.46	Merck
<b>11. Acetone – liquid</b>	58.08	System
<b>12. Absolute ethanol – liquid</b>	46.07	Hmbg Chemical
<b>13. N-(trimethoxysilylpropyl) ethylenediamine triacetic acid – liquid (EDTA-silane)</b>	292.24	Sigma-Aldrich
<b>14. Methanol – liquid (CH<sub>3</sub>OH)</b>	32.04	System

### 3.3 Sample preparation

Sample preparation is divided into three stages. In the first stage, four different methods had been chosen to prepare CuO. The best method that yields CuO with excellent catalytic activity would be selected to fabricate the nanocomposite. In the second stage, GO had been prepared by oxidation technique with graphite flakes as the precursor. Next, this GO undergone functionalization via silanization process to form FGO. At the third stage, the step of preparing the nanocomposite between CuO and FG were being discussed, as well as rGO hybridized with CuO as a comparison. Three different weight ratios had been chosen to make the nanocomposite for the purpose of finding the best ratio to produce best nanocomposite with excellent catalytic activity.

#### 3.3.1 Different ways of preparing CuO with different morphologies

The first stage consists of series of experimental methods for synthesizing CuO in which each method is chosen for its own properties, in term of temperature and processing time taken to complete the process. **Table 3.2** shows the overview of methods in synthesizing CuO.

**Table 3.2:** Overview of methods in synthesizing CuO.

<i>Method</i>	<i>Temperature (°C)</i>	<i>Time (hour)</i>
<b>Reflux</b>	90	2
<b>Hydrothermal</b>	180	24
<b>Ultrasonication</b>	-	2
<b>Two steps heating</b>	90	24

### 3.3.1.1 Preparation of CuO using reflux method

The first method of preparing CuO is by a simple reflux method (**Figure 3.2**). In a typical procedure, 0.5 g copper acetate monohydrate  $[\text{Cu}(\text{CH}_3\text{COO})_2 \cdot \text{H}_2\text{O}]$  was dissolved in 25 ml deionized water (DIW) with violent magnetic stirring.

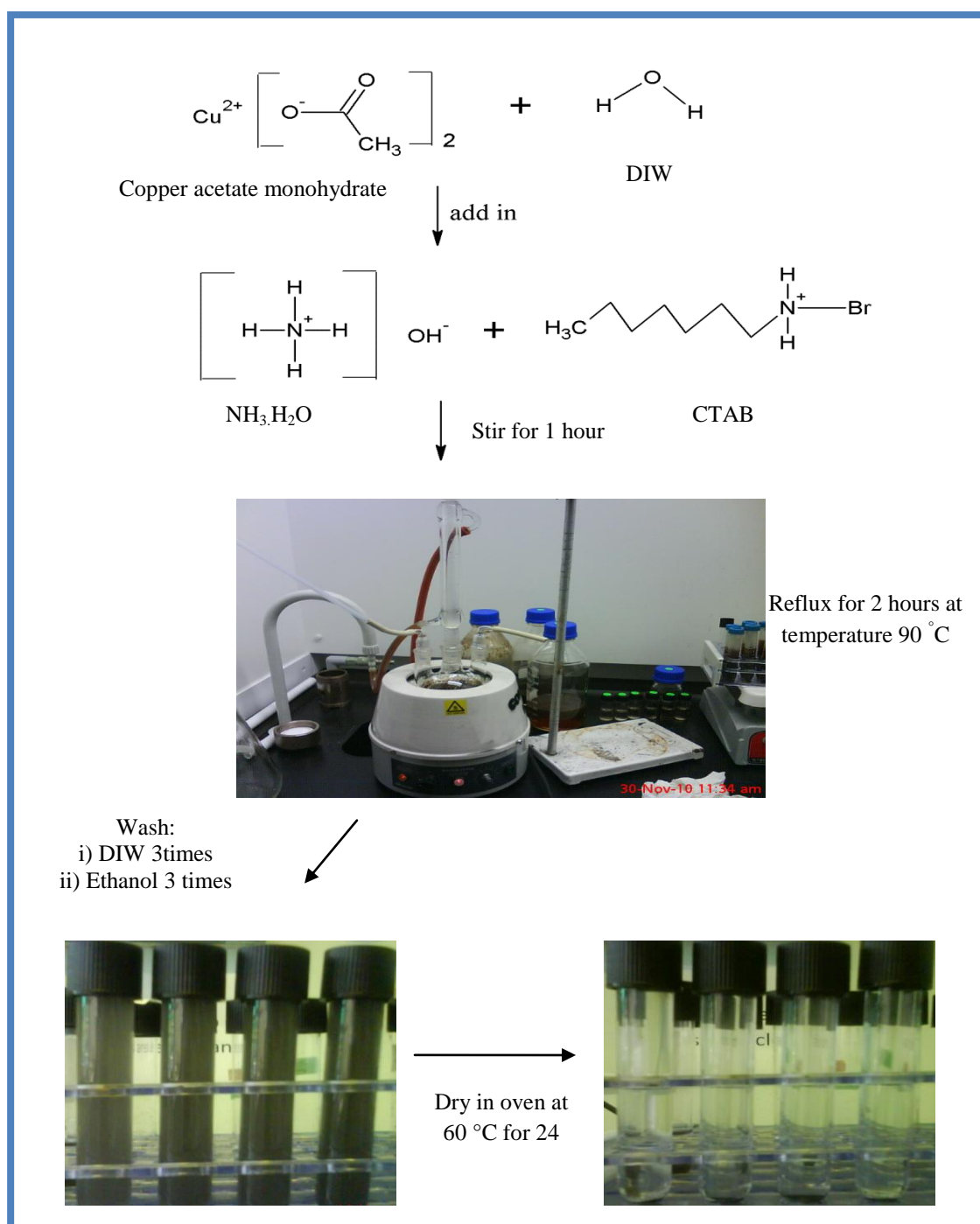


**Figure 3.2:** Flow chart of synthesis of CuO nanostructure via reflux method.

Then, 10 ml ammonia solution ( $\text{NH}_3 \cdot \text{H}_2\text{O}$ ) (25 weight%) and 0.1 g CTAB were slowly added into the above solution while stirring. The mixed solution was stirred for 1 hour. Subsequently, the resulting mixture was refluxed for 2 hours at temperature  $90^\circ\text{C}$  under constant stirring. The resulted sample was cooled to room temperature before separated using centrifugation and washed three times with DIW and ethanol respectively. Finally, the final product was dried in an oven at  $60^\circ\text{C}$  for 24 hours.

### 3.3.1.2 Preparation of CuO using the hydrothermal method

The CuO was prepared by hydrothermal as the second method (**Figure 3.3**). In the typical processes, 0.5 g  $\text{Cu}(\text{CH}_3\text{COO})_2 \cdot \text{H}_2\text{O}$  was dissolved in 25 ml DIW. The mixture was stirred for 10 minutes before added with 10 ml  $\text{NH}_3 \cdot \text{H}_2\text{O}$  (25 weight%) and 0.1 g CTAB into the solution under stirring.

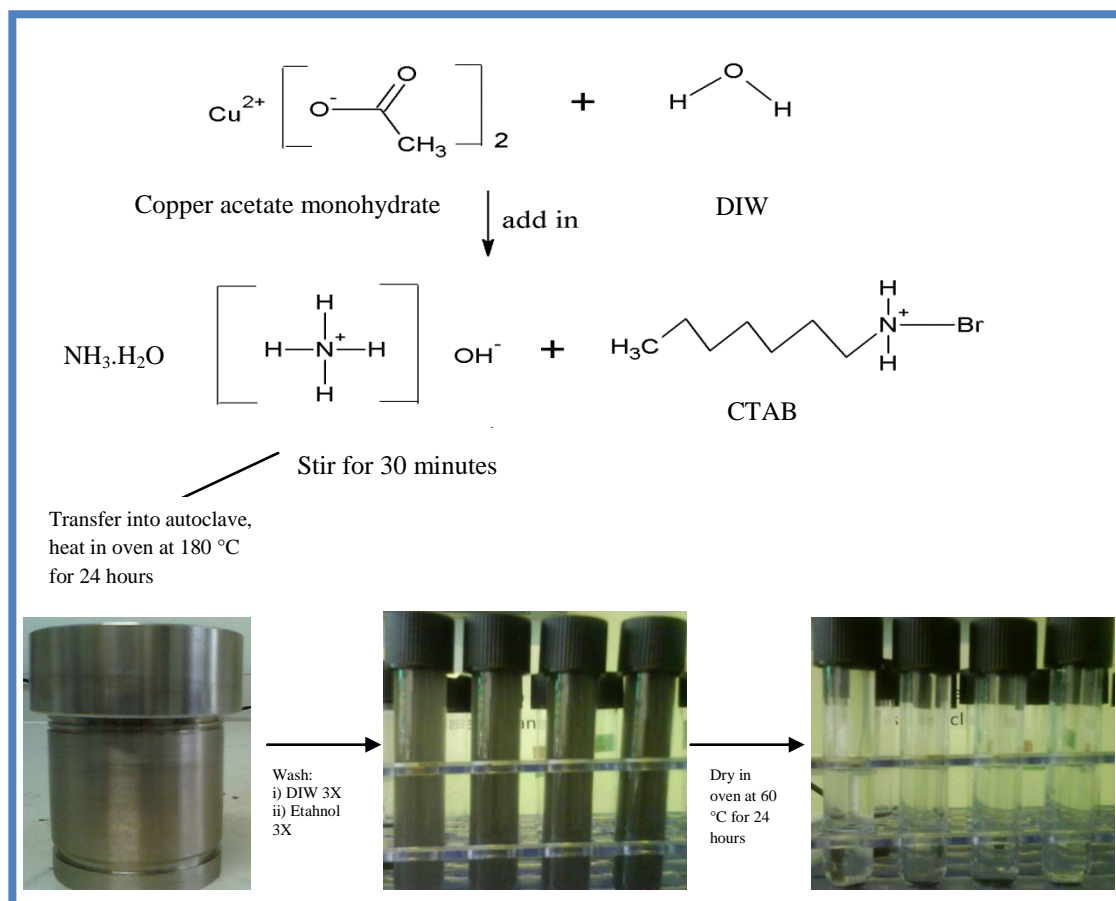


**Figure 3.3:** Flow chart of synthesis of CuO nanostructure via hydrothermal method.

The mixed solution was stirred for 30 minutes. Subsequently, the mixture was transferred into steel autoclave and heated in oven at 180 °C for 24 hours. The resulted solution was cooled naturally to room temperature before centrifugation and washed three times with DIW and ethanol respectively. Finally, the final product was dried in an oven at 60 °C for 24 hours.

### 3.3.1.3 Preparation of CuO using ultrasonication method

The third method of synthesized CuO is by ultrasonication method (**Figure 3.4**). Typically, 0.5 g  $\text{Cu}(\text{CH}_3\text{COO})_2 \cdot \text{H}_2\text{O}$  and 0.1 g CTAB were mixed well through grinding. Then, the mixture was transferred into a beaker with mixture of 25 ml DIW and 10 ml  $\text{NH}_3 \cdot \text{H}_2\text{O}$  (25 weight%) and ultrasonicated for 2 hours. Finally, the resultant sample was washed with DIW and ethanol 3 times each and dried in oven for 24 hours at temperature 60 °C.

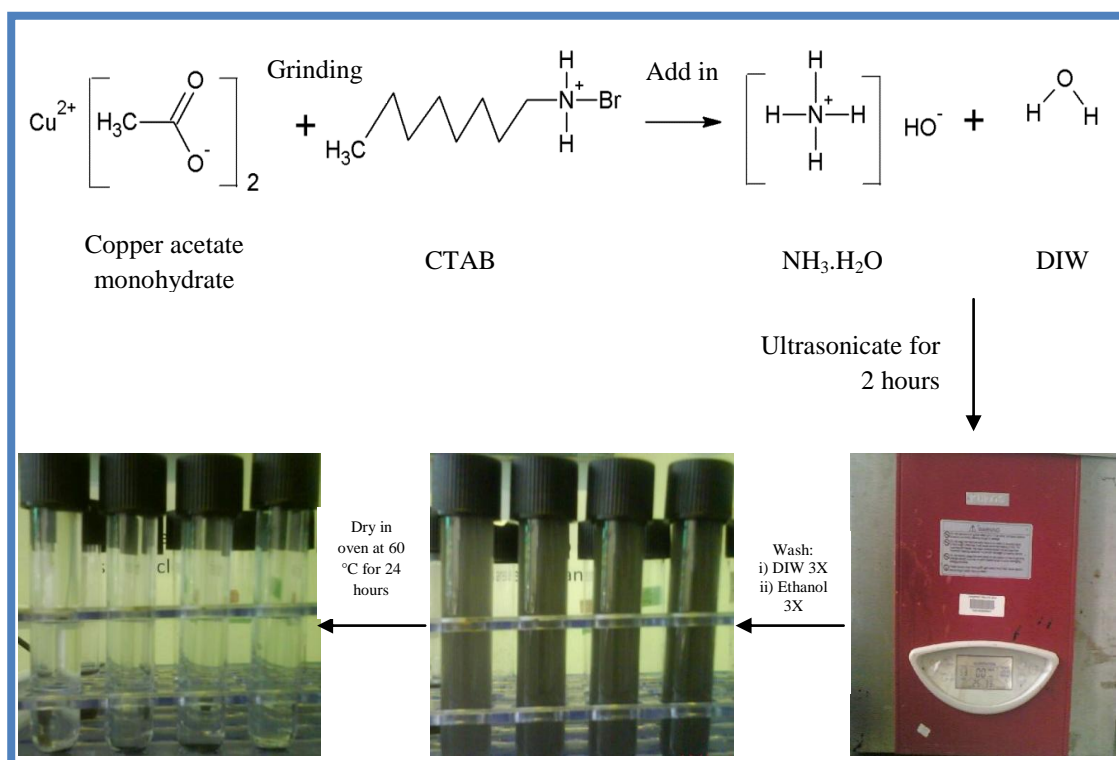


**Figure 3.4:** Flow chart of synthesis of CuO nanostructure via ultrasonication method.

### 3.3.1.4 Preparation of CuO using the two steps heating method

Another method of producing CuO is using a two steps heating method that only involves two setup steps (**Figure 3.5**). In the first step, 0.5 g  $\text{Cu}(\text{CH}_3\text{COO})_2 \cdot \text{H}_2\text{O}$  was dissolved in 10 ml  $\text{NH}_3 \cdot \text{H}_2\text{O}$  (25 wt%). The solution was stirred for 2 hours. Then, 25 ml DIW was added slowly into the above solution with stirring. The mixed solution was continued stirring for 1 hour. The final solution was labeled as  $\text{Cu}(\text{OH})_2$ . In the second step, 5 ml  $\text{Cu}(\text{OH})_2$  (0.2 M) and 0.1 g CTAB were dispersed in DIW with constant stirring for 1 hour. The resulting mixture was heated to 90 °C for 2 hours under stirring in the silicon oil bath. The mixed solution was let stirring overnight. Subsequently, the final product was washed with DIW and ethanol three times, respectively and dried in oven at 60 °C for 24 hours.

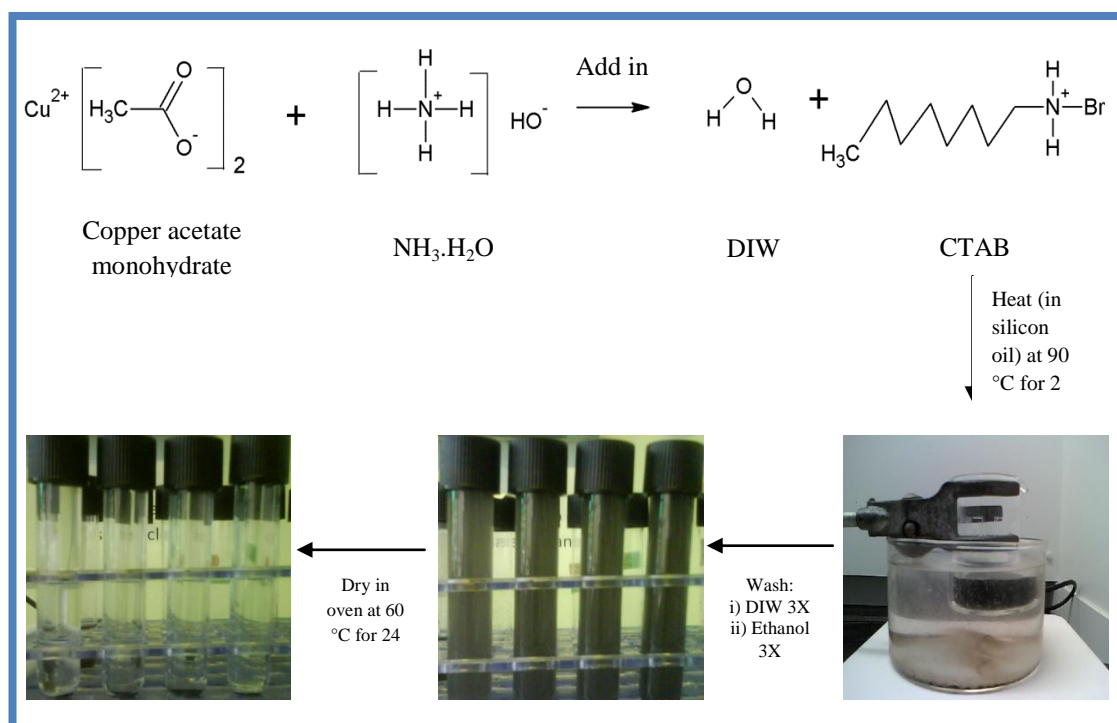


**Figure 3.5:** Flow chart of synthesis of fibril-like CuO nanostructure using two steps heating method.

### 3.3.2 Preparation of GO and FGO

The second stage was done to prepare GO and FGO from graphite flakes as the precursor. GO was synthesized via the simplified Hummers method, by oxidation of graphite flakes in the acidic solution with the presence of  $\text{KMnO}_4$ . Next, this GO undergone a surface modification by the chemically functionalization process via silanization. The GO sheets were silanized with EDTA-silane where a new functional group was introduced to the surface of GO.

#### 3.3.2.1 Synthesis of GO using simplified Hummers' method

In this work, GO had been prepared using Simplified Hummers' method (**Figure 3.6**). Firstly, we need to prepare a 400 ml mixture containing concentrated  $\text{H}_2\text{SO}_4$  and concentrated  $\text{H}_3\text{PO}_4$  with ratio 9:1. Then, added 3.0 g of graphite into the mixture. Next, 18.0 g of  $\text{KMnO}_4$  was added slowly and the solution was left to oxidize for 3 days with continuous stirring.

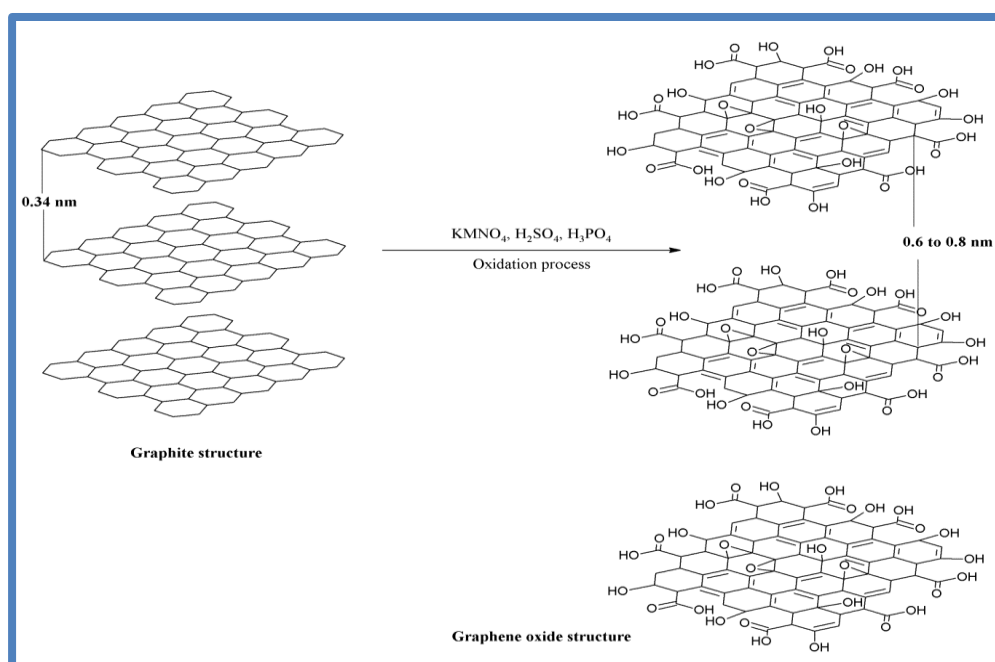


**Figure 3.6:** Schematic diagram of synthesizing GO.

After 3 days, 400 ml ices with 20 ml of 35 % H<sub>2</sub>O<sub>2</sub> were poured into the solution. This would stop the oxidation process. The solution was left for a few minutes to remove the excess KMnO<sub>4</sub>. Finally, the solution was washed with 1 M hydrochloric acid (HCl) for 3 times and continued with DIW for 6 times. Centrifuged it at 9600 rpm for 10 minutes.

### 3.3.2.2 Synthesis of FGO via silanization process

This process was divided into 2 that are the preparation part and the washing part (**Figure 3.7**). In the preparation part, 200 mg of dry GO was dispersed in 300 ml of absolute ethanol and was labelled as (A). The solution was ultrasonicated for 1 hour. Next, 1g of EDTA-silane was well-mixed in 15 ml DIW and was labelled as (B). Then part (A) was poured in a round bottom flask and refluxed at temperature 85 °C. Part (B) was then slowly added in part (A) and continued to reflux for 16 hours while stirring. For the washing part, 200 ml methanol was added into the solution and let it settled down for a few minutes. Then, the solution was washed 2 times with acetone/DIW with ratio (60 ml : 40 ml) before continued to wash with ethanol for 3 times. Proceeded with centrifugation at 4000 rpm for 10 minutes. Finally, the sample was dried at 80 °C for 12 hours.

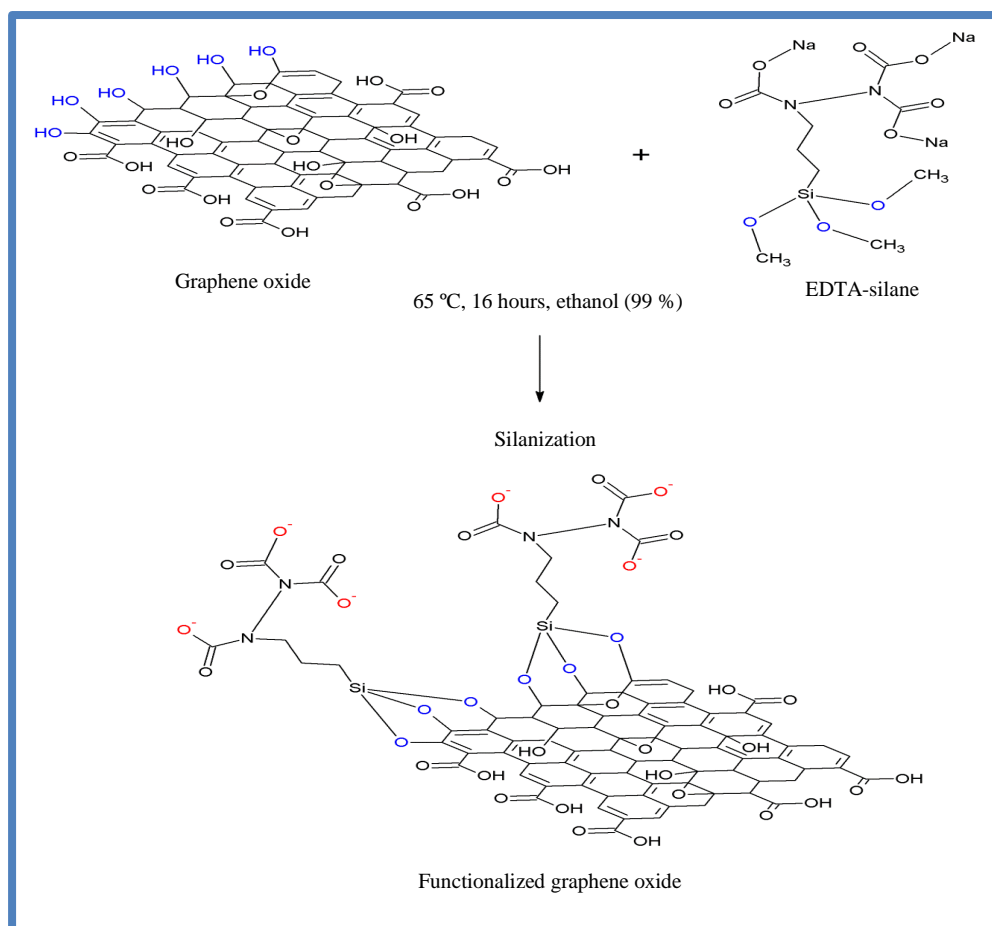


**Figure 3.7:** Schematic diagram of synthesizing FGO.

### 3.3.3 Hydrothermal process for synthesized nanocomposite

The route to produce nanocomposite via hydrothermal method was presented in this third stage where FGO and also GO were used for comparison, as the platform for deposition of copper particles. It has been reported before that FGO and copper hydroxide ( $\text{Cu}(\text{OH})_2$ ) could be transformed into FG and  $\text{CuO}$ , respectively through a dehydration/dehydroxylation process under the hydrothermal condition. In this work, we focussed on preparing FG hybridized with  $\text{CuO}$ . In order to investigate the influence of mass ratio on the nanocomposite, the samples were prepared with 2 mg, 20 mg and 30 mg of FGO, whereas the mass for copper precursor is constant.

### 3.3.3.1 Synthesis of rGO/CuO nanocomposite by hydrothermal method

For synthesis of rGO/CuO nanocomposite via the hydrothermal method (**Figure 3.8**), a 2 ml of 2 mg/ml GO was dispersed in 20 ml DIW. Then, a 1.2 ml  $\text{Cu}(\text{OH})_2$  (0.1 M) was added in the solution. The amount of NaOH added into the solution was controlled until it reached a pH value of 10. Next, the solution was stirred for 1 hour at temperature  $90\text{ }^\circ\text{C}$ . After 1 hour, the solution was transferred into the Teflon lined stainless steel autoclave for hydrothermal process. The autoclave was sealed, maintained at the temperature  $180\text{ }^\circ\text{C}$  for 24 hours.

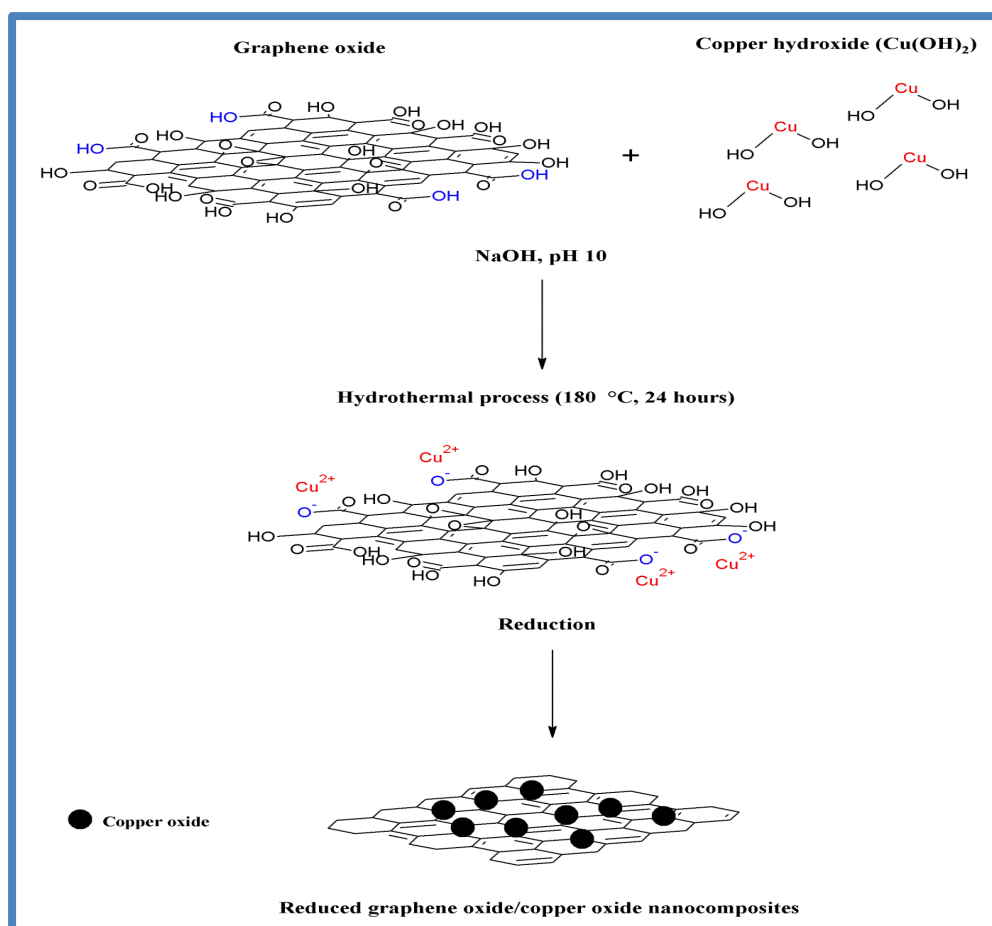


**Figure 3.8:** Schematic diagram for the formation of rGO/CuO nanocomposite.

### 3.3.3.2 Synthesis of FG/CuO nanocomposite by hydrothermal method

Firstly, the FGO (2 mg, 20 mg and 30 mg) were dispersed in 20 ml DIW (**Figure 3.9**). Then, 1.2 ml  $\text{Cu}(\text{OH})_2$  (0.1 M) was added in the solution. The amount of NaOH added into the solution was controlled until it reached a pH value of 10. Next, the solution was stirred for 1 hour at temperature  $90\text{ }^\circ\text{C}$ . The solution was then transferred into the autoclave Teflon for hydrothermal process and left in the oven for 24 hours at temperature of  $180\text{ }^\circ\text{C}$ .

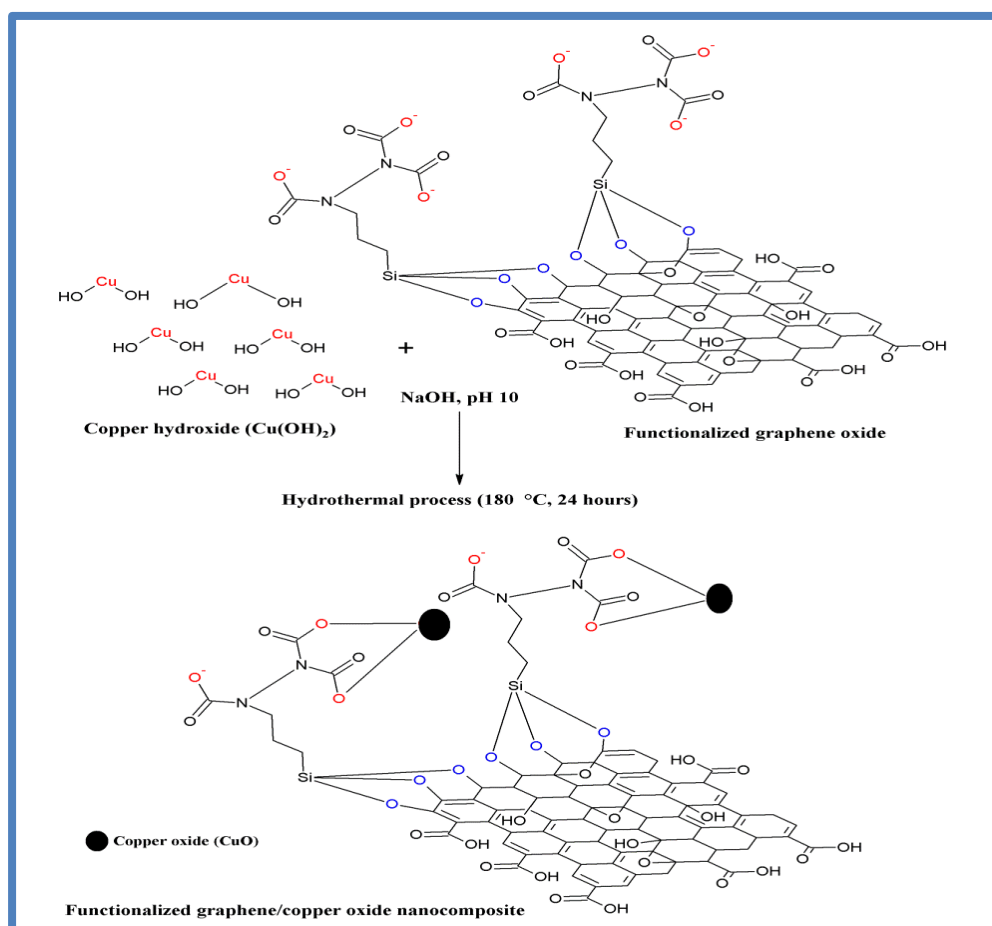


**Figure 3.9:** Schematic diagram for the formation of FG/CuO nanocomposite.

### 3.4 Characterization techniques

Characterization has been one of the foundational pillars of material science in order to gain knowledge and understand the properties, structure, mechanisms and etc of our samples. The second section of this chapter contains the characterization techniques that has been done to characterize the samples. The characterization techniques described in this section is shown in **Figure 3.10**. The analysis using Fourier transform infrared (FT-IR), micro Raman, thermogravimetric analysis (TGA) and X-ray diffraction (XRD) were carried out to determine the elemental composition. TGA was also used to study the amount of weight loss over certain temperature. The morphologies and dimensions of the nanocomposites were examined under field emission scanning electron microscopy (FESEM) and transmission electron microscopy (TEM). The optical properties of the samples were characterized using the UV-visible (UV-vis) spectrometer.

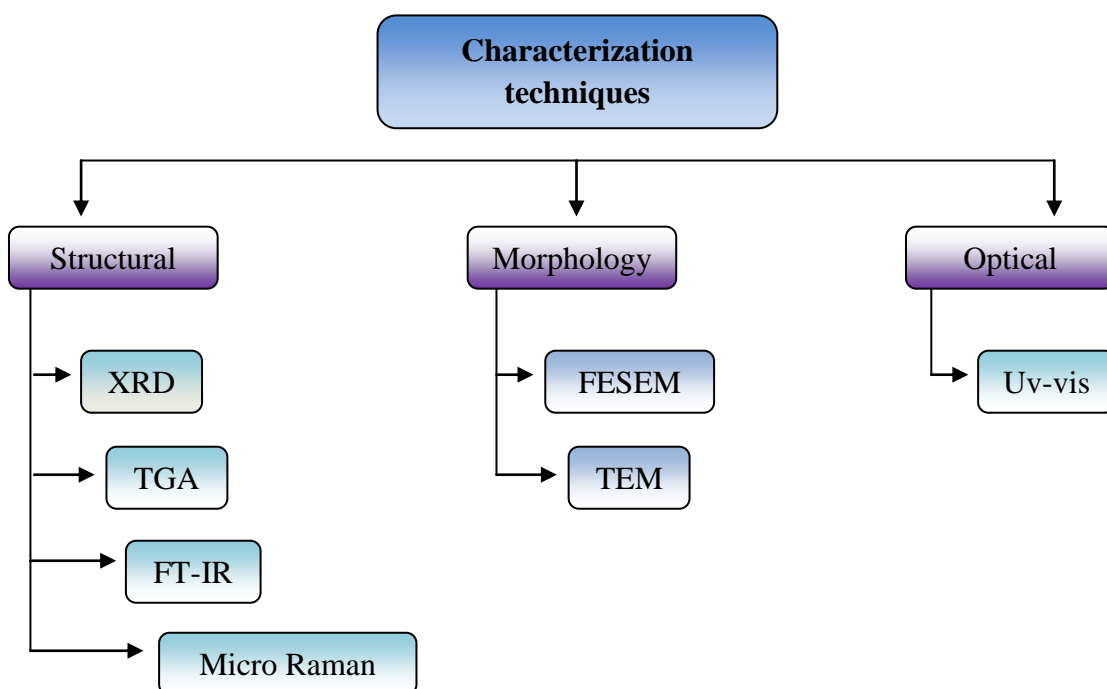


**Figure 3.10:** Characterization techniques involved in this research.

### 3.4.1 Determination of the crystalline structure by XRD

XRD is one of a crucial tools to determine the crystalline structures and phase composition of materials. In this research, XRD pattern of the solid powder was analyzed by Philip XRD (**Figure 3.11**) with monochromatized Cu K $\alpha$  radiation and wavelength,  $\lambda = 1.5418 \text{ \AA}$ . The system operated at a scanning rate of  $0.02^\circ$  per second to over a  $2\theta$  range of  $10^\circ$  to  $80^\circ$ . The sharpness of the diffraction peak pertain to their crystal structure where crystalline has a sharp peak characteristic. While broad peaks are characteristic for amorphous structure. Besides that, the Miller index, diffraction peak position and relative intensity of unknown materials can be identified by comparing the diffraction data with diffraction pattern from Joint Committee on Powder Diffraction Standard (JCPDS). JCPDS is a non-profit scientific organization that collecting, editing, publishing, and distributing powder diffraction data for the identification of inorganic and organic materials with a crystal structure.



**Figure 3.11:** Philip XRD for crystal structure and composition studies.

### 3.4.2 Determination of amount of weight loss over certain temperature by TGA

TGA is a technique that can characterize materials with losing or gaining weight due to decomposition, oxidation or dehydration after going through some treatment. It allows studies of the rate of change in the weight of materials as a function of temperature or time under a controlled atmosphere. These measurements are important to elaborate the composition of materials as well as to predict their thermal stability at up to certain temperatures and also the oxidative stability of the material. For the compositional analysis, TGA is a useful tool to estimate the amount of each components in the material by calculating the onset temperature of degradation or volatilization. In this work, TGA measurement was performed using TG 209 F3 Tarsus thermal analyzer (**Figure 3.12**) that operates over the temperature range of 20-1000 °C with a scan rate of 20 °C/min. The sample sent to TG analysis was in the powder form because it has a larger surface area which is important to improve weight loss resolution and temperature reproducibility.

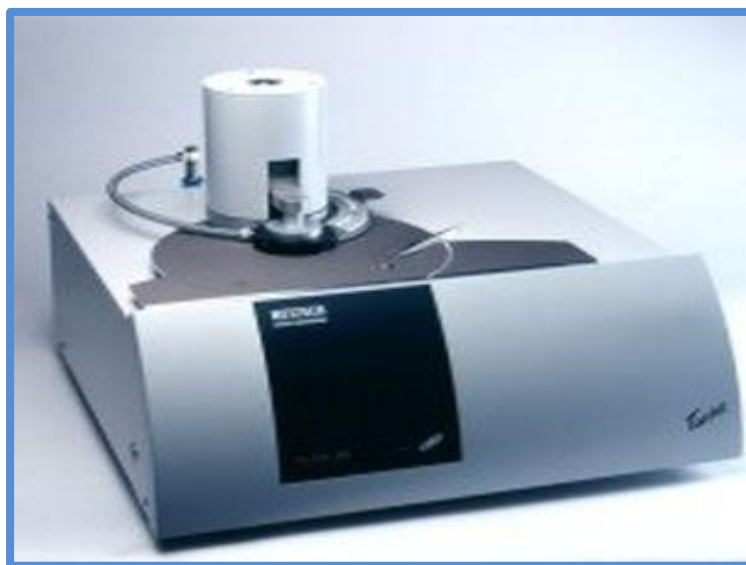


**Figure 3.12:** TG 209 F3 Tarsus thermal analyzer to study the rate of change in weight over temperature or time.

### 3.4.3 FT-IR for chemical bonding studies

FT-IR spectroscopy was performed with Perkin Elmer Instrument FT-IR version 5.0.1 as shown in **Figure 3.13** with scanning spectra recorded in the range of 400 to 4000  $\text{cm}^{-1}$ . The samples were prepared using potassium bromide (KBr) method where the samples were triturate in the powder form with KBr powder. The trituration of KBr is important to avoid light scattering due to the large size of the KBr crystals. Next, the mixture was crushed in a mechanical die press to form a translucent pellet. The pellet was held by a sample holder so that the IR beam could pass through it.



**Figure 3.13:** Perkin Elmer Instrument FT-IR version 5.0.1 for chemical bonding studies.

The advantages of KBr method are:

- I. The small amount of sample was used as we want a translucent pellet in order for IR beam to pass through it.
- II. KBr transmits most of the IR region giving an excellent spectrum. This is because KBr is an alkyl halide, one of the compounds which do not absorb the provided radiations of IR and hence do not exhibit its absorption pattern in the graph.

- III. Does not react with our sample which needed to be analyzed.

The main purpose of studying the FT-IR spectrum is to identify the chemical bonding inside our material as well as its interaction. Besides that, FT-IR can also provide us with other information such as:

- I. Identify unknown material.
- II. Determine the amount of components in a mixture.
- III. Characterization of chemical reaction.

We could detect the interaction between the components by taking into account several factors such as:

- I. Observed the changes in the intensity of the band.
- II. Detected the presence or loss of the band.
- III. Examined the shift of the band.

#### **3.4.4 Structural characteristics determined by micro Raman spectroscopy**

Micro Raman spectroscopy is a powerful and widely used to characterize ordered and disordered crystal structures of carbon materials because it has a high sensitivity to the electronic structures. Micro Raman spectroscopy is also a vital tool to characterize graphene for example to determine the number of layers graphene. The 2D peak in graphene is assigned to two phonons with opposite momentum in the highest optical branch so by study the shape and shift of the 2D peak we could determine the number of layers in graphene. In the case of nanocrystals, the study of the phases and structures of oxide systems especially on the decreasing in the microcrystal size could be done by investigating the shifted in Raman frequency and also broaden by bandwidth.

In this work, the micro Raman measurement of the samples was recorded using Renishaw Raman Microscope (**Figure 3.14**) linked with a 514 nm line of an argon ion laser as the excitation source that performed at room temperature. The Raman signal was integrated over 30 seconds for each spectrum started from 200 to 4000  $\text{cm}^{-1}$ . The specimen was prepared by the drop casting method on a clean glass substrate. The glass slide needs to undergo a cleaning process before it can be used to ensure there is no contaminates. The cleaning procedure for glass is similar to quartz cleaning procedure.



**Figure 3.14:** Renishaw Raman Microscope for structural characterization.

### 3.4.5 FESEM for morphology and structure study

The surface features and particles size or shape of the sample were studied by a high resolution field emission scanning electron microscope. In this work, the images were taken using FEI Quanta 400F FESEM as shown in **Figure 3.15**. The elemental composition of the samples could be observed by energy dispersive X-ray spectroscopy (EDX) as it has been combined with this FESEM model. The field emission gun electron source of this model provides high current to enable imaging up to 3nm

resolution and its magnification can achieve up to 250,000 times. All the samples being tested were in the powder form.



**Figure 3.15:** FEI Quanta 400F FESEM for morphology and structural study.

#### 3.4.6 Morphology characterization using TEM

TEM is a microscopy technique which employs energetic electrons that transmitted through specimens where it provides information pertaining to morphological, compositional and crystallographic of the samples. TEM is also one of a crucial technique to verify the formation of nanocomposite. This microscopy possesses the same basic principle as light microscopy except that its exchange photon with electron which produce shorter wavelength. In this work, TEM images were acquired from Hitachi H7100 TEM with an accelerating voltage of several 100 kV. TEM used to analyse samples in this work is shown in **Figure 3.16**. The specimen preparations started by adding a small amount of powders in ethanol and ultrasonicated it for several minutes to disperse particles well. Next, place a small drop of the suspension on the copper coated grid and let the solvent evaporate for a few minutes. The specimen preparation was actually the crucial part. It is important to ensure that the

suspension was dilute enough and only a small drop of it was deposited on the copper grid in order to form a small thickness that is less than 100 nm. This is because electron that accelerates at several 100 kV can only penetrate the specimen with a thickness less than 100 nm.



**Figure 3.16:** Hitachi H7100 TEM for morphology study.

#### **3.4.7 Optical properties measured by UV-vis spectroscopy**

The UV-visible absorption spectra of the samples were taken by Thermo Scientific Evolution 300 ultraviolet-visible (UV-vis) spectrometer, which works in the range between 200 to 800 nm at room temperature as shown in **Figure 3.17**. In the investigation of optical properties, the samples were ultrasonically dispersed in deionized water before poured the suspension in quartz cuvettes to run the measurement.



**Figure 3.17:** Thermo Scientific Evolution 300 ultraviolet-visible (UV-vis) spectrometer for optical characterization.

UV-vis spectroscopy is widely used method to investigate the following aspects:

- I. Structure elucidation of organic compounds shown by the location of the peak and combination of peaks.
- II. Characterize those types of compounds which absorbs UV radiation through comparison of the measured spectrum with a reference spectrum.
- III. Quantitative determination of compounds that absorb UV radiation by extract the data using Beer's law.
- IV. Confirmation of the chemical changes that occur by examining the shifting in wavelength an its intensity.

#### **3.4.8 Catalytic activity**

FG hybridized with CuO is believed could produce an efficient catalyst toward removal of dye in water waste treatment. To investigate the catalytic activity of the final product, 5 mg of each sample was added into a solution of 25 ml of MB (10 mg/L) and 5 ml of H<sub>2</sub>O<sub>2</sub>. The catalytic reaction was carried out at room temperature after stirring for 5 minutes. The concentration of MB was analyzed every 1 hour using a Thermo Scientific Evolution 300 ultraviolet-visible (UV-vis) spectrometer.

## **Chapter 4 Results and Discussion**

### **4.1 Overview**

In this chapter, the results and discussion regarding the steps of experimental processes are presented. The results are presented in three main parts: 1) synthesis of CuO nanostructures 2) synthesis of GO, FGO and FG and 3) synthesis of rGO/CuO and FG/CuO nanocomposites. Each of these parts comes with the discussion of its formation mechanism and several characterization techniques such as FESEM, TEM and etc. The study on catalytic performance of the CuO and nanocomposite samples are discussed in part 1 and part 3.

### **4.2 Results for synthesis of CuO nanostructures**

In the first part of this chapter, the results obtained from characterizing CuO nanostructures samples that had been fabricated using four different methods are presented. Some discussions about its possible growth mechanism are also being demonstrated briefly. All CuO samples had been characterized by using several instruments to study the structural and morphological as well as its catalytic activity, as presented below. The characterization tools that we used includes XRD, FT-IR, micro Raman, FESEM, TEM and lastly the catalytic activity.

#### **4.2.1 Structural characterization: XRD, micro Raman and FT-IR spectroscopy analysis**

When the reaction was complete, a black precipitate would form (for all four methods). These products went throughly the washing process before it was dried in the oven for 24 hours at temperature 60 °C. The final products in the form of black colored powder were sent for XRD characterization. The XRD patterns for CuO

nanostructures that had been synthesized by using reflux, hydrothermal, ultrasonication and the two steps heating method are shown in **Figure 4.1**. The diffraction peaks at  $35.2^\circ$ ,  $38.5^\circ$ ,  $48.6^\circ$ ,  $53.3^\circ$ ,  $58^\circ$ ,  $61.3^\circ$ ,  $65.9^\circ$ , and  $67.9^\circ$  are assigned to the (0 0 2), (1 1 1), (2 0 2), (0 2 0), (2 0 2), (1 1 3), (0 2 2), and (1 1 3) planes of monoclinic CuO. All these peaks are consistent with the data of JCPDS 00-044-0706 (**Figure 4.1 (a)**). The lattice parameters are  $a = 4.653 \text{ \AA}$ ,  $b = 3.410 \text{ \AA}$  and  $c = 5.108 \text{ \AA}$  with the interlayer spacing is in the range of 2.33 to 2.53  $\text{\AA}$ . The absence of other peaks indicates high purity of the samples.

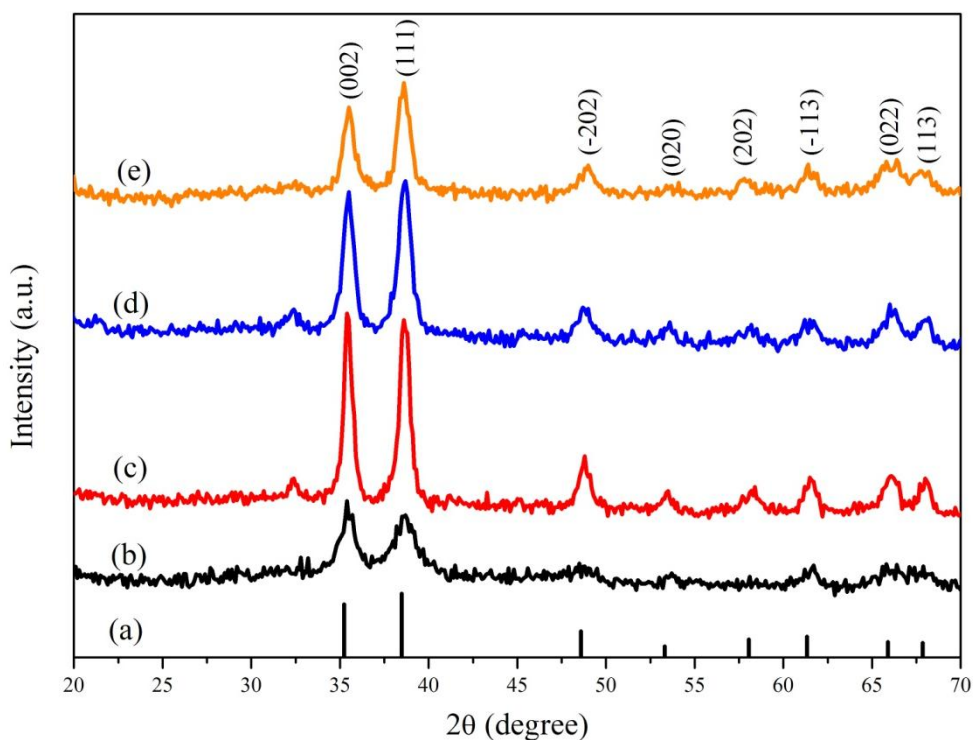


**Figure 4.1:** XRD patterns of (a) standard and CuO nanostructures synthesized by (b) reflux, (c) hydrothermal, (d) ultrasonication and (e) two steps heating methods.

Moreover, the broadening of the major peaks indicates the formation of nanometric particle size (*Maji et al., 2010*). Hydrothermal method with the highest processing temperature produces the largest crystallite size. This result demonstrates clearly the growth in crystallite size of the CuO as a function of the reaction

temperature (*Hong et al., 2002*). Furthermore, one can find that the CuO produced using ultrasonication and two steps heating methods shows that the intensity of the diffraction peaks are similar to the standard pattern. However, CuO samples produced using reflux and hydrothermal methods have higher intensity of the diffraction peak at (002) plane if compared to that of the standard. This indicates that the growth direction of the flower-like and rod-like CuO is along the (002) plane direction.

Based on the XRD results, the degrees of crystallization are strongly associated to the reaction temperature. The sample synthesized using the hydrothermal method that was carried out at the highest temperature at 180 °C has the most intense peak profiles, reflecting the strongest crystalline structure. The samples produced using the reflux and two steps methods which were carried out at lower temperature (90 °C), expectedly, has lower crystallinity. These findings are in agreement with *Carnes et al. (Carnes et al., 2002)*.

Interestingly, ultrasonication is able to fabricate a sample with a high degree of crystallinity, even without the use of high temperature treatment which is similar to the study reported by *Kim et al. (Kim et al., 2006)*. The localized hot spot created during bubble collapse in ultrasonication method supplied the reaction with enough energy to form CuO with good crystallinity. The increase in crystallinity also implies that Ostwald ripening (crystallites grow at the expense of smaller ones) is the underlying mechanism in the morphology evolution of CuO nanostructures (*Yang et al., 2011*). This result reinforces the theory we make regarding the possible mechanism involved in the formation of CuO nanostructures by ultrasonication method.

Some of the obtained black powder samples were then dissolved in the ethanol by using ultrasonication for 5 minutes and dropped directly on the cleaned glass slide before being tested by micro Raman characterization. Micro Raman spectroscopy has been widely used to investigate the microstructure nature of the nano-sized materials due to the higher sensitivity of the probe to the local atomic arrangements and the vibrations of the materials (Zi *et al.*, 1996). In general, CuO belongs to the  $C_{2h}^6$  space group with two molecules per primitives' cell. One can find the zone center Raman active normal modes  $\Gamma_{RA} = 4A_u + 5B_u + A_g + 2B_g$ . There are three acoustic modes (Au+2Bu), six infrared active modes (3Au+3Bu), and three Raman active modes (Ag+2Bg) (Fuentes *et al.*, 2010).

**Figure 4.2** shows the micro Raman spectra of the CuO nanostructures. It is clearly seen that there are four prominent peaks are obtained in the spectra at a position about 285, 340, 611 and 1100  $\text{cm}^{-1}$ , respectively, in which all the peaks are in agreement with the result of the standard CuO materials reported by Xu and co-worker (Xu *et al.*, 1999). Moreover, there are no  $\text{Cu}_2\text{O}$  modes were detected in the spectrum which suggesting the high purity of CuO samples prepared by these methods (Reimann *et al.*, 1989). These results are in a good agreement with the XRD results presented earlier. In comparison with the vibrational spectra of a CuO single crystal that had been reported by other researchers before, the first three peaks at 285, 340 and 611  $\text{cm}^{-1}$  can be assigned to a one-phonon transition while the peak at 1100  $\text{cm}^{-1}$  is attributed to a multi-phonon transition with the second one being the weakest and the third and forth being broad. The peak at 285  $\text{cm}^{-1}$  is designated to the  $A_g$  mode while the peaks at 340 and 611  $\text{cm}^{-1}$  are designated to the  $B_g$  modes. The broad peak at 1100  $\text{cm}^{-1}$  is corresponding to the  $2B_g$  mode, which arise due to the anharmonic coupling between

phonons in polar solid and its intensity is related to the electron-phonon interaction (Wenzhong Wang *et al.*, 2010).

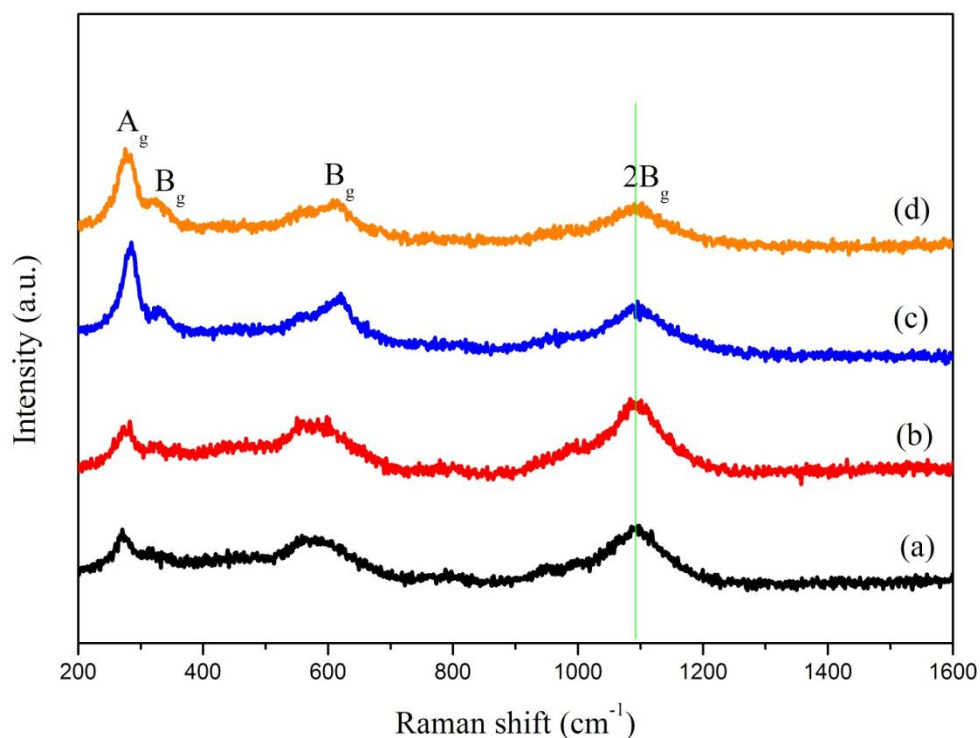


**Figure 4.2:** Micro Raman scattering spectra of CuO prepared using (a) reflux, (b) hydrothermal, (c) ultrasonication and (d) two steps heating methods.

**Table 4.1** shows the effects of different preparation methods on the micro Raman parameters such as peak position and intensity. The position and intensity of the two-phonon scattering band ( $2B_g$ ) varies according to the morphology, size and crystallinity of the nanostructure (Wenzhong Wang *et al.*, 2010).

**Table 4.1:** Effects of different preparation methods on the micro Raman parameters such as peak position and intensity.

<i>Preparation method</i>	<i>Reflux</i>	<i>Hydrothermal</i>	<i>Ultrasonication</i>	<i>Two steps heating</i>
$2B_g$ peak position ( $cm^{-1}$ )	1100	1108	1104	1103
Peak intensity	680	1000	510	430

Volanti *et al.* also reported that there are three factors that affect the peak position in micro Raman spectrum which are the preparation method, geometry and crystal structure (Volanti *et al.*, 2008). These statements are referring to all the peaks in the micro Raman spectrum however in the case of CuO, these effects toward  $2B_g$  peak are more pronounced. We encountered similar peak position of  $2B_g$  for the CuO nanostructures which were prepared using the ultrasonication and two steps heating methods (**Figures 4.2c and 4.2d**) suggesting that the two methods might produce CuO with similar morphology, as peak position is morphology-related. This result supports our earlier hypothesis that ultrasonication and two steps heating methods may possess the same mechanism for formation of CuO resulted in the same morphology of CuO as they have almost similar peak position of  $2B_g$  peak.

Further analysis of the micro Raman spectrum, we found that CuO prepared by hydrothermal method have the highest intensity at the peak  $2B_g$  followed by reflux, ultrasonication and two steps heating method. The change in intensity of the  $2B_g$  peak could be explained in term of phonon-plasmon coupling due to the high local density of anisotropic carriers in CuO nanostructures (Wang *et al.*, 2010). We believed that the particle size of CuO has affected the intensity of the peak  $2B_g$  where as the size of CuO becomes larger, the intensity of the peak  $2B_g$  will also increase. This statement can be further confirmed using FESEM and TEM images as discuss in section 4.2.2. Moreover, the variation in the  $2B_g$  peak intensity also shows a crystallinity effect of CuO nanostructures. Thus, CuO prepared by hydrothermal method possess the highest crystallinity while CuO fabricated using the two steps heating method possess the lowest crystallinity. This result is in agreement with the XRD results presented in section 4.2.1.

FT-IR is another useful tool to corroborate the XRD result regarding on the nature of the produced CuO. Some of the powder of the final product was mixed with KBr through grinding before pressed it into pellets. This pellet was then subjected to FT-IR analysis. Based on the FT-IR spectrum as shown in **Figure 4.3**, it is shown that there are three strong characteristic peaks at around 443, 521 and 607  $\text{cm}^{-1}$  which corresponding to the Cu-O stretching vibration mode that assigned to the Au, Bu and other Bu mode of monoclinic phase of CuO, respectively (*Erdoğan et al., 2010; Ethiraj et al., 2012; Wang et al., 2009*). This confirmed the presence of nano-sized CuO particles as the final product. The peak at 607  $\text{cm}^{-1}$  may also correspond to the COO bending and rocking in the acetate group. But it is believed that the Cu-O stretching vibration is still the predominant interaction as the formation of CuO is complete at this stage. The FT-IR analyses were summarized in **Table 4.2**.

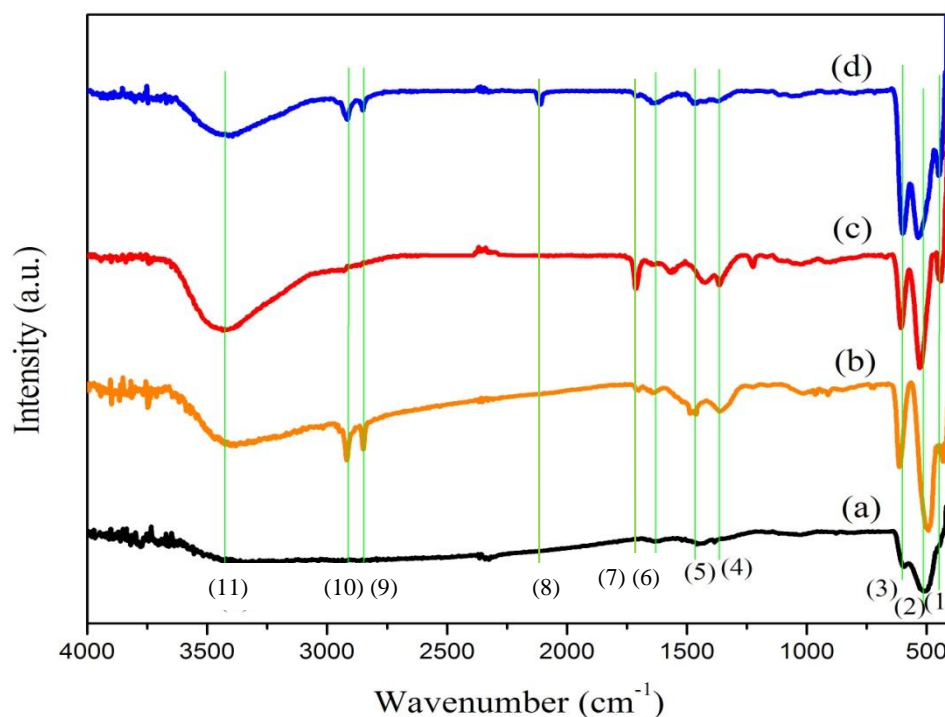


**Figure 4.3:** FT-IR spectra of CuO preparing using (a) reflux, (b) two steps heating, (c) hydrothermal and (d) ultrasonication methods.

**Table 4.2:** Vibrational modes and wavenumbers exhibited by CuO based on our FT-IR result.

<i>Number</i>	<i>Wavenumber (cm<sup>-1</sup>)</i>	<i>Vibrational modes</i>	<i>References</i>
(1)	443	Cu-O stretching	(Wang et al., 2009)
(2)	521	Cu-O stretching	(Erdoğan et al., 2010)
(3)	607	Cu-O stretching	(Ethiraj et al., 2012)
(4)	1388	C=O stretching	(Trass et al., 2011)
(5)	1489	C=O stretching	(Trass et al., 2011)
(6)	1623	O-H bending	(Muhamad et al., 2007)
(7)	1687	C=O stretching	(Muhamad et al., 2007)
(8)	2212	C≡N stretching	(Hou et al., 2012)
(9)	2876	C-H stretching	(Hou et al., 2012)
(10)	2972	C-H stretching	(Hou et al., 2012)
(11)	3450	O-H bending	(Srivastava et al., 2011)

Moreover, there are two weak peaks appear at 1388 and 1489 cm<sup>-1</sup> corresponding to C=O stretching of carboxylate ion bond to the CuO nanoparticles. It has been known that the carboxylate ion may bond to the metal atom through oxygen as a unidentate or bidentate ligand or act as a bridge between two metal atoms (Alexander et al., 2001; Socrates et al., 1994). A coordination of bidentate type is expected between the carboxylate ion and the Cu<sup>2+</sup> of CuO since the two bands due to the C=O stretching vibration are closer together than for the free carboxylate ion (1560 and 1415 cm<sup>-1</sup>) (Li et al., 2004). In addition to the bidentate product, the peak at 1489 cm<sup>-1</sup> also represents the formation of covalent bond between the -OH on the surface of CuO, producing (-C( O)-OCu) (Trass et al., 2011). But it is believed that the bidentate coordination is still the predominant interaction in the formation of CuO. For **Figure 4.3(c)** and **(d)**, there is a peak appear at position 1687 and 2212 cm<sup>-1</sup>, respectively

caused by the weakening of C=O due to resonance and the detection of carbon dioxide in the atmosphere that had not been fully subtracted out.

Besides all the peaks mention above, there is an intense band near 2876 and 2972  $\text{cm}^{-1}$  that can be assigned to the C-H stretching and deformation vibrations of CTAB (Hou *et al.*, 2012). The two weak peaks are exist only on the FT-IR spectrum of CuO prepared by ultrasonication and two steps heating methods and totally disappear in the reflux and hydrothermal method. This result revealed that the CTAB is not completely decomposed to form  $\text{CTA}^+$  and  $\text{Br}^-$  ions under lower temperature, thus it would reduce the number of CTAB molecules that absorbed onto the surface of CuO. Hence, the CuO formed by both ultrasonication and two steps heating methods would favor to form agglomeration of CuO nanostructures. These can be proved by FESEM images presented in section 4.2.2. We also can conclude that the surfactant used in the fabrication of the CuO using both ultrasonication and two steps heating methods have not been totally removed after washing with ethanol and deionized water for several times.

In addition to these strong absorption bands, a weak and a broad absorption bands at 1623 and 3450  $\text{cm}^{-1}$  have also been observed, which are assigned to the stretching and bending mode of absorbed water and surface hydroxyl groups, respectively (Srivastava *et al.*, 2011). Comparing the strength of peak at 3450  $\text{cm}^{-1}$  for all four spectrums, spectra for CuO prepared by hydrothermal method shows strong peak which indicates the highest presence of hydroxyl ions due to the Cu-OH layer (Wang *et al.*, 2009) and higher water content as the hydrothermal method allowed the amount of water before and after reaction remain the same. Moreover, no other infrared

active modes such as  $\text{Cu}_2\text{O}$  which appeared at  $615\text{ cm}^{-1}$  can be traced. Thus, these FT-IR analyses further confirmed the purity of the  $\text{CuO}$  obtained from all four methods.

#### 4.2.2 Morphological characterization: FESEM and TEM analysis

The black colored powders obtained were dissolved in the ethanol via ultrasonication for 5 minutes before drops on the silicon wafer for FESEM characterization and on copper grids for TEM characterization to study the surface morphology of the  $\text{CuO}$  nanostructures. The FESEM images in **Figure 4.4 (a-c)** show the morphologies of  $\text{CuO}$  synthesized by the reflux method that has been taken at different magnifications.

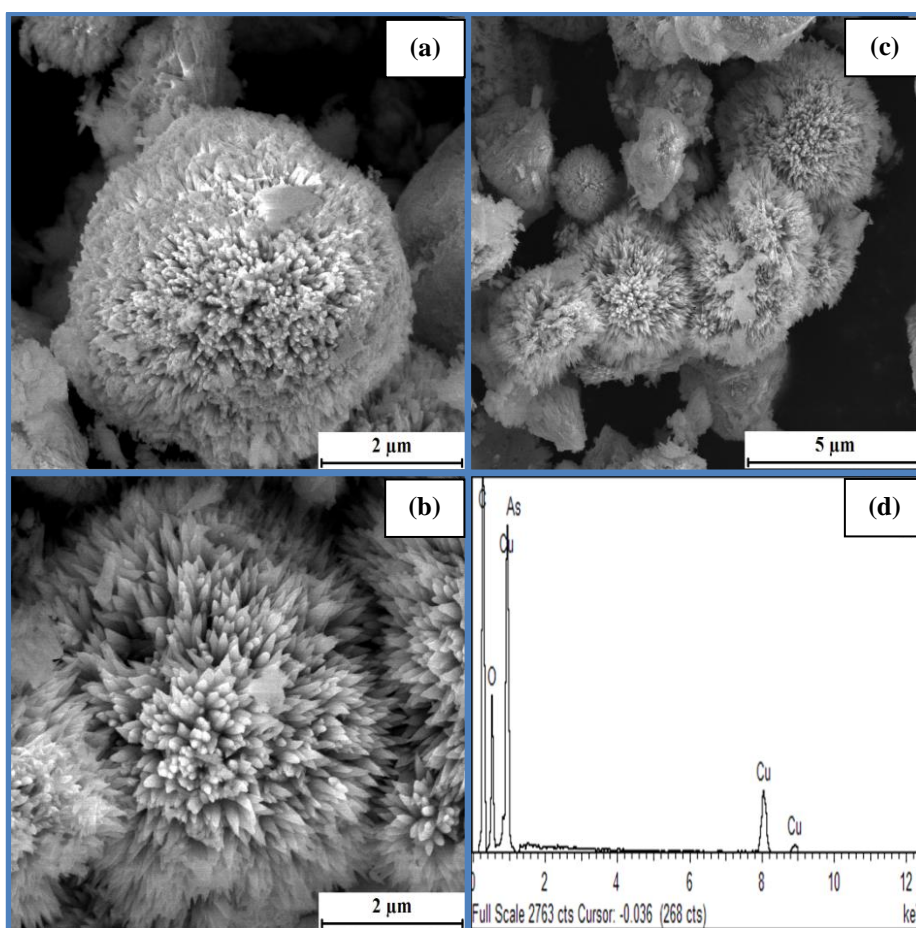


**Figure 4.4:** FESEM images of  $\text{CuO}$  synthesized via reflux method taken at (a) 20K x, (b) 40K x and (c) 80K x magnifications and (d) the EDX result for  $\text{CuO}$  nanoparticles.

CuO produced has flower-like shape with the diameter in the range of 1-2  $\mu\text{m}$ . On a closer look, we can see this flower pattern CuO consists bundle of nanorods as the flower petal. These flower petals seem like radiated from the center of the nanostructures with average diameter less than 100 nm and average width about 50 nm. Furthermore, the chemical composition of the CuO prepared by reflux method are presented in **Figure 4.4d**. The EDX characterization of the CuO reveals the presence of copper (5 %) and oxygen (25 %) in this flower-like structure with the atomic ratio of 1:5, proving the existence of CuO (*Cao et al., 2012*). The absence of other peak further confirms the purity of the final product.

When we changed the preparation method to hydrothermal method, a different morphology of CuO can be observed. **Figures 4.5 (a-c)** show the FESEM images of CuO nanostructures prepared using the hydrothermal method taken at different magnification. This method fabricated CuO nanostructures with rod like pattern and have an average diameter and length of about 5 nm and 100 nm, respectively. These fine nanorods tend to aggregate in bundles because of their high surface energy that render high van der Waals forces (*LB Chen et al., 2009*), which cause the surface interaction. One can also find that the sample is composed of higher capacity of nanorods with almost uniform size and shape, which may correlate with the presence of CTAB that serve as a surfactant that controlled the growth rate and orientation of the crystals (*Yoshida et al., 1999*). The TEM image (**Figure 4.5d**) from part of the sample shows the detail texture of the particles which reveals that the samples is built up from rod-like pattern of CuO with length about 100nm. This result is in good agreement with the result shown by FESEM images.

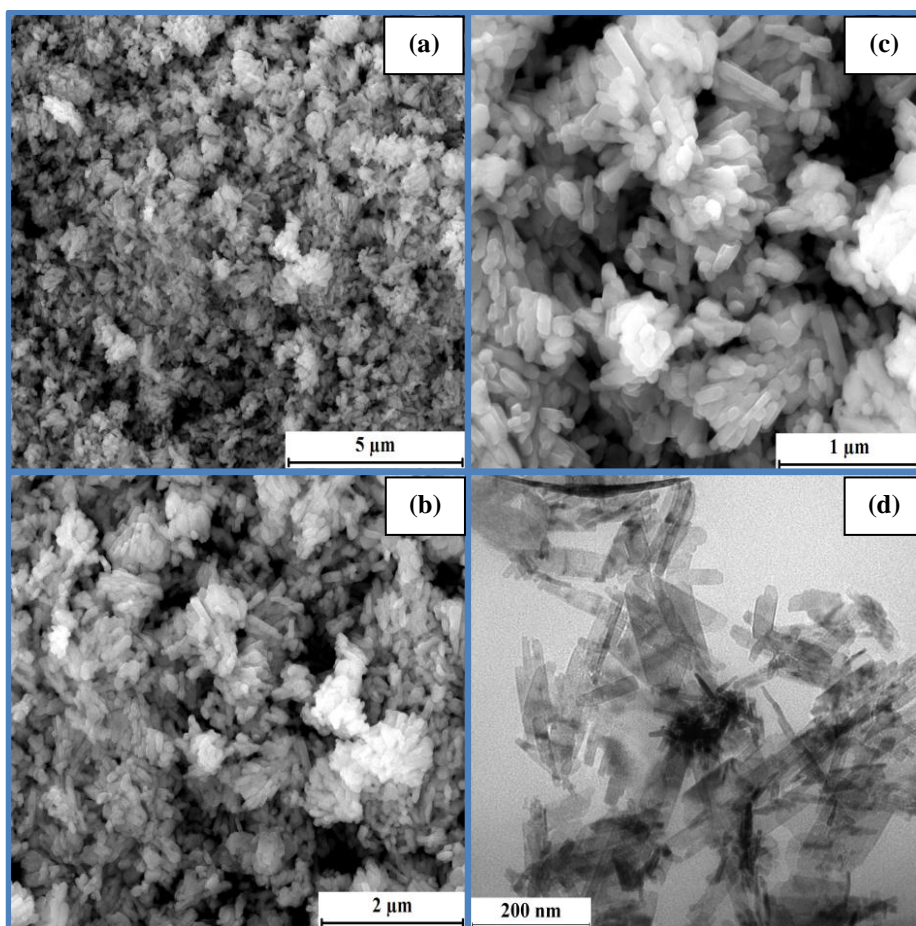


**Figure 4.5:** FESEM images of CuO synthesized via hydrothermal method taken at (a) 20K x, (b) 40K x and (c) 80K x magnifications and corresponding (d) TEM image.

**Figure 4.6 (a-c)** shows the FESEM images of CuO nanostructures obtained from the ultrasonication method taken at different magnification. Crossview of the products indicates that the sample is made up of high yield fibril-like nanostructures with an average length of less than 1 μm and less than 50 nm in diameter. These fibrils tend to assemble into almost spherical bundles with diameters about 5 μm. Further characterization of the morphology of CuO is obtained by TEM as shown in **Figure 4.6d**, which the result is consistent with the FESEM results.

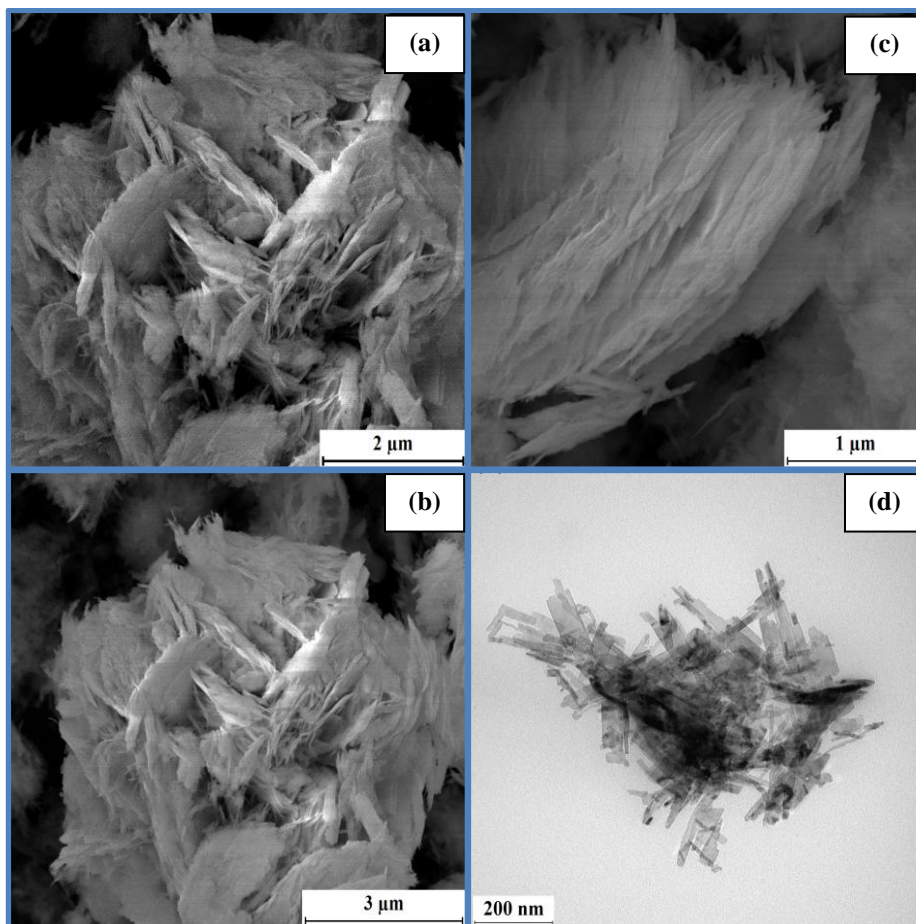


**Figure 4.6:** FESEM images of CuO synthesized via ultrasonication method taken at (a) 20K x, (b) 40K x and (c) 80K x magnifications and corresponding (d) TEM image.

Likewise, the two steps heating method yielded similar fibril-like nanostructures except that it is more narrow and thin than fibrils produced by ultrasonication method, as revealed by FESEM images (**Figure 4.7a-c**). These fibrils possess of an average length and diameter of less than 50 nm and 10 nm, respectively. The TEM image of the sample for one of the microsphere spots is shown in **Figure 4.7b** where we could see a few of microspheres with an average diameter of 0.5 μm that made up of hundreds of compactly self-assembled fibril-like nanostructures. It is clearly seen that the microsphere is consists of fibril-like nanostructures with almost similar sizes as revealed by FESEM results.

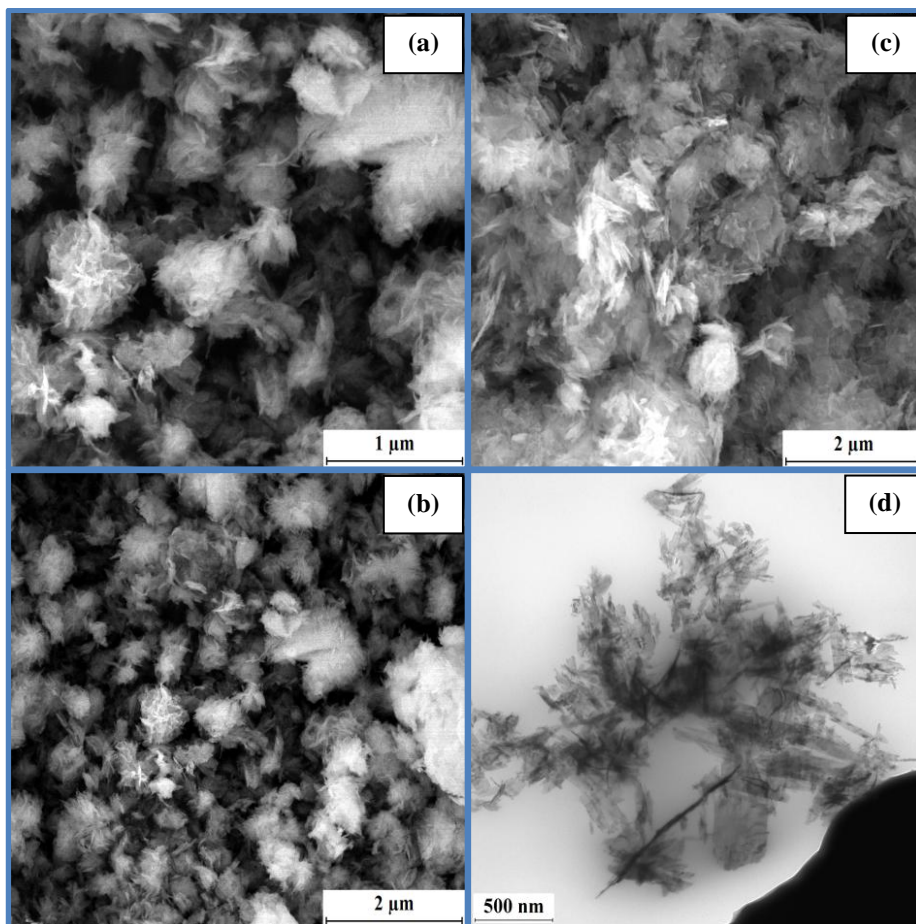


**Figure 4.7:** FESEM images of CuO synthesized via two steps heating method taken at (a) 20K x, (b) 40K x and (c) 80K x magnifications and corresponding (d) TEM image.

Based on all the FESEM and TEM images for CuO fabricated by all four methods, we could see that different method produced different shape of CuO. The ultrasonication and two-step heating methods produced CuO with similar morphology that is fibril-like nanostructures, which then was confirmed one of the hypothesis made by the micro Raman spectrum previously. The hypothesis states that ultrasonication and two steps heating methods should have similar morphology as they possess a similar peak position of  $2B_g$  band. Hence, we can conclude that the synthesis approach plays an essential role in determining the final morphology of the CuO nanostructures. Besides that, the agglomeration of samples prepared by both methods may correlate with the

existence of less surfactant absorbed on the surface of particles as can be evidenced by the FT-IR results shown previously.

Moreover, CuO nanostructures with different particle size were detected based on the FESEM and TEM images that might happen due to the different reaction temperature. In our case, hydrothermal with the highest reaction temperature among the other method produced the longest particle size while the smallest particle size had been synthesized using the two steps heating method. It has been reported before that the smaller particles could get enough energy from the circumstance and escape from each other at a high temperature. Furthermore, the organic ligands on the plane surface and in the solution could exchange more intense with each other. So the particles could change their position with others and choose a suitable plane to attach with another particle to form bigger particles (*Liu et al., 2007*).

### 4.2.3 Formation mechanism of CuO nanostructures

In an attempt to study the effect of different wet chemical processing methods on the formation of CuO, discovering the possible growth mechanism for formation of CuO nanoparticles is a crucial step (**Figure 4.8**). From the research and observation that had been done, it is believed that all four methods went through a similar step of mechanism first, due the same amount and materials used. Afterward, these particles started to show different step of mechanism because each method has a significant influence on directing the formation of CuO nanostructures that affected by the variable processing parameters such as temperature and time.

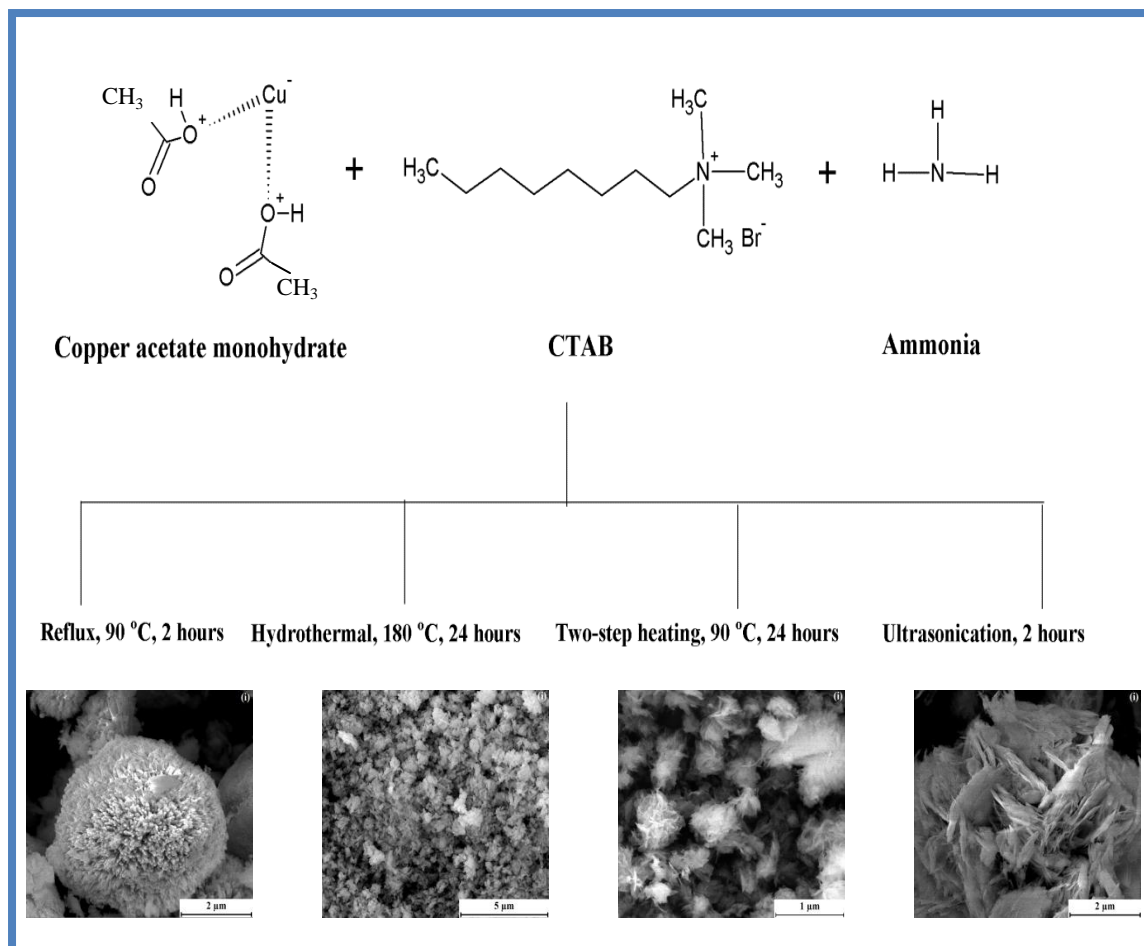
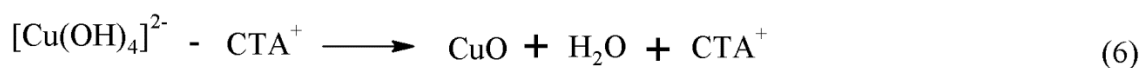
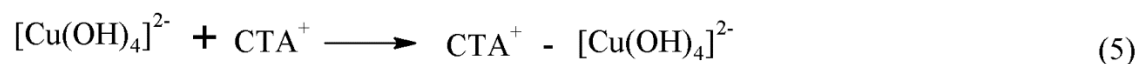
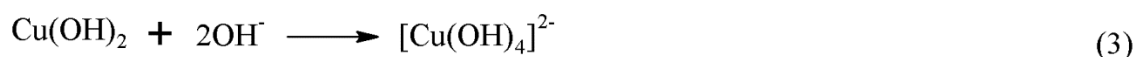
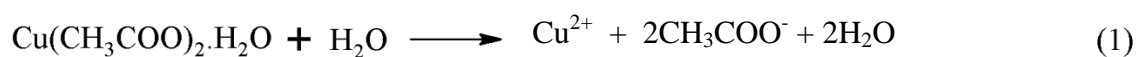


**Figure 4.8:** Formation of CuO nanostructures.

The possible reactions involved in the formation of CuO are shown below:



In general, the process of growing CuO nanoparticles begin with the formation of  $\text{Cu}^{2+}$  aqueous solution straight after copper salt is dissolved in the deionized water (reaction (1)). The process where copper salt dissolved in water further dissociates into its constituent anions and cation is called the hydrolysis process. In this process, water molecules also ionized into hydroxyl anions and hydrogen cations. It has been reported before that  $\text{Cu}^{2+}$  have a coordination number of 6 in aqueous solution which means that it could surround by four water molecules to form a square structure and another two water molecules at its axis due to the solvating action that happen when copper salt was dissolved in water (Veillard, 1977; Zhu et al., 2008). This first reaction would occur in all four methods due to the same type and amount of solvent and also the same precursor for  $\text{Cu}^{2+}$  used that are 25 ml of deionized water and 0.5 g copper acetate monohydrate, respectively.

Upon adding  $\text{NH}_3 \cdot \text{H}_2\text{O}$  in the  $\text{Cu}^{2+}$  aqueous solution, a precipitate was obtained which proven the existence of orthorhombic  $\text{Cu}(\text{OH})_2$  (reaction (2)). The  $\text{NH}_3$  molecules were not going to enter the ion's coordination sphere yet it will act as ligands that bounding on the  $\text{Cu}^{2+}$  cations due to the low concentrations of  $\text{NH}_3$  compared to  $\text{OH}^-$  ions that obtained from the water molecules (Pranowo et al., 2001). Hence,  $\text{Cu}^{2+}$  tended to make a ligand exchange reaction strongly with  $\text{OH}^-$  which form the  $\text{Cu}(\text{OH})_2$ . No precipitate of  $\text{Cu}(\text{OH})_2$  could be observed if the ammonia concentration was too high due to the higher numbers of excess  $\text{NH}_4^+$  and  $\text{NH}_3$  that reacted with  $\text{Cu}(\text{OH})_2$ , thus make it dissolved immediately (Xiang et al., 2010a). In addition, the concentration of ammonia and  $\text{OH}^-$  is correlated with the pH values of the mixture we made at this stage.

As the solution has a pH value of 10, it formed a basic solution. The  $[\text{Cu}(\text{OH})_4]^{2-}$  complex was formed in the basic solution as a result of the  $\text{Cu}(\text{OH})_2$  precursor that hardly dissolved (reaction (3)). These negatively charged complexes were the first nucleation seed or growth units for the formation of CuO that would act as an initial nucleus along the particle growth. Meanwhile, the positively charged tetrahedron which possesses a long hydrophobic tail known as  $\text{CTA}^+$  was formed when CTAB was ionized completely in water as CTAB is an ionic compound (reaction (4)). CTAB is a useful surfactant that serves as a morphology directing agent to control the morphology of nanomaterials as well as promote self-assembly of nanoparticles.

According to the reaction (5), ion pairs of  $[\text{Cu}(\text{OH})_4]^{2-} - \text{CTA}^+$  were formed by electrostatic reaction between  $[\text{Cu}(\text{OH})_4]^{2-}$  anions with  $\text{CTA}^+$  cations. Thus,  $\text{CTA}^+$  ions absorbed on the surface of  $[\text{Cu}(\text{OH})_4]^{2-}$  (Wang *et al.*, 2010). The crystal growth process that involved the interactions between surfactant adsorbed on the surfaces of the nanoparticles is called the oriented attachment mechanism (Zhang *et al.*, 2008). These combination ions would form CuO nanostructures via a dehydration process where unstable copper complex started to convert to CuO with different morphologies that directed by the presence of CTAB (reaction (6)). Cao *et al.* speculate that due to electrostatic interactions, inorganic precursor  $[\text{Cu}(\text{OH})_4]^{2-}$  and cationic surfactant CTAB could form different conformations in organic surfactant composites under different reaction conditions, which may serve as templates (Cao *et al.*, 2003). Basically, there are a few points that need to be highlighted regarding the factors that affect the growth behaviors of CuO as shown in **Figure 4.9**.

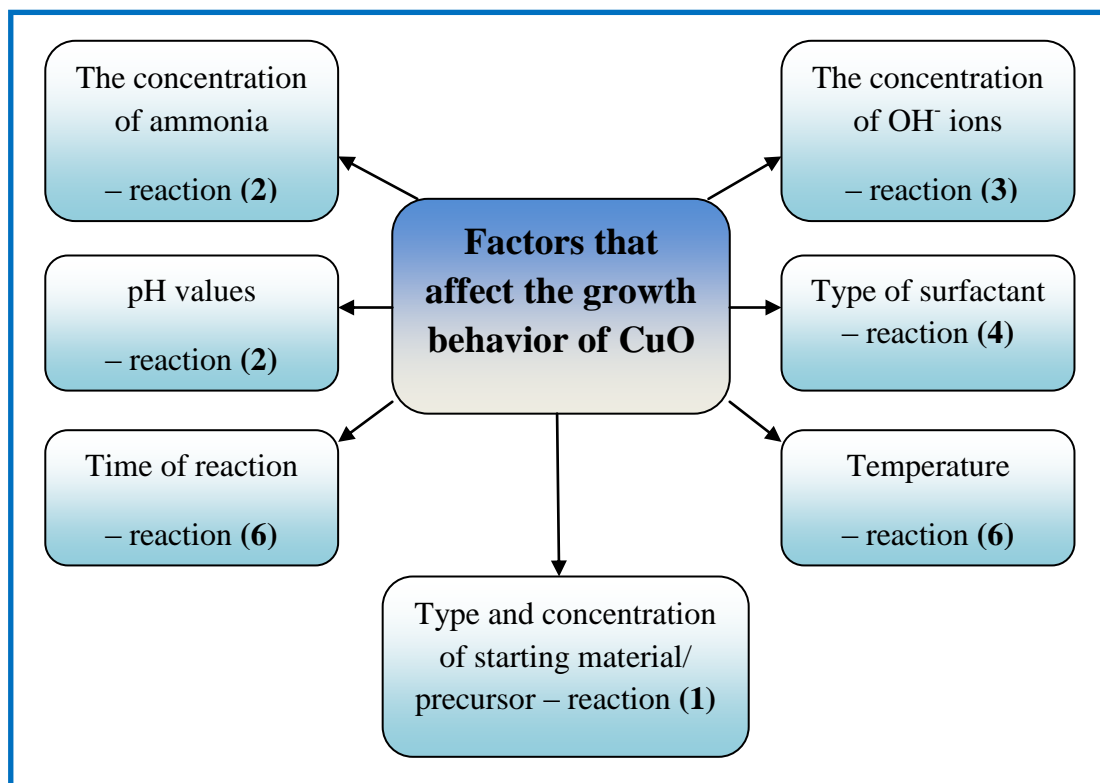
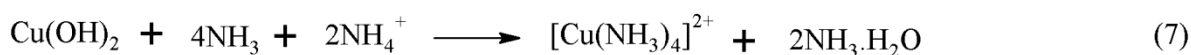


**Figure 4.9:** List of factors that affect the growth behavior of CuO.

We suggest that all four methods went through the same reaction from reaction (1) to reaction (2) as they used the same type of copper precursor (copper acetate monohydrate) where the mineralize would be the  $\text{CH}_3\text{COOH}$ . The study done by Cho *et al.* (Cho *et al.*, 2009) and Xu *et al.* (Xu *et al.*, 2009) prove that the different mineralizes have a significant influence on the formation of different shapes of crystallites as they form an interfering ions in the solution that will interfere the crystal growing. Hence, we hypothesize that all four methods would have the same crystal growing rates because of the presence of  $\text{CH}_3\text{COOH}$  or  $\text{CH}_3\text{COO}^-$  ions that can kinetically control it. With the same amount of copper salt and water, we expected that the concentration of  $\text{Cu}^{2+}$  will be the same.

Moreover, we also used the same amount of  $\text{NH}_3\cdot\text{H}_2\text{O}$  in all methods so the concentration of ammonia in the solution should be the same and we also believed that the water molecules were more dominant than ammonia. Hence, there was no existence of excess  $\text{NH}_4^+$  and free  $\text{NH}_3$  in the solution that can further react with  $\text{Cu}(\text{OH})_2$  as shown in reaction (7) and the  $\text{Cu}^{2+}$  is favorable to form  $\text{Cu}(\text{OH})_2$  instead of  $[\text{Cu}(\text{NH}_3)_4]^{2+}$  complexes. Since the pH values are fixed in all methods (at pH 10), the concentration of  $\text{OH}^-$  expected to be the same, thus produced the same concentration of  $[\text{Cu}(\text{OH})_4]^{2-}$  complex at first as it has been reported before that the different pH values has no doubt lead to the different concentration of  $\text{OH}^-$  in the solution (*Xiang et al., 2010a*).



However, according to the result of the analysis, only reflux and hydrothermal method could form the  $[\text{Cu}(\text{OH})_4]^{2-}$  complex while the other two methods could only form  $\text{Cu}(\text{OH})_2$ . This is because we believed that while the solutions go through reflux and hydrothermal process, the amount of  $\text{OH}^-$  would increase as the concentration of water molecules is higher even though we heated the solution at 90 °C and 180 °C, respectively if compared to the other two methods. It is because reflux is a technique involving the condensation of vapors and the return of this condensate to the system from which it originated while hydrothermal process involved a close system reaction that allowed the concentration of  $\text{OH}^-$  remains the same. Hence, reflux and hydrothermal method would have excess  $\text{OH}^-$  ions that allowed the formation of  $[\text{Cu}(\text{OH})_4]^{2-}$  complex.

In the case of reflux method,  $[\text{Cu}(\text{OH})_4]^{2-}$  ions might exist in spherical clusters at low temperature (90 °C) due to the steric effect and hydrophilicity of hydroxyl that allowed each atom within a molecule occupies a certain amount of space, hence brought too close together to form a spherical cluster (Cölfen *et al.*, 2003). These spherical clusters of  $[\text{Cu}(\text{OH})_4]^{2-}$  were then become the first nucleation seeds for the growth of flower-like CuO nanostructures. After 2 hours of heat treatment, the flower-like CuO nanostructures were obtained because  $[\text{Cu}(\text{OH})_4]^{2-}$  clusters started to dehydrated to form CuO flower-like while  $\text{CTA}^+$  that adsorbed on the surfaces of these seeds will help to direct the growth of flower petals all over its surfaces.

In the suggested mechanism for the formation of rod-like CuO nanostructures by hydrothermal process, the concentration of  $[\text{Cu}(\text{OH})_4]^{2-}$  anions were higher due to the higher processing temperature (180 °C) that gradually generate the  $\text{OH}^-$  ions. As a result, it induces the highest reaction rate for producing  $[\text{Cu}(\text{OH})_4]^{2-}$  ions. The required number of charge compensating cations remarkably increases as the concentration of  $[\text{Cu}(\text{OH})_4]^{2-}$  increases to a higher value. So, the system favors a complete lamellar phase structure to obtain its minimum energy configuration in which the interlayers might serve as microreactors and responsible for the ultimate formation of nanorods (Cao *et al.*, 2003). Under hydrothermal condition, rod-like CuO nanostructures was produced via the decomposition of ion pairs of  $[\text{Cu}(\text{OH})_4]^{2-} - \text{CTA}^+$ .

Meanwhile, the formation of fibril-like CuO nanostructures under two steps heating conditions would start with the production of  $\text{Cu}(\text{OH})_2$ . Before that, the polar hydrophilic head of CTAB chain would attach itself to the  $\text{Cu}^{2+}$  ion and relocated it according to the surfactant-water interaction. As the micelles formed, the ions attached acted as the nucleation spots for nanofibril growth in a radial direction from the centers

of the micelles. Surfactant could encapsulate a water drop and with its copper ions which formed a nanoparticle. Afterward, the  $\text{OH}^-$  ions that penetrated the surfactant shell would reduce the particle to form  $\text{Cu}(\text{OH})_2$  (**Figure 4.10**). When the surfactant density is large enough it forms a larger shell, the volume of surrounded water is larger and the shape of the structure is more elongated (*Filipič et al., 2012*). The  $\text{Cu}(\text{OH})_2$  is believed to have the needle-like structures that tends to assemble into bundles due to the Van der Waals force and hydrogen bonds (*Lu et al., 2004*). Under the heavy heating of  $\text{Cu}(\text{OH})_2$ , the fibril-like  $\text{CuO}$  nanostructures were yield as the final product due to the thermally induced decomposition.

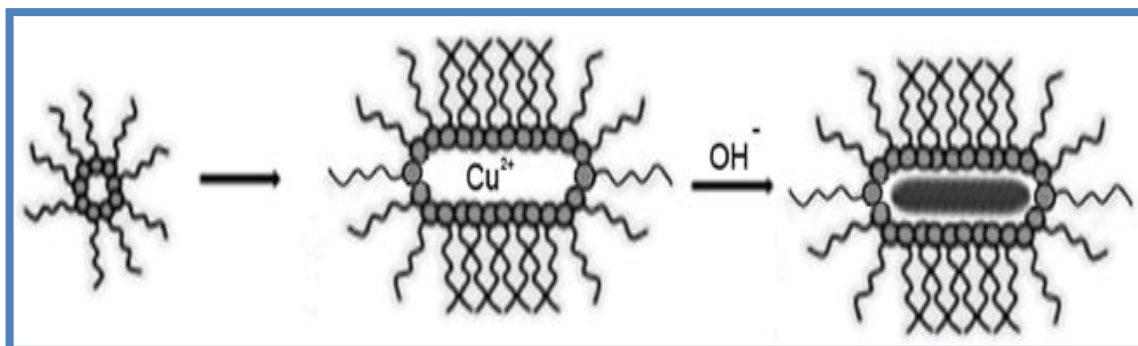


**Figure 4.10:** Growth of a  $\text{Cu}(\text{OH})_2$  with the help of CTAB as the surfactant which further reduced to form fibril-like  $\text{CuO}$  nanostructures (*Filipič et al., 2012*).

The same mechanism speculates goes into the formation of fibril-like  $\text{CuO}$  nanostructures using ultrasonication method even though the ultrasonication method did not involve the heating treatment. We suggest that during the reaction at the first stage, grinding can increase the velocity of the molecules and increase the contact area of the reagent molecules. In addition grinding can increase the energy of the reaction and increase the temperature of some areas, which makes one reaction begins. This is perhaps the most important reason for the beginning of a solid state reaction (*Jisen et al., 2004*).

Upon treated under ultrasonication, the individual  $\text{Cu}(\text{OH})_2$  nanoparticles was formed at the beginning where then  $\text{Cu}(\text{OH})_2$  nanowires grew preferentially by the oriented attachment of the primary nanoparticles with the help of surfactant cations  $\text{CTA}^+$  that was attached to its surfaces, which was coupled with coordination self-assembly, resulting in polycrystalline  $\text{Cu}(\text{OH})_2$  nanowires. The individual nanowires were further attached side by side to assemble into bundles on further aging, accompanying an Ostwald ripening process leading to larger crystallite sizes and tougher nanowires (Lu et al., 2004). The reaction continued to increase resulted in transformation of  $\text{Cu}(\text{OH})_2$  to fibril-like  $\text{CuO}$  nanostructures through breaking the interplanar hydrogen bonds and recrystallization.

We believed that the ultrasonication method is based on acoustic cavitations through the formation, growth, and collapse of bubbles in the liquid (Xiao et al., 2011). The chemical effects of ultrasound have been well explained as the consequence of localized hot spots created during bubble collapse. Bubble collapse in liquids results in an enormous concentration of energy from the conversion of the kinetic energy of liquid motion into heating of the contents of the bubble. The high local temperatures and pressures, combined with extraordinarily rapid cooling, provide a unique means for driving chemical reactions under extreme conditions (Suslick et al., 1999).

Furthermore, cavitation and the shock waves produced during ultrasonic irradiation of liquid-powder slurries could accelerate solid particles to high velocities. The interparticle collisions that resulted were capable of inducing striking changes in surface morphology, composition and reactivity. Thus, microjet and the shockwave impact (on large surfaces) and interparticle collisions (with powders) have substantial effects on the chemical composition and physical morphology of solids that can

dramatically enhance chemical reactivity (*Suslick et al., 1999*). However, the exact growth mechanisms of CuO nanostructures under different wet methods are still under investigation.

#### 4.2.4 Catalytic activity of CuO nanostructures

CuO has attracted a considerable interest of researchers due to its unique properties which can be applied in various fields of application. Currently, many reported the use of H<sub>2</sub>O<sub>2</sub> for the purpose of the oxidative degradation of organic dye. However, MB dye is resistant to H<sub>2</sub>O<sub>2</sub> oxidizer due to its high stability characteristic. Thus, in order to overcome this problem, the combination of H<sub>2</sub>O<sub>2</sub> and metal oxide catalysts with the ability to form reduction and oxidation pairs has been used to degrade the organic compounds (*Weixin Zhang et al., 2007*).

In the current work, MB, a common cationic dye in textile industry, was chosen as a typical organic pollutant. The catalytic properties of CuO were investigated by the catalytic oxidation of MB in the presence of H<sub>2</sub>O<sub>2</sub> at ambient temperature. For the interval of 1 hour, 1 ml aliquot was pipetted into a quartz cell and its absorption spectrum was measured using a UV–vis spectrometer. The graph of absorbance versus wavelength was plotted based on the result for 10 hours reaction, as shown in **Figure 4.11**. It is clear that the addition of nanostructures of CuO to the MB and H<sub>2</sub>O<sub>2</sub> solution results in the decreased of the absorption peaks of MB at 665 nm with respect to the increased of the reaction time. The peak at 665 nm become broad and weak as a function of time but the rate of degradation of MB is different between all methods. The results show that rod-like and fibril-like CuO prepared by hydrothermal and

ultrasonication methods, respectively, presents the fastest rate of degradation of MB (Figures 4.11 b&c).

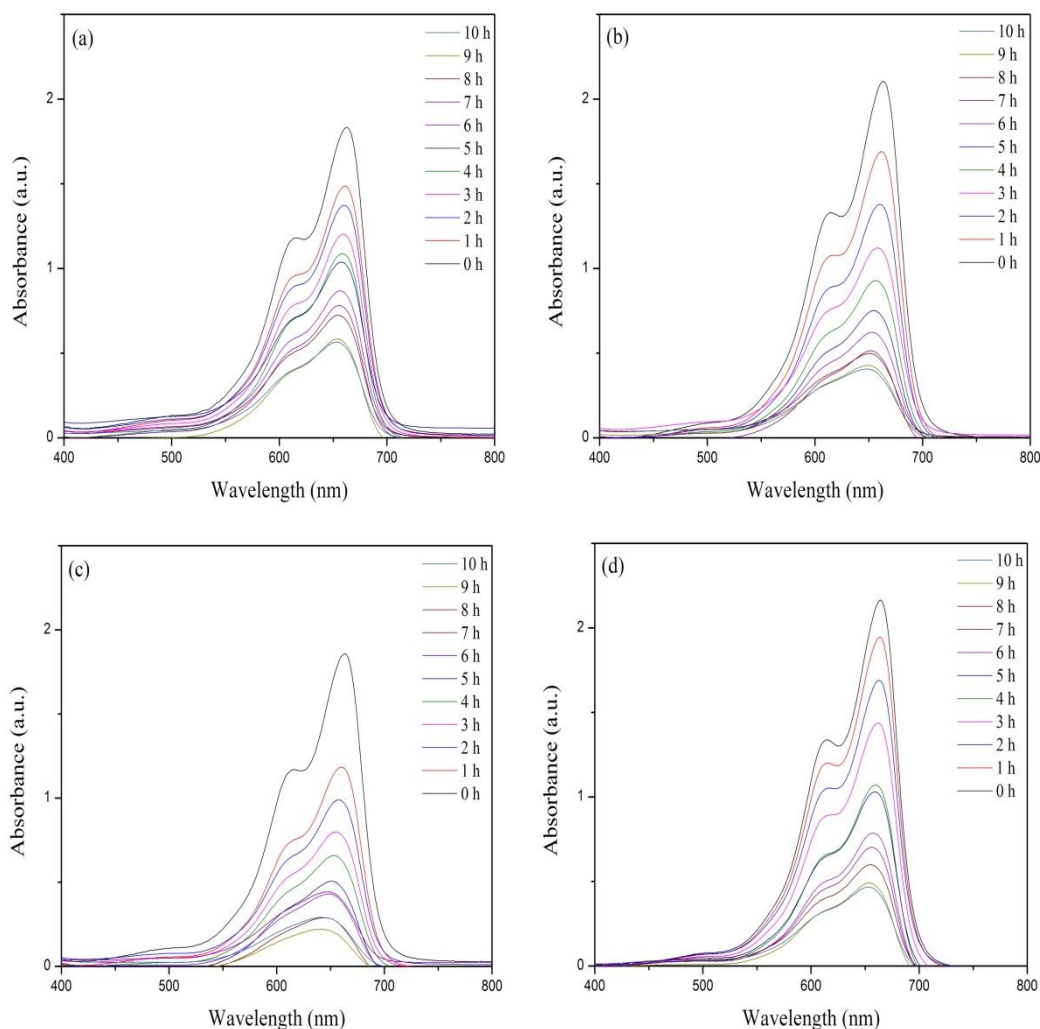


**Figure 4.11:** UV-vis absorption spectra of an aqueous solution of MB and  $\text{H}_2\text{O}_2$  in the presence of CuO nanostructures synthesized using (a) reflux, (b) hydrothermal, (c) ultrasonication and (d) two steps heating methods at different reaction times.

The UV profiles on degradation of methylene blue are translated into a single plot of degradation (%) versus reaction time for comparison (Figure 4.12). In the absence of CuO catalyst, the degradation of MB was insignificant even though after 10 hours of reaction time. Only 5.12 % of degradation was achieved in the blank

experiment in the absence of a catalyst. In contrast, the catalytic performance with the inclusion of CuO nanostructures has an impressive increase of at least 14 times. The initial contaminants almost fully diminished after 10 hours of reaction with the catalyst. The catalytic activity ascends in the following order: reflux (flower-like CuO reached 71.8 %) < two steps heating (fibril-like CuO reached 81.4 %) < ultrasonication (fibril-like CuO reached 87.1 %) < hydrothermal (rod-like CuO reached 87.5 %).

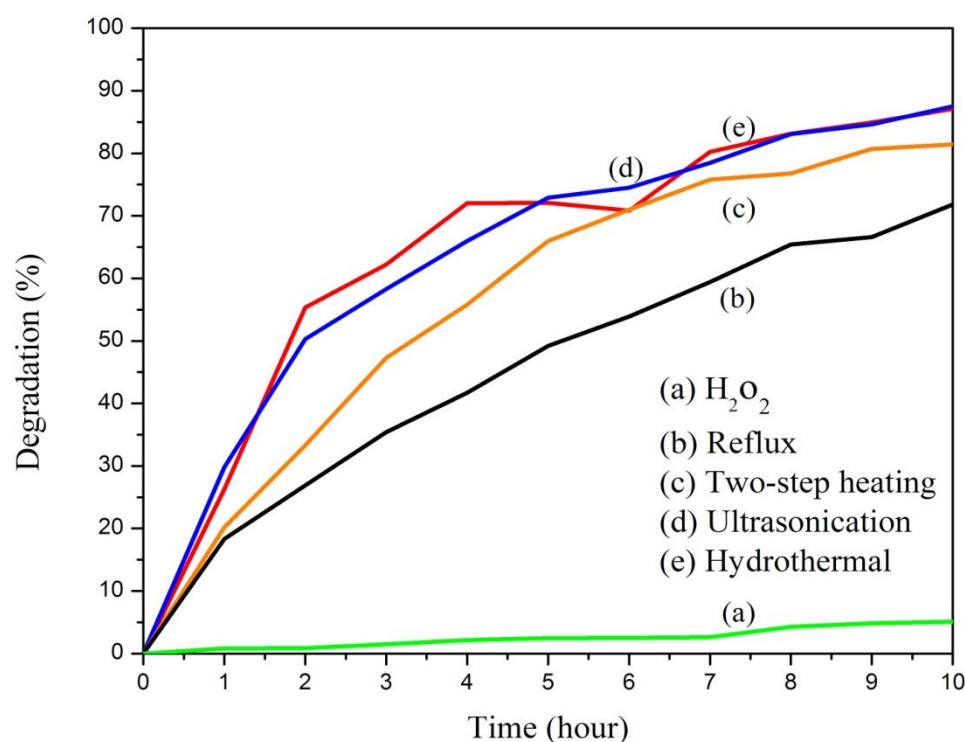


**Figure 4.12:** Time profile of MB degradation.

The ultrasonication and hydrothermal methods produced CuO nanostructures with the highest crystallinity, resulting in the best catalytic performance. On the other hand, the reflux and two steps heating methods yielded CuO nanostructures with lowest crystallinity, hence the lowest catalytic performance. Thus, the catalytic activity of CuO was influenced by the crystallinity of the nanostructures. Our results coincided with the findings of Teng *et al.* where their research has proven that the crystallinity of the

catalyst played the dominating role in the enhancement of catalytic activities (*Teng et al., 2008*).

Eventhough the particle size of rod-like CuO is quite big, but it is still in the nano-sized which means that the surfaces of nanoparticles are unstable and can reconstruct dynamically, especially during catalysis process, where the constantly changing adsorbate-surface interactions can further induce dynamic surface restructuring thus enhanced the catalytic performance (*Zhou et al., 2009*). We believed that this maybe the reason why rod-like CuO exhibits the best catalytic performance even though it has a bigger particle size. Moreover, the enhanced catalytic activity of the CuO may be associated with the uniform and organized structure as can be evidenced by the research done by L. Xu *et al.* (*Xu et al., 2009*). In our case, hydrothermal method has been confirmed to produce the most uniform and organized structure with high capacity of particles that ensure more active surface site as compared to the others CuO nanostructures. So, it is not surprising that this rod-like CuO could exhibit excellent catalytic properties.

The possible mechanism for ambient degradation of methylene blue by CuO with the presence of H<sub>2</sub>O<sub>2</sub> is shown in **Figure 4.13**. It is generally accepted that the main process in the degradation of MB is related to the adsorption–oxidation–desorption mechanism that happen on the surface of the catalyst (*Zhang et al., 2006*). At the first stage, CuO nanostructures would absorb MB onto its surfaces followed by absorption of H<sub>2</sub>O<sub>2</sub>. Next, the highly active catalyst, CuO nanostructures induce the decomposition of H<sub>2</sub>O<sub>2</sub> to form free radical species, such as HO•, HOO• or O<sup>2-</sup>•. The nascent free radical species have the high oxidative ability especially the HO• that act as the leading oxidation agent. These species would cause destructive oxidation of the

organic dye. Finally, the small molecules from the dye degradation were desorbed of the CuO surface, and the catalyst is recovered immediately after it left the CuO nanostructures surfaces (Zaman *et al.*, 2012).

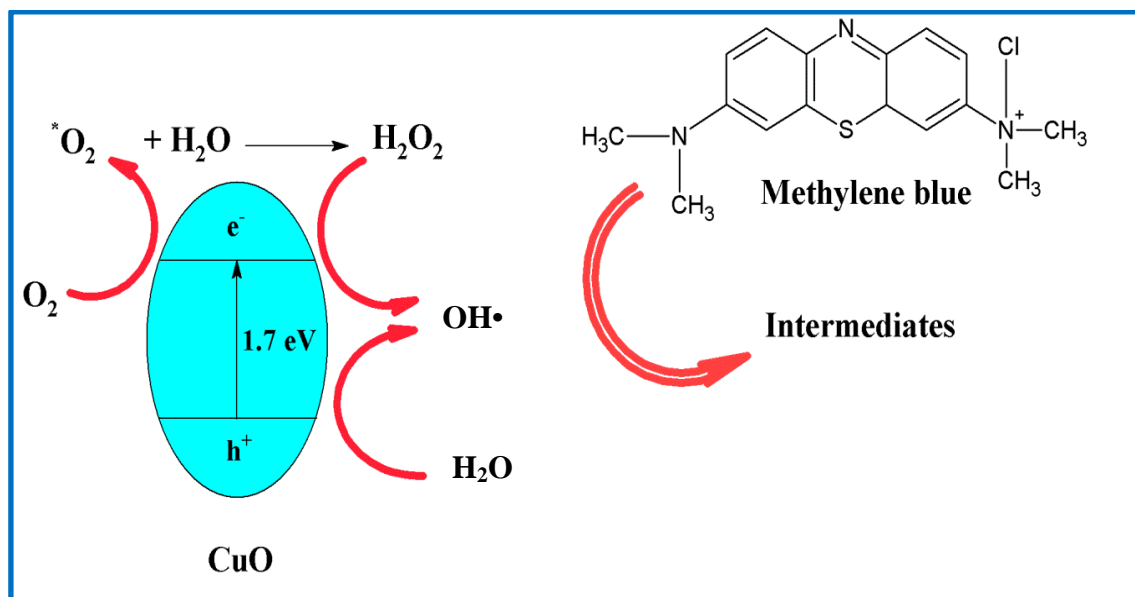


**Figure 4.13:** Ambient degradation of MB by CuO with the presence of H<sub>2</sub>O<sub>2</sub>.

### 4.3 Results for synthesis of GO, FGO and FG

In the second part of this chapter, the results for synthesis of GO, FGO and FG that obtained from several characterization tools will be discuss, which includes XRD, micro Raman, FT-IR, TGA, FESEM, TEM, and UV-vis spectrometer. The deeper discussion regarding the result obtained are presented including the investigation toward the possible formation mechanism of GO, FGO and FG. Through characterization methods and understanding of its chemical structure, the difference between all three types of materials could be detected and further understand of this behavior toward different properties.

### 4.3.1 Structural characterization: XRD, micro Raman, FT-IR and TGA analysis

One of the important parameter to evaluate the structural information of GO, FGO and FG is by measuring the distance between these two layers which can be obtained from XRD. Thus, the structural characterization of the samples was first carried out by powder XRD performed at room temperature with the angle of  $2\theta$  were recorded from  $5^\circ$  to  $80^\circ$ . The d-spacing of all three samples were calculated using the Bragg's Law before being analyzed to study the possible structure started from GO until it transform to FG.

The XRD pattern of the prepared GO and FGO is compared with those of FG obtained by hydrothermal reduction of FGO in **Figure 4.14**. The characteristic peak of GO appears at  $\sim 10^\circ$  is corresponding to (001) plane with an interlayer d-spacing of 8.36 Å which is higher than that of graphite ( $\sim 3.40$  Å). The presence of oxygen-rich groups (carboxylic acid, carbonyl, hydroxyl and epoxy groups) on both sides of the GO sheets and trapping of water molecules between the sheets after the oxidation and exfoliation process could possibly contribute to the increasing of the interlayer spacing of GO (*Zhang et al., 2009*). It's been reported before that the insertion of these groups induced by the oxidation process leads to decrease in the van der Waals forces between the graphene sheets in the exfoliated GO (*Karthika et al., 2012*). In this regard, the graphitic structure of GO was found to be disordered slightly due to the alteration of functional groups. Moreover, the interlayer spacing of GO is proportional to the degree of oxidation (*Chen et al., 2011; Marcano et al., 2010*) hence, the increase in d-spacing proved the oxidation of graphite flakes had occurred to form GO.

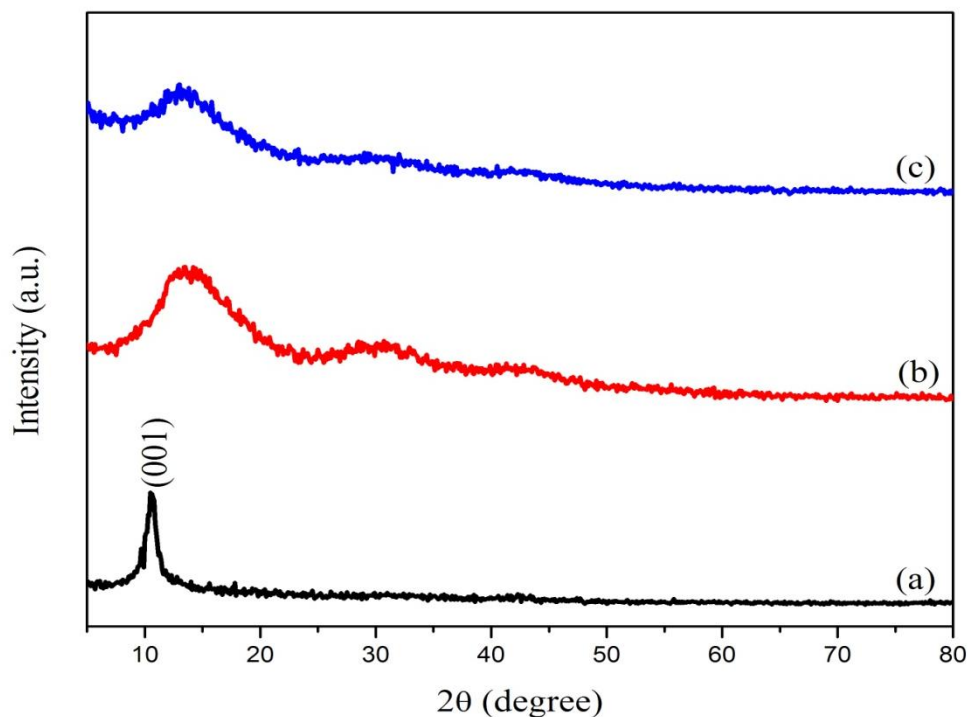


**Figure 4.14:** XRD patterns for (a) GO, (b) FGO and (c) FG.

Apparently, the characteristic peak of GO is almost diminish in FGO demonstrating the exfoliation of regular stacks of GO which was caused by the existence of negatively-charged functional carboxyl groups on both sides of an FGO sheet after the silanization process. These chemicals grafting of silane molecules onto GO gives rise to the drastic decrease of d-spacing from  $8.36 \text{ \AA}$  to  $6.80 \text{ \AA}$  hence confirmed the conversion of GO into FGO. There is an emergence of a new hump located at  $\sim 13^\circ$  which indicates the formation of a new lattice structure, suggesting that the GO had been partially reduced to graphene after the functionalization process. Using the idea of the presence of oxygen groups supposed to make the layer spacing enlarge other than the oxidation process that involved the formation of GO, the addition of more functional groups on GO surfaces would help to loosen the graphitic layers for easy exfoliation of GO to form partially reduced FGO during the functionalization process.

The XRD pattern for FG is almost similar to FGO, except that its peak is broad, weak and a little bit shifted to the higher angle. The weak diffraction peak indicates the typical amorphous structure of FG. The broadening may result from the poor order of the FG sheets along the stacking direction hence revealing the existence of many free nanosheets in the sample. Whilst, the decrease in its intensity indicates that graphene had been fully exfoliated into single-layered or few-layered sheets (Cai *et al.*, 2007), as further hydrothermal treatment increased exfoliation (Zhou *et al.*, 2009). In contrast to FGO, the interlayer spacing of FG is decreased to 6.10 Å. This reduces in d-spacing might be due to the removal of the oxygen-containing groups of FGO which decomposed into CO<sub>2</sub> and H<sub>2</sub>O by high temperature heat treatment (in our work is 180 °C) under hydrothermal condition (Du *et al.*, 2010). Note that this decrease in d-spacing also confirms the almost recovery of graphitic crystal structure after the reduction of FGO via hydrothermal treatment. The d-spacing posses by GO, FG and FG is summarized in **Table 4.3**.

**Table 4.3:** Properties of GO, FGO and FG obtained by XRD analysis.

<i>Material</i>	<i>Peak Position, 2<math>\theta</math></i> (°)	<i>d-spacing</i> (Å)	<i>FWHM</i> (rad)
<i>GO</i>	10.58	8.36	0.0193
<i>FGO</i>	13.01	6.80	0.0284
<i>FG</i>	14.50	6.10	0.0333

Micro Raman spectroscopy is one of the most efficient tools to characterize material based on carbon, especially considering the fact that the micro Raman intensities would be higher induced by the conjugated and double carbon-carbon bonds thus provides the best signature of characterizing graphene. By analyzing the micro Raman spectrum, it would give a great deal of detail on the fine structure of GO, FGO and FG as it is sensitive to the number of layers and also to dopant effects. Generally,

two most characteristic features of graphene could be detected from its micro Raman spectrum namely the D and G band. It is reported that the D peak corresponds to the defects and disorder-activated Raman mode arise from the vibrations of  $sp^3$  carbon atoms while G peak arise from  $sp^2$  hybridized carbon atoms in a graphitic 2D hexagonal lattice (Ferrari *et al.*, 2006). The micro Raman spectra of GO, FGO and FG have been recorded in **Figure 4.15** is carried out with incident laser of 514 nm in wavelength.

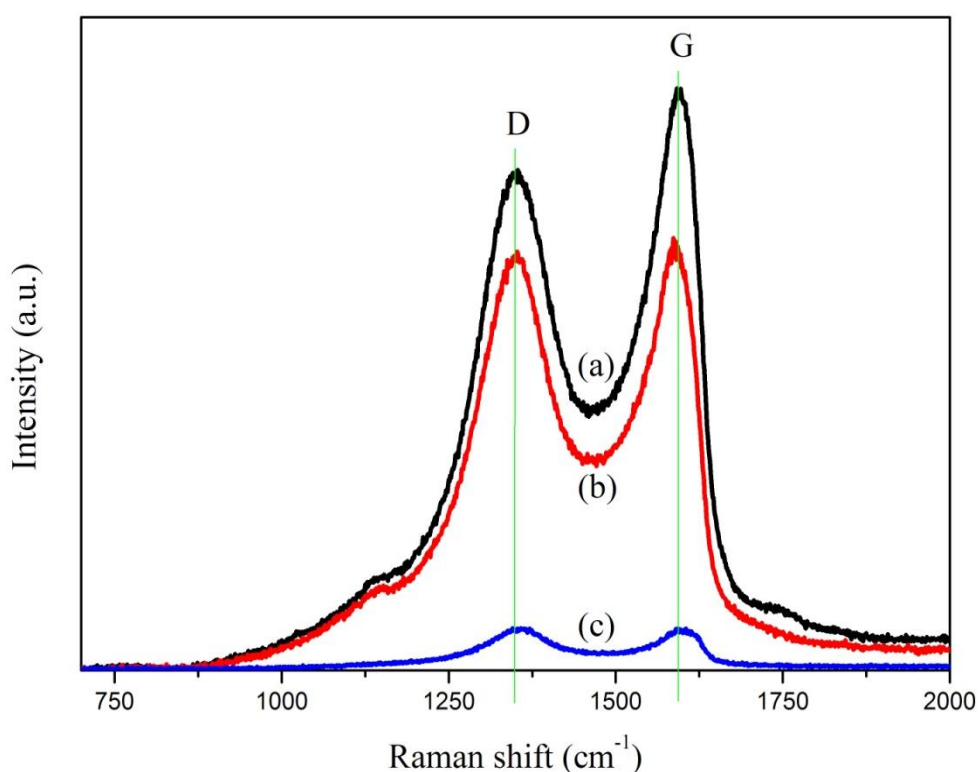


**Figure 4.15:** Micro Raman spectrum for (a) GO, (b) FGO and (c) FG.

As shown in micro Raman spectra, all samples display two prominent peaks that assigned to the D and G peak. For GO, the G band is located at  $1593\text{ cm}^{-1}$  while the G band for FGO can be observed at position  $1591\text{ cm}^{-1}$  and decreased to  $1586\text{ cm}^{-1}$  for FG. We could see there is a red-shifted trend occurred in G band position after functionalization and reduction process. The spectrum also clearly visualized the

broadening of the G band from GO to FG. This shifting and broadening may relate to the increase in temperature along the process of functionalization of GO (65 °C) and hydrothermal reduction (180 °C) of FGO that induced the transformation of  $sp^3$  amorphous GO to  $sp^2$  nanocrystalline graphene. Cuong *et al.* reported an amorphous and highly disordered  $sp^3$  matrix had separating the small clusters of  $sp^2$  in GO by forming a high tunnel barrier between clusters, therefore, thermal energy triggered by heat supplied through the whole process of functionalization and reduction will facilitates clustering of  $sp^2$  phase forming a connection between ordered rings and phase transition from amorphous to the 2D grapheme (Cuong *et al.*, 2010). Moreover, the shift of G band also indicates the functionalization of GO had occurred and further shifting demonstrates the recovery of the  $sp^2$  domain after the hydrothermal reduction of FGO (Wang *et al.*, 2009).

Significant intensity changes in the D band during the functionalization and reduction process are also reflected in the micro Raman spectrum. We could observe that GO have the highest intensity of D band followed by FGO and FG. It is noted that the intensity of D band correlates with the degree of defects and impurities in the graphitic structures and hence the increase in its intensity shows higher defect in the graphitic network especially at the edge of the sheets. Therefore, the functionalization and reduction process had reduced the defect as the intensity of D band is decreased. However, the defect is not fully removed as the D band is still appearing and prominent in all three micro Raman spectrums. This result could be linked to the d-spacing obtained from the XRD analysis. The d-spacing for GO is higher compared to FGO and FG due to the presence of many defects and nanoholes. Thus this result is visualized in the highest intensity of D band in micro Raman spectrum. By considering the existence of oxide groups and  $H_2O$  molecules in the empty spaces in GO, some of it will be

removed after functionalization and reduction process, hence reduce its d-spacing is reflected in the lower intensity of D band for FGO and FG. Therefore, FGO and FG can have oxide groups of C-O<sub>x</sub> with a sp<sup>3</sup> bond in their defects and nanoholes (*Huh, 2011*) thus proving the prominent of D band for FGO and FG.

The measure of the degree of oxidation and reduction as well as the disorder present within graphene can be obtained by calculating the intensity ratio of D band to G band ( $I_D/I_G$ ). The  $I_D/I_G$  ratio for GO is 0.87 which markedly increased to 0.97 for FGO upon functionalization process. The increment indicates the formation of much sp<sup>3</sup> carbon on the graphene plane, reflecting the increase in disorder after functionalization (*Huang et al., 2012; Kudin et al., 2008*). These results give the evidence of the successful modification of GO surfaces by silanization process to form FGO. Moreover, the result also suggests that functionalization process is able to produce a limited amount of damage which causes the relative disorder (*Chen et al., 2011*). The  $I_D/I_G$  ratio is further increased to 1.01 after hydrothermal treatment. This change should be possible attributed to a more numerous in number of a decrease in the average size of the sp<sup>2</sup> carbons upon reduction, compared with GO and FGO (*Chen et al., 2011*) which cause the increased defects or edge areas.

One of the ways of checking chemical properties of the sample is via FT-IR spectroscopy. It is almost similar to micro Raman spectroscopy except that its use of white light that cause less destructive compared to Raman. Other than that, FT-IR also used to reveal the chemical purity and the bonding structure of the synthesized GO, FGO and FG. A small amount of the samples in the form of powder was grounded with KBr powder to form pellets for FT-IR characterization. The FT-IR spectrum for GO,

FGO and FG were plotted in **Figure 4.16**. The vibrational modes and wavenumbers that exhibited by GO, FGO and FG based on our FT-IR result was listed in **Table 4.4**.

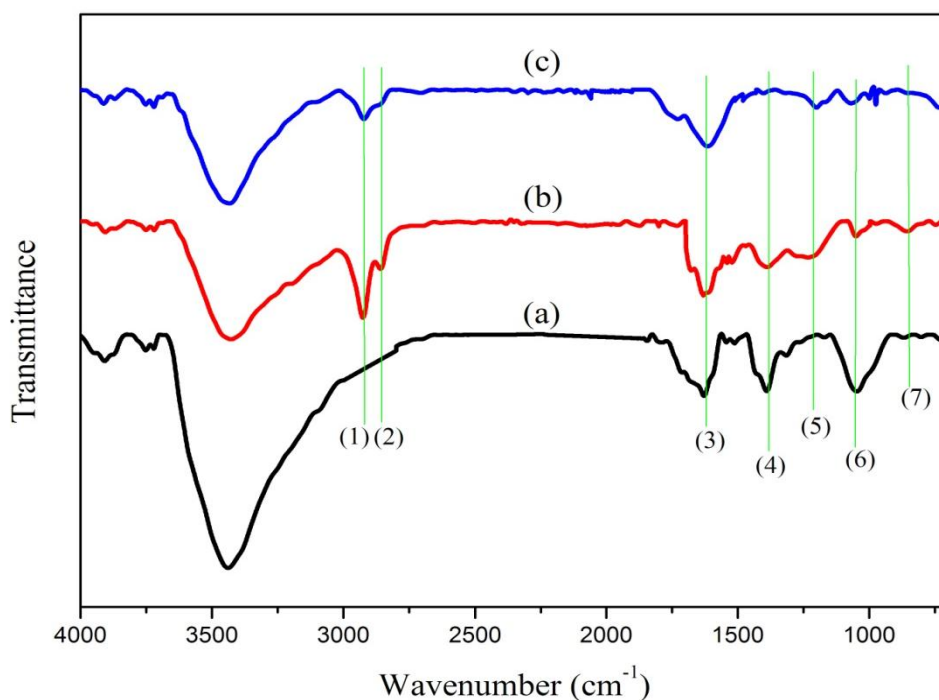


**Figure 4.16:** FT-IR spectrum for (a) GO, (b) FGO and (c) FG.

**Table 4.4:** Vibrational modes and wavenumbers exhibited by GO, FGO and FG based on our FT-IR result.

<i>Peak</i>	<i>Wavenumber (cm<sup>-1</sup>)</i>	<i>Vibrational modes</i>	<i>References</i>
(1)	2910	C-H stretching	(Yang, Li, et al., 2009)
(2)	2842	C-H stretching	(Yang, Li, et al., 2009)
(3)	1618	C=C stretching O-H bending	(Pham et al., 2010)
(4)	1405	O-H stretching	(Choi et al., 2010)
(5)	1210	C-N stretching	(De Palma et al., 2007)
(6)	1013	C-O-C bending	(Choi et al., 2010)
(7)	943	Si-OH stretching	(Hou et al., 2010)

We could see that all three samples have the same strong and broad peak at  $3425\text{ cm}^{-1}$  and  $1618\text{ cm}^{-1}$ , which is assigned to the O-H stretching and bending

vibration shows the intercalated free H<sub>2</sub>O molecules. The intensity of these peaks decreases and become weak when further hydrothermal reduction due to the lost of H<sub>2</sub>O molecules at higher temperature due to the removal of large fraction of O-H groups (*Pham et al., 2010*). The H<sub>2</sub>O molecules were not fully removed as the peak is still present after reduction. The water molecules does not fill up the defects and trapped between the interlayer space in FG sheets but rather exist in the surfaces of FG sheets.

In spite of the intercalation of water molecules, the band at 1618 cm<sup>-1</sup> may assigned to the C=C bonds which is related to the restoration of the sp<sup>2</sup> carbon networks during hydrothermal reduction (*Geng et al., 2010*). It is noted that all three spectrums show a similar peak at 1618 cm<sup>-1</sup> but different in intensity where FG shows the lower intensity due to the removal (cracking) on aromatic C=C bonds at higher temperature (*Huh, 2011*). Meanwhile, the FT-IR spectra of GO shows another two characteristics of oxygenic groups at 1405 cm<sup>-1</sup> and 1013 cm<sup>-1</sup> that can be ascribed to O-H and C-O-C stretching vibration. The reduction of FGO by removing the oxygen containing groups of GO is clearly reflected by the diminishing of the O-H peak and intensity reduction of C-O-C peak in the FT-IR spectra of FG (*Choi et al., 2010*). The decrease in intensity of C-O-C also may correspond to the decrease in amount due to most of it had reacted with silane molecules to form form C-N bonds. It is reasonable to consider that C-O-C on the GO surface has converted to  $\pi$ -conjugation by the hydrothermal reduction process.

FT-IR spectra for FGO and FG displayed double peaks at 2910 cm<sup>-1</sup> and 2842 cm<sup>-1</sup> corresponding to symmetric  $\nu_a$  CH<sub>2</sub> and asymmetric  $\nu_{as}$  CH<sub>2</sub> of the alkyl chains, which are assigned to EDTA-methylene groups of FGO and FG (*Yang, Li, et al., 2009*).

This band is absent in FT-IR spectra of GO and it is suggested the formation of functionalization of GO with the linking of silane molecules on its surfaces. Moreover, there is a peak at  $943\text{ cm}^{-1}$  appeared in the FT-IR spectrum of FGO, which denoted to the Si-OH stretching vibration that had been introduced to GO by the addition of EDTA-silane during the functionalization process (Hou *et al.*, 2010). This peak disappears after hydrothermal reduction due to the hydrolysis of Si-OH groups to form siloxane groups (Si-O-Si) which could be detected its presence by the peak at around  $1000\text{ cm}^{-1}$  (Yang, Li, *et al.*, 2009). The appearance of this peak further confirms the functionalization of GO and its reduction. The formation of FGO has also been confirmed further by the appearance of C-N stretching vibration at  $1210\text{ cm}^{-1}$  that associated with the attachment of EDTA-silane moieties (carboxylic acid to be specific) on the surfaces of GO (De Palma *et al.*, 2007).

TGA is a tool that continuously measures the weight of a sample as a function of temperature and time. It is valuable to note that we can correlate the volatilization of sample components, decomposition, oxidation and reduction as well as other changes corresponding to the weight changes that observed at specific temperatures. The TGA thermogram of weight loss over temperature for GO, FGO and FG were recorded start with the temperature of  $50\text{ }^{\circ}\text{C}$  to  $500\text{ }^{\circ}\text{C}$  with the rate of  $5\text{ }^{\circ}\text{C}/\text{min}$  that had been performed under nitrogen gas flow. The results are shown in **Figure 4.17**.

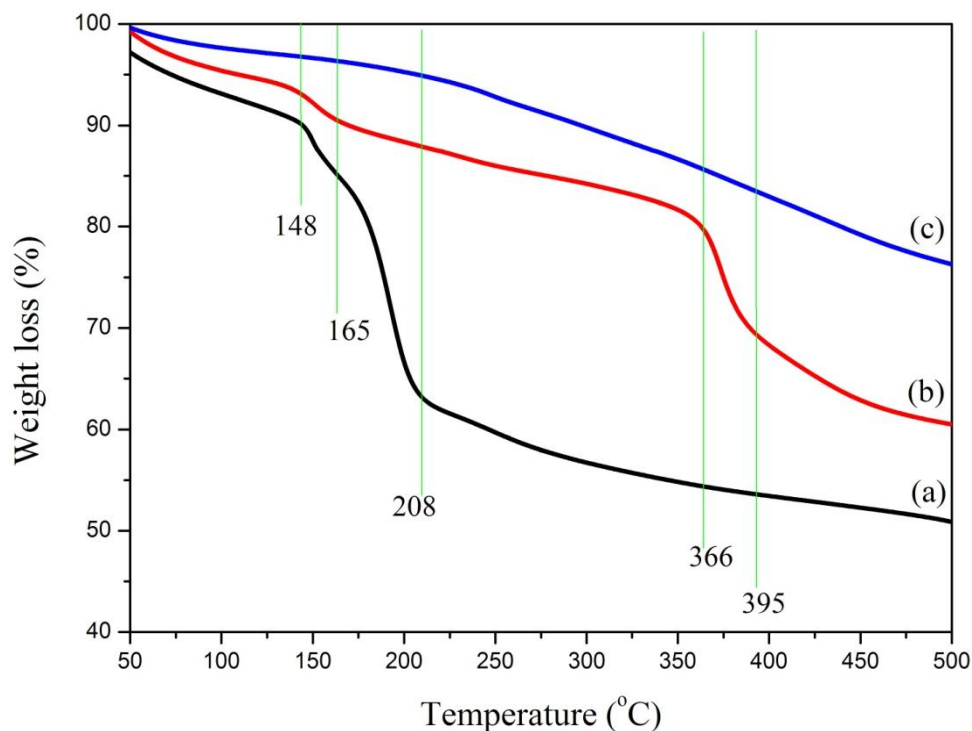


**Figure 4.17:** TGA thermogram for (a) GO, (b) FGO and (c) FG.

As shown in **Figure 4.17 (a)**, the TGA result shows that GO are detected to have three main regions where the first region started from room temperature to 148 °C with the weight lost is about 10 %. The second region which started from 148 °C to 208 °C shows the major mass reduction that is 27 % followed by a 13 % weight loss in the final region starting from 208 °C to 500 °C making the total weight loss until 500 °C is 50 %. We predict that the first region indicates the elimination of physisorbed water molecules. In the second region, pyrolysis of the most labile oxygen functional groups such as hydroxyl groups had occurred, which then released CO, CO<sub>2</sub> and steam (Eigler *et al.*, 2012). The lower rate of weight lost over temperature in the final region may attributed to the burning of more stable oxygen functionalities (Zhou *et al.*, 2010). It's been reported that carboxyl groups would probably be removed at this region due to the higher temperature that breaking the double bond between carbon and oxygen of the carboxyl group (Jeong *et al.*, 2009).

**Figure 4.17 (b)** shows the TGA plot for FGO with five main regions. The first region would be from room temperature to 148 °C with the loss of 6 % of absorbed water. The second region starts from 148 °C to 165 °C due to the removal of hydroxyl groups up to 3 %. Compared to GO, the weight loss is lower because GO is partially reduced during functionalization process thus the amount of oxygen containing groups will be less. The same reasons go to the third region which starts from 165 °C to 366 °C. Upon functionalization, some of the C-O-C bonds that located in the basal planes would react with silane molecules by opening the rings in epoxides thus allowed the attachment of silane molecules. Therefore, 11 % weight loss in region three is referred to the burning of these epoxides groups that is less on the weight loss compared to GO. The fourth region covers a range from 366 °C to 395 °C indicated the removal of 10 % weight of silane molecules as well as the elimination of the alkyl groups. The high temperature required to break the bonds as the bonds linking between them is strong. Lastly, the remaining oxygen functionalities in FGO would continue to burn as shown in the final region from 395 °C to 500 °C with the losses of 7 %. Noted that the total weight loss starting from the room temperature until 500 °C is less than GO which is only about 37 %, hence showing that FGO is more thermally stable than GO.

In the case of FG, the weight loss of 5% occurs at room temperature up to 208 °C, which could possibly due to the removal of remaining most stable oxygen functional groups that was not reduced during the reduction process. The losses are much lower as compared to GO and FGO indicates a significantly decreased amount of oxygenated functional groups where most of them had been removed by hydrothermal reduction (*Stankovich et al., 2007*). This result could also be related to the diminishing of oxygen containing groups peaks which reflected in the FT-IR spectrum of FG. There

is a weight loss observed from 208 °C until 500 °C with the losses of 18 % weight corresponding to the decomposition of the surface-bound silane molecules. The total weight loss of FG is 23 % thus making it's the most thermally stable compared to GO and FGO. This result also confirmed the reduction of FGO has occurred.

#### 4.3.2 Morphological characterization: FESEM and TEM analysis

The GO, FGO and FG were characterized using the FESEM and TEM characterization in order to observe the structure and surface morphology of all the samples. The samples were prepared by drop casting the diluted dispersion onto a Si/SiO<sub>2</sub> substrate for FESEM and onto the copper grid for TEM characterization. The FESEM and TEM images for GO are shown in **Figure 4.18 (a)** and **(b)**, respectively. It is clearly seen from the FESEM image that the surface of GO is formed into a series of rounded folds; a cloud-like structure. This corrugation of the GO sheets is attributed to the disruption of the planar sp<sup>2</sup> carbon sheets by the introduction of sp<sup>3</sup>-hybridized carbon upon oxidation (*Wang et al., 2009*). The presence of residual H<sub>2</sub>O molecules tightly bound with carboxyl or hydroxyl group of GO may also lead to this morphologies (*Ju et al., 2010*).

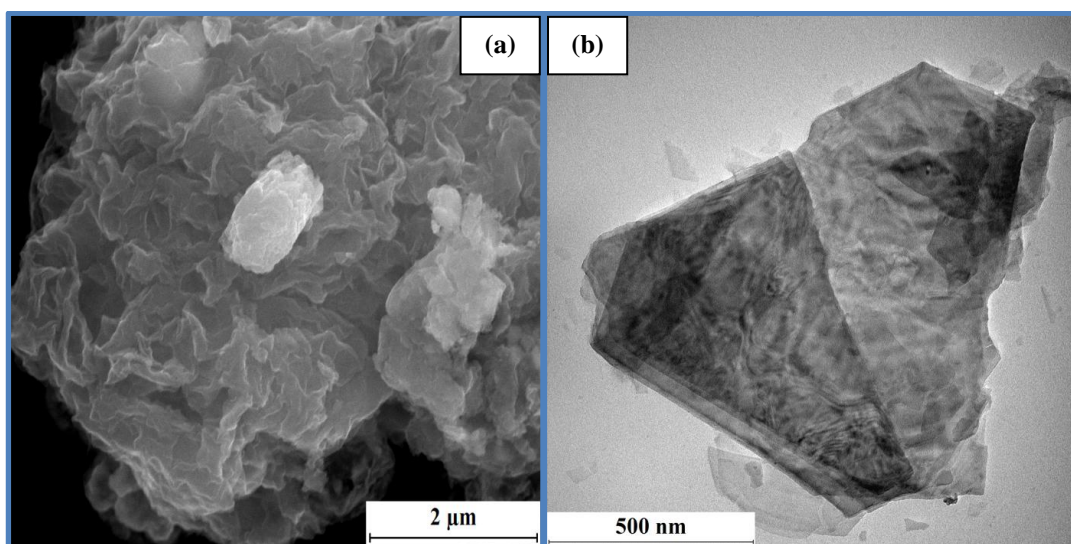


**Figure 4.18:** (a) FESEM and (b) TEM images for GO.

The GO flakes possess an average lateral dimension of more than 1  $\mu\text{m}$  that appears to be built up from a few larger flakes of graphene that stack together to form thicker GO flakes with wavy wrinkles on its surfaces as visualized by TEM. The stacking of few graphene sheets might cause the increase in thickness of GO. Besides that, the GO has a higher thickness may be due to the presence of covalently bonded oxygen and the displacement of  $\text{sp}^3$  hybridized carbon atoms slightly above and below the original graphene plane (*Zhao et al., 2010*). The darker image of GO observed in the TEM image further proof that GO consist of a few layers of graphene that stack together.

**Figure 4.19** shows typical FESEM and TEM images of FGO sheets obtained by the silanization process of GO. It is worth noting that these FGO sheets have an average lateral dimension of more than 5  $\mu\text{m}$  with almost smooth surface in the middle and a few crumpled sheets at the edges as clearly observed in the FESEM image (**Figure 4.19 (a)**). The partial removal of oxygen containing groups at the middle and the linking of silane molecules at the edges of GO sheets after functionalization process may lead to this structure of FGO sheets. The decrease of van der Waals interlayer interactions due to the presence of silane molecules would make the GO layers easier to cleave thus forming thin FGO sheets that consists of fewer layers of graphene comparatively to GO. The semi-transparency of FGO sheets as seen in the TEM image (**Figure 4.19 (b)**) further evidence the existence of thin FGO sheets with a reduction in its thickness. Moreover, these FGO have a clearly sheetlike structure in nature even though it is slightly overlapping proving the well ordered of the graphene sheets.

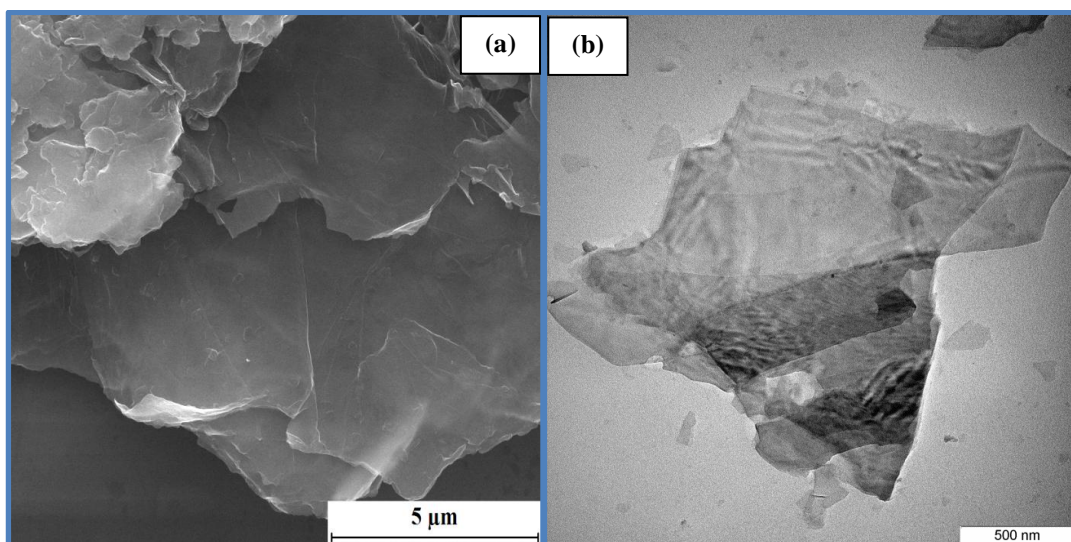


**Figure 4.19:** (a) FESEM and (b) TEM images for FGO.

The SEM and TEM images of FG exhibited a layered structure of FG sheets. After silanization and hydrothermal treatment, the cloudy-like structure was destroyed and the GO could be effectively separated into very thin FG sheets, as taken from FESEM visualized in **Figure 4.20 (a)**. The average lateral dimension of these FG sheets is about 2 to 3  $\mu\text{m}$ . As compared to FGO sheets, these FG sheets have smaller area that is attributed to the breaking of larger sheets into a small domain after the hydrothermal reduction due to the higher temperature (*Su et al., 2009*). Zhao et al. reported that the area of GO correlated with the content of C-O bond (*Zhao et al., 2010*). The larger amount of C-O bonds would produce a larger area of GO. Hence, we believed that the larger area of FGO corresponds to the larger content of C-O bonds. These C-O bonds would break in further hydrothermal reduction at temperature 180  $^{\circ}\text{C}$ , thus forming FG sheets with the decrease in area. Besides that, Shen. et al. also reported that the formation of graphene with smaller size but numerous in number happened because some fragmentation occurred along the reactive sites during the reduction process thus yields new graphitic domains which lead to the smaller size of grapheme (*Shen et al., 2010*). In this regard, the results also in turn indicate the

effectiveness of the functionalization methodology because it prevents the agglomeration of GO sheets thus facilitate the further anchoring of other material especially metal oxide and wider its application.

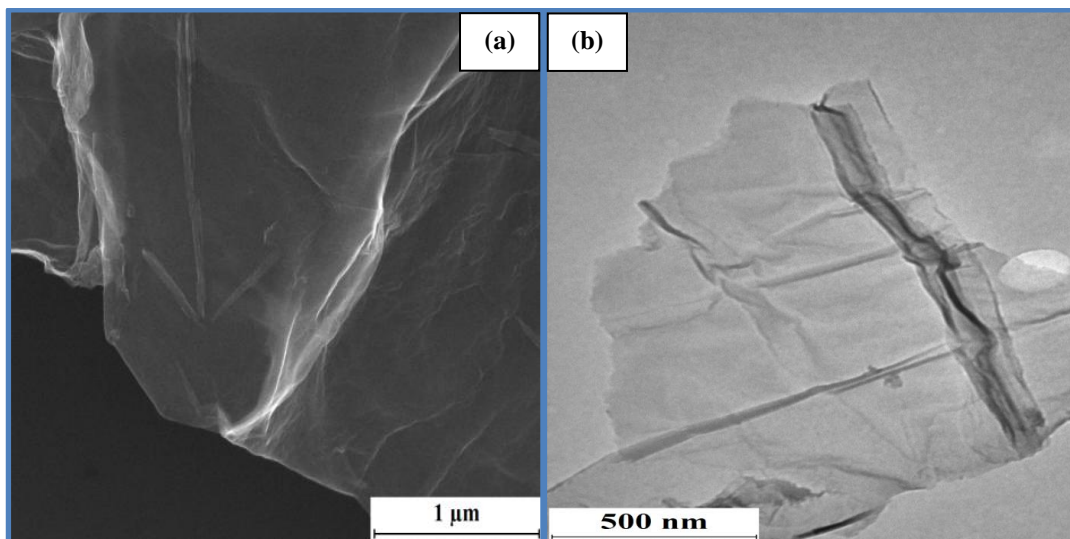


**Figure 4.20:** (a) FESEM and (b) TEM images for FG.

### 4.3.3 Optical characterization: UV-vis spectroscopy analysis

**Figure 4.21** displays the difference in the UV-vis spectra of GO, FGO and FG. The insert is the digital images of GO, FGO and FG which show the difference in color between the samples that had been dissolved in deionized water. We can see the color changes from brown to dark brown after functionalization process and further changes to black after hydrothermal reduction. Upon adding the EDTA-silane into GO solution, an alkaline solution would form with a pH value of about 10. It is believed that under this condition, GO would undergo partially deoxygenation and cause in its color changes after functionalization. When FGO was treated under hydrothermal reduction, oxygen groups especially hydroxyl and epoxy group could be removed from FGO surfaces thus reflect on the color changes from dark brown to black.

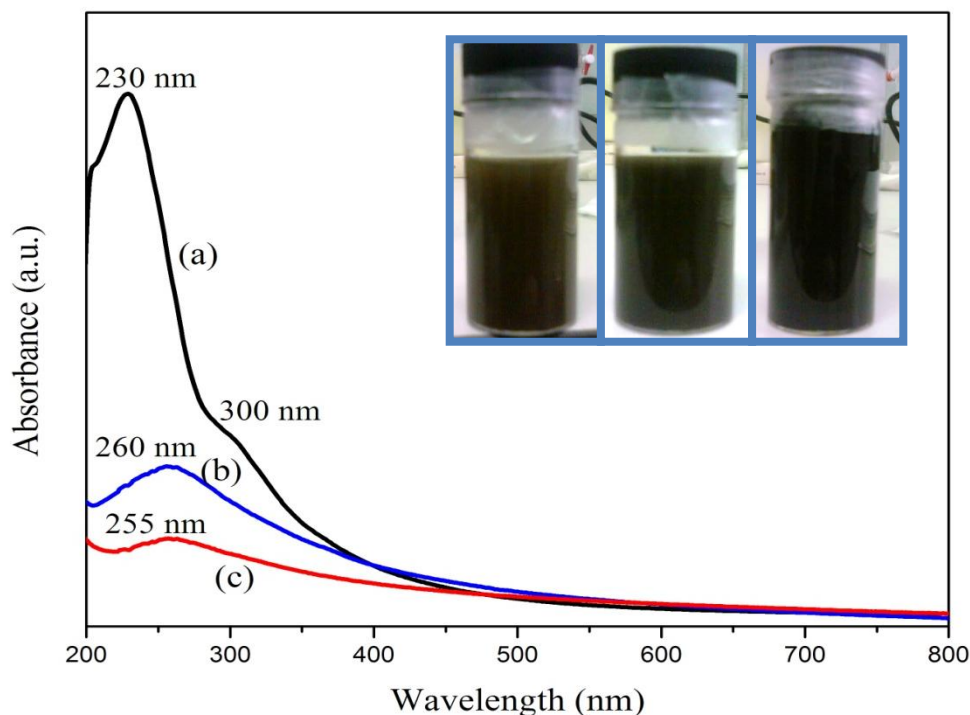


**Figure 4.21:** UV-vis spectra of (a) GO, (b) FGO and (c) FG.

From the UV-vis spectrum, we could observe that GO exhibits a strong absorption peak at 230 nm and a shoulder at around 300 nm. This maximum absorption peak is corresponding to the  $\pi \rightarrow \pi^*$  transitions of aromatic C-C bonds while the shoulder occurred due to the  $n \rightarrow \pi^*$  transition of C=O bonds (carbonyl groups) (Paredes *et al.*, 2008). Marcano *et al.* reported that the degree of remaining conjugation can be determined by the  $\lambda_{\max}$  of UV-vis spectrum where the higher  $\lambda_{\max}$  is attributed to the mayor  $\pi \rightarrow \pi^*$  transitions (conjugation) as only less energy is needed to be used for the electronic transition (Marcano *et al.*, 2010). Besides that, the red shifting of  $\lambda_{\max}$  also can be used as a yardstick to estimate the degree of reduction as suggested by Merino *et al.* (Fernandez-Merino *et al.*, 2010). The maximum red shifted indicates a higher degree of reduction.

For FGO, the maximum absorption peak is recorded at 255 nm with the absorption peak at 300 nm disappeared. This peak is attributed to the linking of silane molecules to the GO surfaces via hydroxyl containing groups such as –OH and –COOH (*Shifeng Hou et al., 2010*). The phenomenon of red shifting about 25 nm from GO spectrum indicates a considerable partially deoxygenation of GO by the functionalization process. After the hydrothermal treatment, the peak red-shifted to 260 nm suggests the effective restoration of the  $sp^2$  carbon networks (C=C bonds) within the FG sheets (*Li et al., 2008*). Moreover, this bathochromic shift further confirmed that FGO had been reduced to FG with the highest degree of reduction compared to FGO.

#### 4.3.4 Formation mechanism of GO, FGO and FG

In general, one of the ways to trace the difference the between GO, FGO and FG and also confirmed its formation is through the study of chemical structures. Here, we purpose the possible mechanism for the formation of GO, FGO and FG. In the case of GO, a method was developed to prepared GO based on the oxidation process where graphite flakes will act as the starting materials. In this study, the GO samples were prepared by simplified Hummers' method where the final samples obtained from the oxidation of graphite flakes followed by the exfoliation of graphite oxide into GO.

It is well known that graphite is composed of stacking of few layer graphene with the d-spacing between layers is about 0.34 nm due to the tightly packed monolayer of carbon atoms. Using simplified Hummers' method, graphite flakes will start to oxidize induced by the presence of acidic solvent that are made up from a mixture of  $H_2SO_4$  and  $H_3PO_4$  to form the graphite oxide. It will further oxidize by the addition of excess  $KMnO_4$  which also known as one of the strongest oxidation agents. During the

stirring and washing process, graphite oxide will undergo an exfoliation process to make it thin as one carbon layer described as GO.

It is well-known that the oxidation process could break the  $\pi$ - $\pi$  conjunction with the original graphite structure to form graphite oxide (Wang *et al.*, 2011). Upon oxidation and exfoliation, the interlayer spacing started to increase in the range of 0.6 to 0.8 nm due to the disruption on the  $sp^2$  bonded carbon network of graphite which makes the new structure of GO disordered. The existence of ketone, epoxy, and the hydroxyl groups in GO which bonded with a significant fraction of carbon network also be among the result of these oxidation processes. By adding these oxygen containing groups, the van der Waals force that holds the graphene sheets together will reduce hence allowed exfoliation to happen upon sonication thus lead to the increase of its interlayer spacing. It has been reported before that at this stage, the GO structure consists of intact graphitic regions interspersed with  $sp^3$  hybridized carbons containing hydroxyl and epoxide functional groups on the top and bottom surfaces of each sheet and  $sp^2$  hybridized carbons containing carboxyl and carbonyl groups mostly at the sheet edges (Stankovich *et al.*, 2006). The attachment of hydroxyl (-OH) groups on the surface of GO nanosheets resulted the hydrophilicity of GO forming aqueous solution in water and any solvent.

More details about the oxidation mechanism of graphite sheets had been reported by Shao *et al.* (Shao *et al.*, 2012) and illustrated in **Figure 4.22**. In the first stage of oxidation process, a large number of phenolic groups produced at the edges where then defects on the basal plane of graphene sheets under strong oxidation of  $KMnO_4/H_2SO_4$ . Under the same condition the single bonds had been formed from the transformation of the double bonds that attached to these chemical reaction points as

shown in **Figure 4.22b**. When we further extended the oxidation process, two processes have a possibility to be happening concurrently. One of it is the condensation of part of phenolic group to form C–O–C (ether) linkages (**Figure 4.22c, oval**) and the other one is the oxidation of a small proportion of phenolic groups at the edges or defects to two adjacent ketone groups, that is, the phenolic groups were oxidized to quinone groups as illustrated in **Figure 4.22c, square**. Next, the COOH groups were formed from the conversion of the ketone groups (**Figure 4.22d, square**). It is believed that the COOH groups might decarboxylated easily and C–C bond between them would cleave if it was carboxyl or carbonyl groups that adjacent to COOH groups which owing to the electrophilic effect and anionic mechanism. However, one CH<sub>2</sub> could form (**Figure 4.22d, oval**) if there were three carbons that attached to hydrogen at the edges in one benzene ring were oxidized. On the other hands, there were still some ketone and quinone groups left. Hence, as the oxidation proceeded the amount of oxygen functional groups will increased except for phenolic groups.

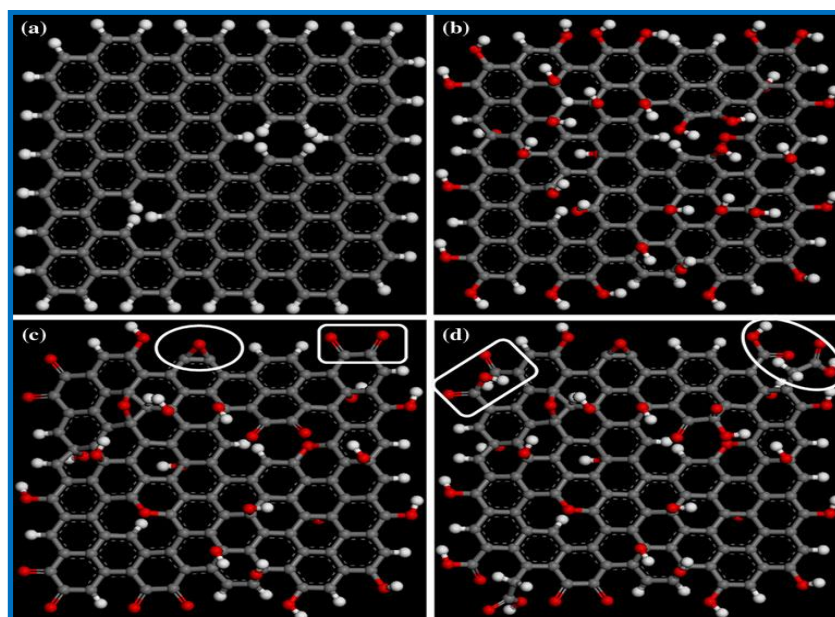


**Figure 4.22:** The oxidation mechanism model of graphite sheets (*Shao et al., 2012*).

Previously reported that the oxidation and exfoliation of graphite may induce a variety of defects and oxygen containing functional groups such as hydroxyl and epoxide (*Luo et al., 2011*) resulting in the degradation of the electronic properties of graphene (*Pei et al., 2012*). Therefore, one of the way to repair some of the defects thus account for the improvement of electronic properties of graphene is by chemical functionalization of GO. As such, GO could serve as an excellent precursor for fabrication of a new material with modification on its surfaces via silanization process described as FGO attributed to the presence of oxygen functionalities at GO surfaces that provide reactive sites for chemical modification using known carbon surface chemistry (*Marques et al., 2011*). The stable aqueous dispersion of FGO is simply obtained by refluxing dried GO in the solution of ethanol with the presence of EDTA-silane under heat treatment at temperature 65 °C. In this process, a new functional group that is the silane molecules was introduced to linkage at the surface of GO.

In general, the linking of silane molecules onto the carbon surfaces can be made using two routes. One approach involves a chemical covalent linkage between amine groups and the activated carbon surface as reported by Yuen *et al.* (*Yuen et al., 2008*). Zhu *et al.* have produced modified graphene using the second process which involves a chemical reaction between the trialkoxy groups of silane and the hydroxyl groups on the carbon surface (*Zhu et al., 2010*). In this study, we employed the second route, in which silane molecules were linked to the RGO and GO surfaces via hydroxyl-containing groups such as -OH and -COOH.

Hou *et al.* presented the possible reaction mechanism involved in the fabrication of FGO which can be described in three steps (*Hou et al., 2010*). In the first step, a large amount of C-OH groups had been introduced on the GO surfaces due to

the oxidation process of graphite. Next, the hydrolysis of the trialkoxy groups of silane groups will take place in the second step which will generate  $-\text{Si}-\text{OH}$  groups. Lastly, the reaction between  $\text{Si}-\text{OH}$  and  $\text{C}-\text{OH}$  of GO links EDTA-silane to the GO surface through  $\text{Si}-\text{O}-\text{C}$  bonds. This resulted in more negatively charged on the surface of GO due to the presence of highly  $\text{COO}^-$  and  $-\text{OH}$  groups on both sides of GO and this new material is described as FGO.

In order to obtain the FG sheets, FGO needs to undergo the reduction process. Cheng *et al.* revealed that the reduction of GO has dedicated to achieving two main targets which includes elimination of the functional groups and further healing the structural defects (Cheng *et al.*, 2012). For the elimination of functional groups, the reduction of GO must be mainly aimed at eliminating epoxy and hydroxyl groups on the plane while in the same time healing the structural defects. Thus, if these lattice defects can be healed during reduction, the GO could possibly behave as perfect graphene.

Herein, the FG sheets was obtained by thermal reduction of FGO under hydrothermal condition at temperature 180 °C. The hydrothermal method could promote the recovery of  $\pi$ -conjugation after dehydration, which is favorable for minimizing defects. This behavior can presumably be attributed to the relatively high temperature and internal pressure in a closed system (Zhou *et al.*, 2009). Beside that, most of the FGO oxygen-containing functional groups were reduced during the hydrothermal process, thereby increasing the thermal stability of this new material named FG. **Figure 4.23** illustrates the reduction process of FGO to form FG sheets. The possible reaction mechanism can be described as follows: (1) Oxygen groups in FGO are largely removed (2) defects are successfully repaired during this restoring

approach. However, the detailed formation process on the defect repair process is still unclear, which needs further discussion.

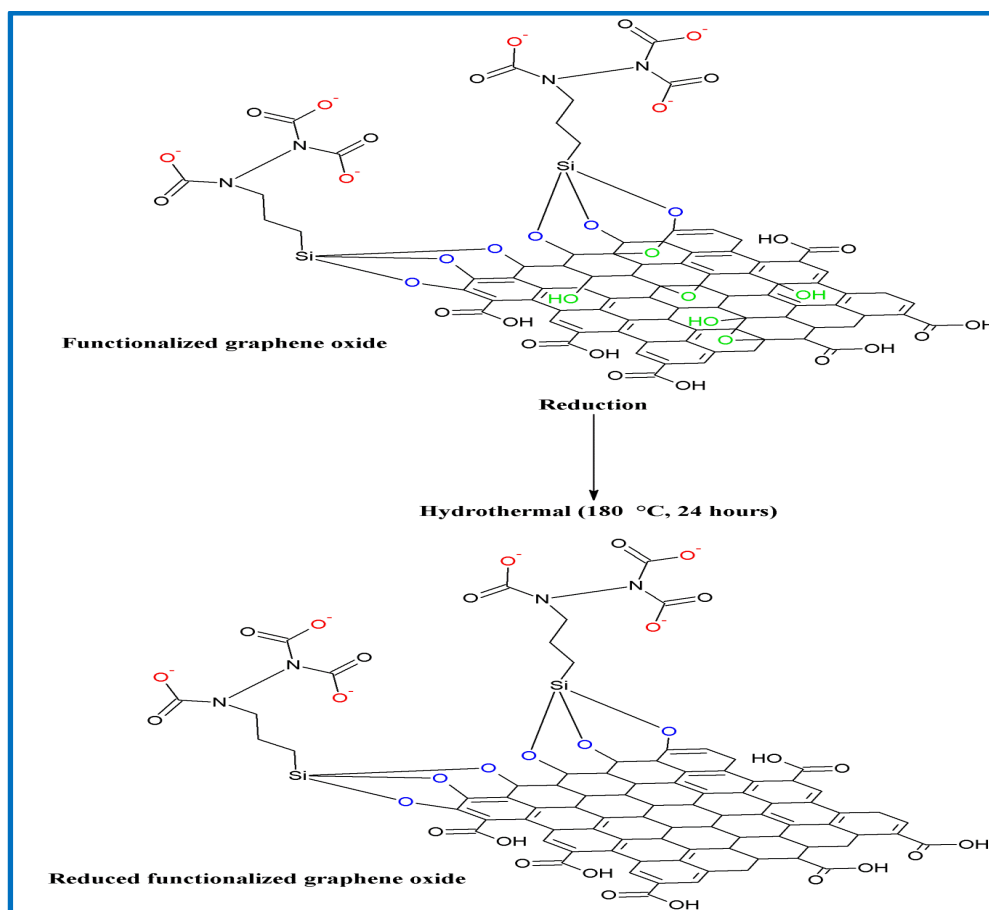


**Figure 4.23:** Formation of FG via hydrothermal method.

#### 4.4 Results for synthesis of rGO/CuO and FG/CuO nanocomposites

The last part of this chapter presents the results for synthesis of rGO/CuO and FG/CuO nanocomposites that cover the possible formation mechanism and the study of its catalytic activity. In order to study the effect of different mass ratio, FG/CuO nanocomposites with three different mass ratio has been prepared and characterized by using XRD, micro Raman, TGA, FESEM, TEM and also the catalytic activity. All the results are discussed and presented in this last part of Chapter 4.

#### 4.4.1 Structural characterization: XRD, micro Raman, and TGA analysis

XRD measurements were employed to investigate the phase purity and composition of the as-synthesized samples as well as to confirm the formation of graphene hybridized CuO nanocomposites. The XRD patterns of FG, rGO/CuO and three nanocomposites samples, prepared with different amount of FGO, are shown in **Figure 4.24**. The XRD pattern of FG showed a broad diffraction peak at  $2\theta$  of  $\sim 13^\circ$  (**Figure 4.24 (a)**) with d-spacing of  $6.10 \text{ \AA}$ , suggesting that FGO is reduced to FG and the carbon  $sp^2$  bonding restored after hydrothermal reduction. **Figure 4.24 (b)** shows the XRD pattern for rGO/CuO nanocomposite where all the diffraction peaks that can be indexed to the monoclinic CuO particles except for a small peak at  $2\theta = 26^\circ$ . This weak peak is the characteristic peak of residual graphite unoxidized. The absence of GO peak at around  $10^\circ$  indicates that GO has been reduced to graphene. The absence of other than CuO peaks reveals that rGO/CuO nanocomposite has been produced after hydrothermal reaction.

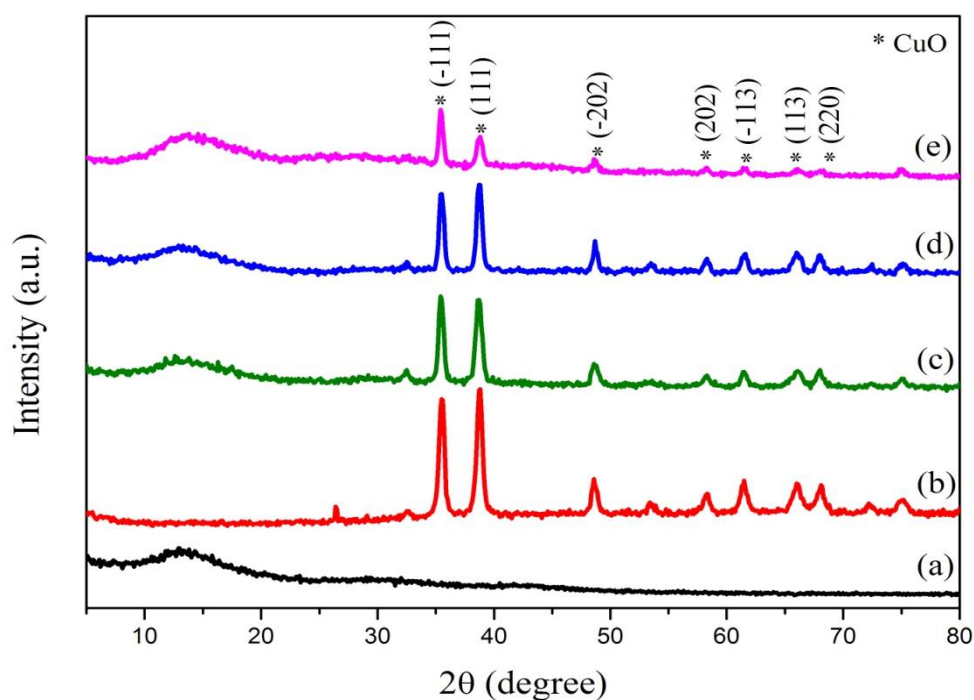


**Figure 4.24:** XRD patterns of (a) FG, (b) rGO/CuO, (c) 2 mg FG/CuO, (d) 20 mg FG/CuO and (e) 30 mg FG/CuO nanocomposites.

The composition of FG/CuO nanocomposites with three different amounts of FGO were examined by XRD, as shown in **Figure 4.24 (c-e)**. The peak of the samples at  $35.54^\circ$ ,  $38.73^\circ$ ,  $48.74^\circ$ ,  $58.31^\circ$ ,  $61.55^\circ$ ,  $67.93^\circ$  and  $68.15^\circ$  are indexed to (-111), (111), (-202), (202), (-113), (113) and (220) planes of monoclinic CuO (JCPDS 41-0254), respectively. These samples have a similar hump at  $\sim 13^\circ$ , which is contributed by FG, revealing the hybridization of the two materials. We could also observe that this peak is slightly shifted to the right as the amount of FGO is increased suggesting that further exfoliation of FGO sheets has occurred by the crystal growth of CuO between the interlayers during the hydrothermal reaction. No diffraction peak assigned to other than these two elements could be observed thus confirming the successful preparation of FG/CuO nanocomposite by using hydrothermal method.

The XRD result of all three FG/CuO nanocomposites shows sharper peaks of CuO suggesting that these nanocomposites composed of CuO with higher crystallinity. The broadening of CuO peaks could be observed as we added more FGO in the composites, following the order of: 2 mg < 20 mg < 30 mg. The decrease in the size of CuO with the increase in the amount of FGO is supported by the broadening of the diffraction peaks at higher FG content (*Ji et al., 2011*). We could also observe that the intensity of FG peak increases with the additional amount of FGO sheets and smaller CuO sizes. From this observation, it is clear that larger CuO particle sizes would cover a bigger area of FG sheets thus allowed a smaller signal from FG sheets to be detected, reflected in the lower intensity of FG peak. Therefore, the peak of FG with lower intensity was shadowed by the high intensities of CuO peaks.

Moreover, the d-spacing of FG sheets at diffraction angle of  $13^\circ$  in the 2 mg, 20 mg and 30 mg FG/CuO nanocomposites were calculated and found to be about 6.68 nm, 6.61 nm and 6.24 nm, respectively. However, the d-spacing for FG sheets itself is calculated to be about 6.10 nm which is less as compared to the one obtained from the three nanocomposite. This is because the growth of CuO nanoparticles between the interlayer would help the exfoliation of FGO thus increase its d-spacing. Besides that, CuO nanoparticles would also act as a spacer to keep FG layers separated (Zhou, Ma, et al., 2011). The summary of information obtained in this analysis is shown in **Table 4.5**.

**Table 4.5:** Properties of rGO/CuO and FG/CuO nanocomposites with an appropriate amount of FGO flakes obtained by XRD analysis.

<i>Materials (nanocomposites)</i>	<i>Peak position, <math>2\theta</math> (<math>^\circ</math>)</i>	<i>FWHM (rad)</i>	<i>d-spacing (<math>\text{\AA}</math>)</i>
<i>rGO/CuO</i>	35.46	0.0085	3.60
<i>2 mg FG/CuO</i>	35.45	0.0086	6.68
<i>20 mg FG/CuO</i>	35.49	0.0096	6.61
<i>30 mg FG/CuO</i>	35.46	0.0104	6.24

Micro Raman spectrum is a powerful tool for the characterization of carbon based materials as it is one of the most sensitive and informative techniques to probe the presence of disorder in  $sp^2$  carbon materials. **Figure 4.25** shows the micro Raman spectrum for FG, rGO/CuO and FG/CuO nanocomposites with an appropriate amount of FGO flakes. All samples display two prominent peaks that assigned to the D and G peaks. Typically the D peak arises from defects in the hexagonal  $sp^2$  carbon network or the finite particle size effects (Ferrari et al., 2001) while G peak originates from the stretching motion of  $sp^2$  hybridized carbon atoms in both rings and chains (Pimenta et al., 2007). The three peaks allocated between  $280\text{ cm}^{-1}$  to  $614\text{ cm}^{-1}$  are indexed to CuO

cannot be seen clearly and almost diminish (**Figure 4.25 (b-e)**) because it had been shadowed by the higher intensities of D and G peaks belonging to the graphene sheets.

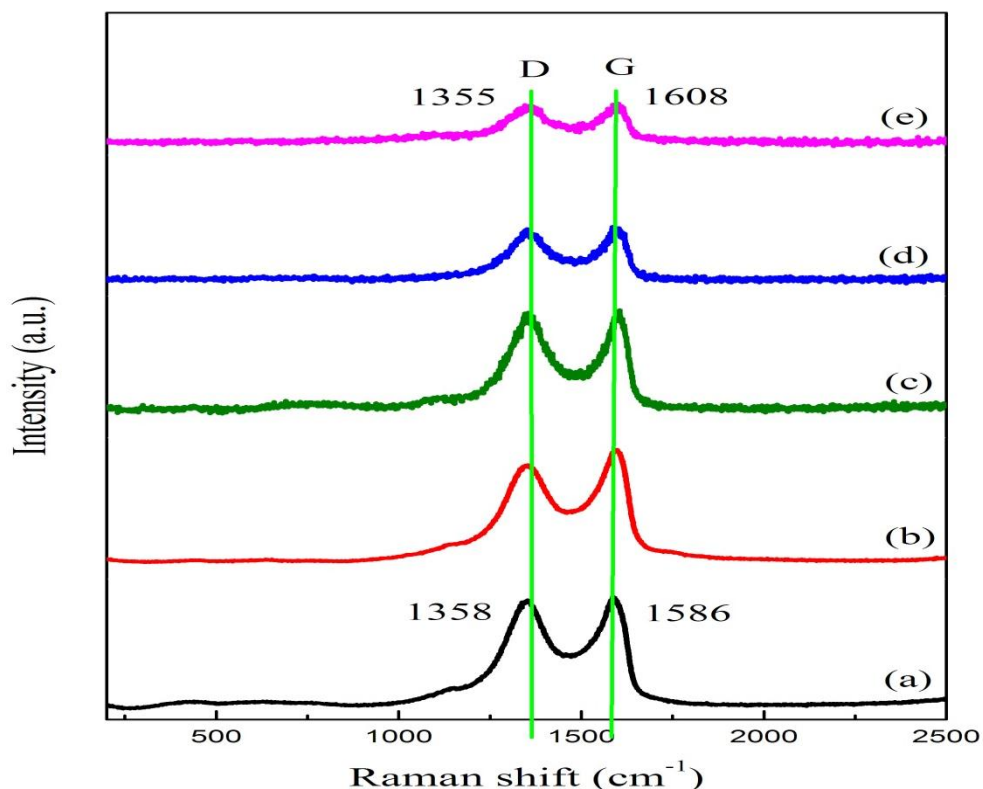


**Figure 4.25:** Micro Raman spectra for (a) FG, (b) rGO/CuO, (c) 2 mg FG/CuO, (d) 20 mg FG/CuO and (e) 30 mg FG/CuO nanocomposites.

For FG, the D and G peaks allocated at  $1358\text{ cm}^{-1}$  and  $1586\text{ cm}^{-1}$ , respectively with an intensity ratio of D band to G band ( $I_D/I_G$ ) is about 1.01. However, these D and G peak position slightly red-shifted to  $1355\text{ cm}^{-1}$  and blue-shifted to  $1608\text{ cm}^{-1}$ , respectively for the case of 30 mg FG/CuO nanocomposite and it is shifted to a lower wavenumbers as the amount of FGO varies from 30 mg FGO to 2 mg FGO (**Figure 4.26**). These shifts in the Raman peak could be attributed to the chemical interaction between CuO and FG sheets (*Xu et al., 2011*). It has been reported before that the presence of charge transfer between carbon with other compounds could be detected by the shifted of G band position (*Rao et al., 1997; Zhou, Song, et al., 2011*). So the shift in G peak by  $22\text{ cm}^{-1}$  (**Figure 4.26 (e)**) from G peak position in the micro Raman

spectrum for FG associated with the charge transfer from FG to CuO particles as well as the formation of a new bonding between them. The sample with 30 mg FGO shows the highest blue-shifted of G band, this may indicate that it has the strongest interaction as the interaction will be stronger in line with the shift towards higher wavenumbers.

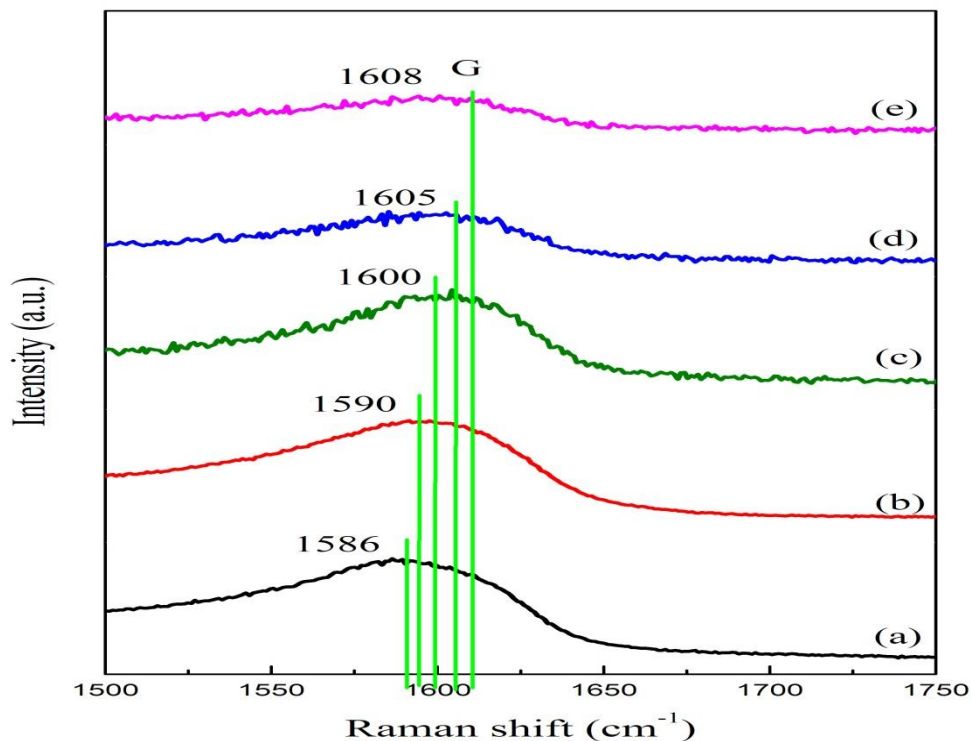


**Figure 4.26:** Enlarged G band for (a) FG, (b) rGO/CuO, (c) 2 mg FG/CuO, (d) 20 mg FG/CuO and (e) 30 mg FG/CuO nanocomposites.

For FG, the D and G peaks allocated at  $1358\text{ cm}^{-1}$  and  $1586\text{ cm}^{-1}$ , respectively with an intensity ratio of D band to G band ( $I_D/I_G$ ) is about 1.01. However, these D and G peak position slightly red-shifted to  $1355\text{ cm}^{-1}$  and blue-shifted to  $1608\text{ cm}^{-1}$ , respectively for the case of 30 mg FG/CuO nanocomposite and it is shifted to a lower wavenumbers as the amount of FGO varies from 30 mg FGO to 2 mg FGO (**Figure 4.26**). These shifts in the Raman peak could be attributed to the chemical interaction between CuO and FG sheets (*Xu et al., 2011*). It has been reported before that the presence of charge transfer between carbon with other compounds could be detected by

the shifted of G band position (*Rao et al., 1997; Zhou, Song, et al., 2011*). So the shift in G peak by  $22\text{ cm}^{-1}$  (**Figure 4.26 (e)**) from G peak position in the micro Raman spectrum for FG associated with the charge transfer from FG to CuO particles as well as the formation of a new bonding between them. The sample with 30 mg FGO shows the highest blue-shifted of G band, this may indicate that it has the strongest interaction as the interaction will be stronger in line with the shift towards higher wavenumbers.

It is also found that the intensity of D to G band for the nanocomposite is slightly higher than that of FG (1.01). The  $I_D/I_G$  for rGO/CuO nanocomposite is calculated to be about 1.10 and increased to 1.08, 1.05 and 1.03 for 2 mg FG/CuO, 20 mg FG/CuO and 30 mg FG/CuO nanocomposites, respectively. This happened due to the intercalation of CuO nanoparticles with different sizes into FG sheets (*Lu et al., 2011*) which then lead to the different degree of disorder in FG. It has been reported that the  $I_D/I_G$  is proposed to be an indication of disorder in graphene originating from defects associated with vacancies, grain boundaries, and amorphous carbons (*Fan et al., 2011*). Therefore, in our case, the 30 mg FG/CuO nanocomposite with the lowest  $I_D/I_G$  may contain the lower concentration of defects because the smaller size of CuO nanoparticles had occupied most of the vacancies in FG thus recovered its defects.

TGA is one of the important characterization used to study the thermal stability and composition of the nanocomposites. **Figure 4.27** shows the thermogravimetric curves of FG and the nanocomposites where we could observe that the functionalization and reduction of GO and further hybridization with CuO had improved the thermal stability of GO. It is obviously seen that rGO/CuO nanocomposite shows the weak thermal stability with the total percentage of weight loss after heated up to  $500\text{ }^\circ\text{C}$  is about 75 % (**Figure 4.27 (b)**). At the first stage, 4 %

weight loss was detected below 108 °C which is assigned to the evaporation of the physisorbed water. Next, 5 % of weight has losses in the temperature range of 108 °C to 117 °C due to the decomposition of labile oxygen groups in the graphene, and continue to losses 7 % weight slowly until reaching the temperature of 290 °C. An abrupt weight loss (59 %) occurs between 290 °C and 342 °C which was possibly due to the oxidation and decomposition of residual oxygen groups in graphene that was not fully reduced during hydrothermal reduction (*K. Zhou et al., 2010*).

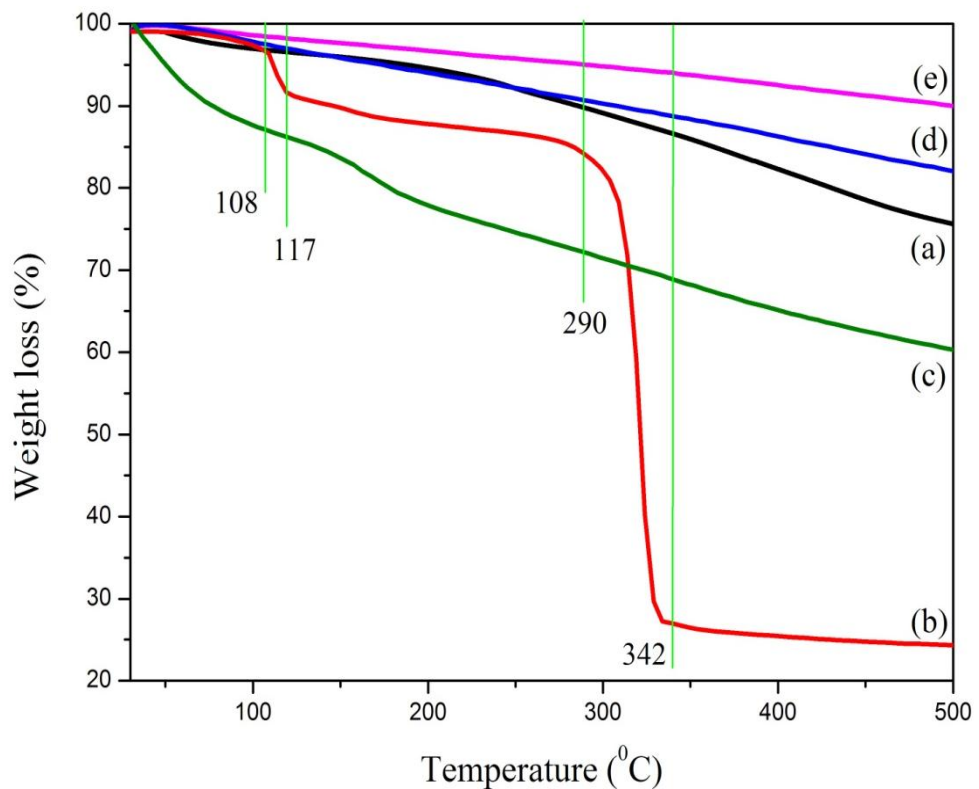


**Figure 4.27:** Thermogravimetric curve of (a) FG, (b) rGO/CuO, (c) 2 mg FG/CuO, (d) 20 mg FG/CuO and (e) 30 mg FG/CuO nanocomposites.

The FG/CuO nanocomposites with an appropriate amount of FGO flakes displayed different weight loss in the temperature range from room temperature to 500 °C as shown in **Figure 4.27 (c-e)**. 2 mg FG/CuO have a total weight loss of about 38 %, 20 mg FG/CuO have a total weight loss of about 18 %, and 30 mg FG/CuO have a total weight loss of about 10 %.

followed by 20 mg FG/CuO with 15 % weight loss and lastly the 30 mg FG/CuO nanocomposite with weight loss of about 10 %. For 2 mg FG/CuO, the weight loss of 23 % below 200 °C is corresponding to the loss of water while another 15 % weight loss at temperature above 200 °C to 500 °C indicates the removal of the residual oxygen functional group in FG. We could see that this nanocomposite started to decompose the carbon in FG at temperature 200 °C while decomposition of carbon in FG starting from 290 °C, thus showing that the thermal stability of FG is decreased after forming a composite with CuO nanoparticles. This happens due to the catalytic effect of CuO (*Zhao et al., 2012*).

By comparison with the curve of FG sheets, it can easily be concluded that both 20 mg and 30 mg FG/CuO nanocomposites had showed improvement in the thermal stability where the 30 mg FG/CuO nanocomposite is the most thermally stable. The nanocomposite exhibit a lower thermal degradation rate compared to that of FG and rGO/CuO nanocomposites, indicating the hybridization of FG with CuO can change individual thermal stabilization. The reason is that the FG could impose restrictions on mobilization of CuO nanoparticles and result in homogeneous heating and avoid heat concentration (*Hu et al., 2011*).

This implies that there is strong interaction between the FG and CuO. Besides that, the increased in the cross-linking density of FG/CuO may also result in the improvement of the thermal stability attributed to the so-called tortuous path effect of graphene, which retards the permeation of heat and the escape of volatile degradation products (*Wang et al., 2012*). These results clearly suggest that 20 and 30 mg FG/CuO nanocomposites possess higher thermal stability than FG and rGO/CuO nanocomposite. As the interaction between two materials become stronger, the thermal stability

becomes more stable. Therefore, 30 mg FG/CuO nanocomposite with the excellent thermal stability is speculated to have the strongest coupling interaction between the two materials.

#### 4.4.2 Morphological characterization: FESEM and TEM analysis

The FESEM and TEM characterization used to gain the direct evidence of the formation of CuO nanoparticles on the graphene sheets. **Figure 4.28 (a and b)** shows the FESEM images of rGO/CuO nanocomposite with only a few overlapping of rGO sheets that can be seen in these images and there is no any CuO nanoparticle could be detected on the surface of rGO. When the sample was further characterized by TEM, we could see a few CuO nanoparticles with an average size of larger than 20 nm are attached at the edge of rGO sheets as shown in **Figure 4.28 (c and d)**. It is believed that the CuO nanoparticles are attached to rGO sheets by the linkage between  $\text{Cu}^{2+}$  and  $-\text{COOH}$  groups at the edge of rGO sheets, induced by the electrostatic interactions. The less concentration of  $-\text{OH}$  groups on the surface of rGO sheets may result in the weak attachment of CuO nanoparticles to the sheets.

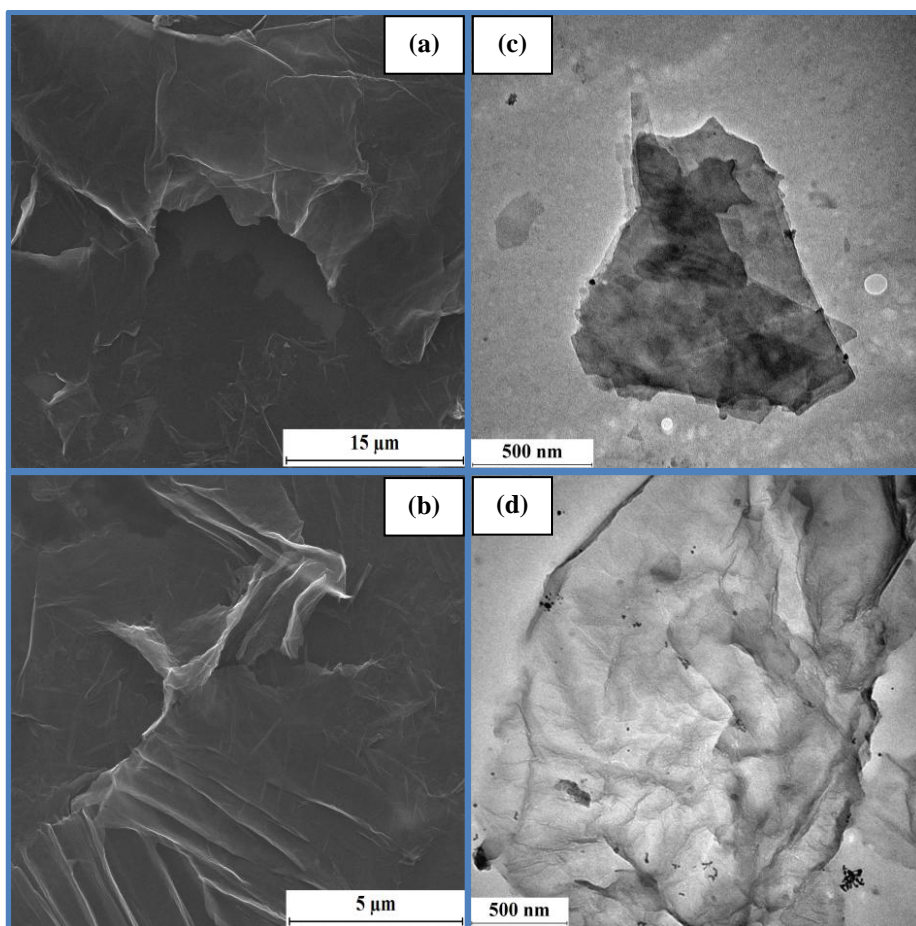


**Figure 4.28:** (a,b) FESEM and (c,d) TEM images of rGO/CuO nanocomposite.

When 2 mg of FGO was introduced to CuO, the nanocomposite shows an aggregation of needle-like CuO with an average length and width of 0.7 μm and 0.2 μm, respectively based on the FESEM images shown in the **Figure 4.29 (a and b)**. We could see that the FG sheet was completely covered by the relatively high amount of CuO. **Figure 4.29 (c and d)** shows the TEM images of 2 mg FG/CuO nanocomposite. The CuO are distributed randomly on the surface and edges of the FG sheets which further evidence for the introduction of more functional groups especially the –COOH and –OH groups on the FG sheets after the functionalization process. These functional groups on the surface of FG sheets would act as an ligand for the adherence of CuO particles.

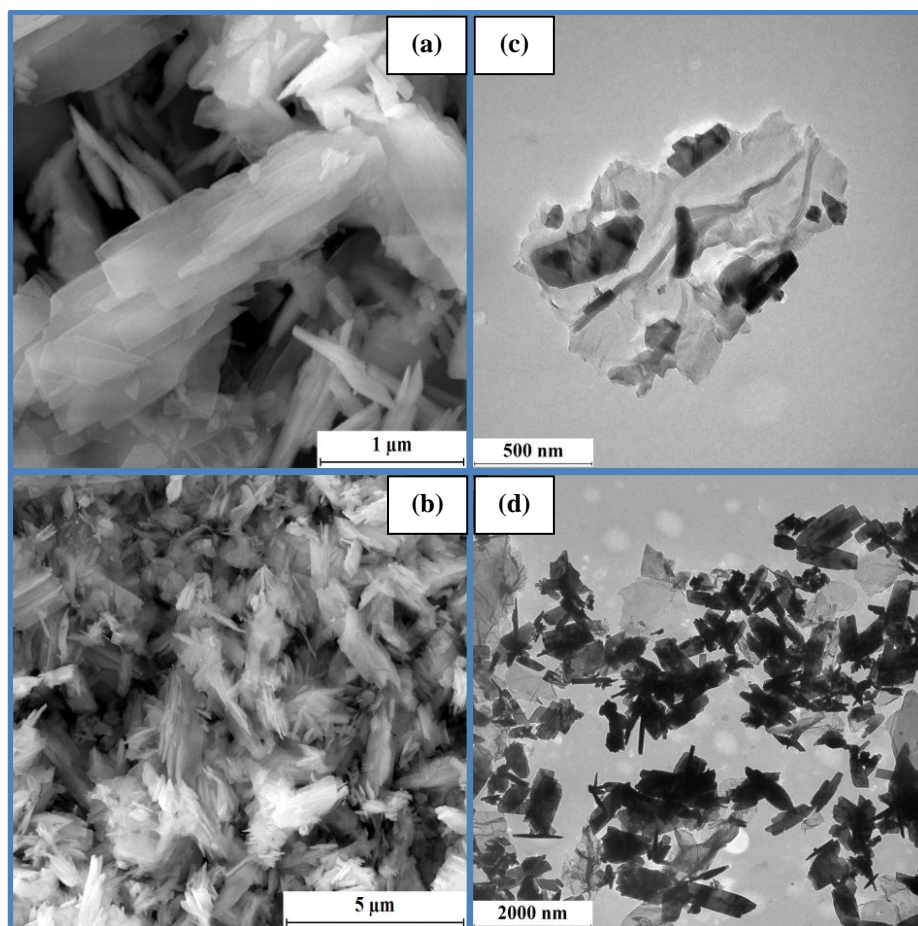


**Figure 4.29:** (a,b) FESEM and (c,d) TEM images of 2 mg FG/CuO nanocomposite.

When the concentration of FGO is increased to 20 mg, spherical CuO particles, with an average size of 500 nm, assembled on the translucent FG sheets (**Figure 4.30 (a and b)**). It is clearly shown that the particles are attached on both sides of the FG sheets, indicating that the functionalization of GO had occurred on the basal planes of the sheets. Based on the TEM images (**Figure 4.30 (c and d)**), we could also see a few nanoparticles reside outside of the support suggesting the moderate coupling interaction between CuO nanoparticles and FG sheets. Moreover, the formation of thin FG sheets had been evidenced by the transparent properties showing in both FESEM and TEM images.

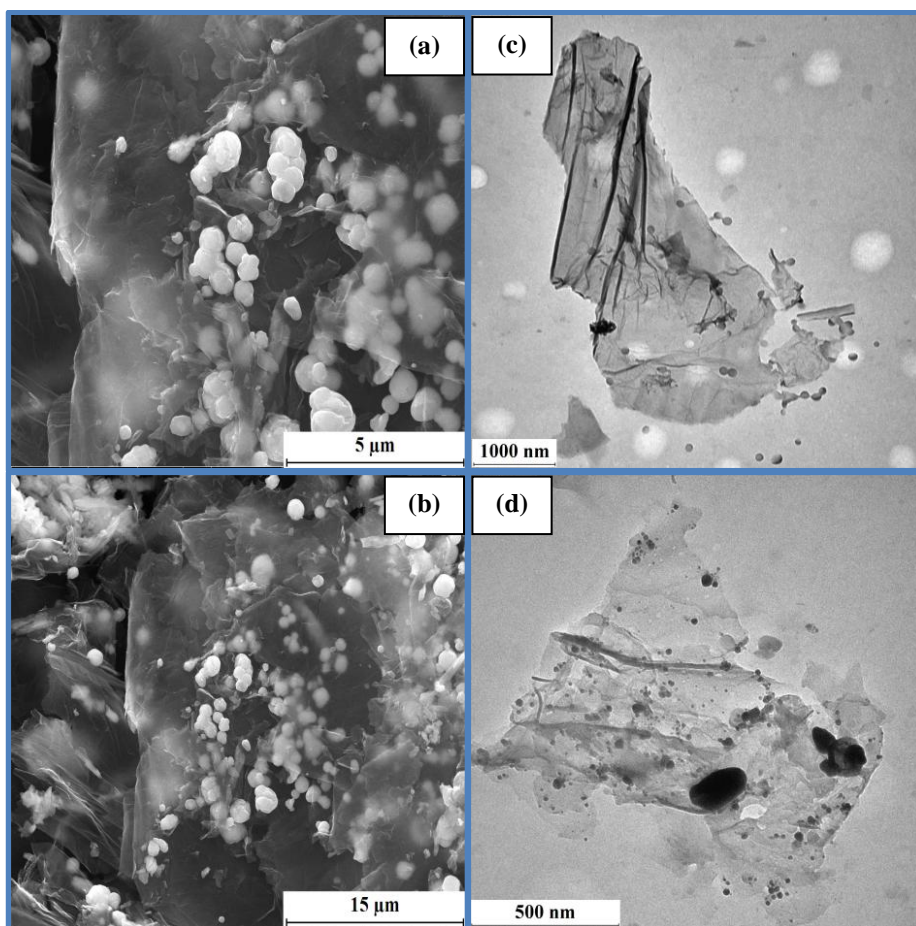


**Figure 4.30:** (a,b) FESEM and (c,d) TEM images of 20 mg FG/CuO nanocomposite.

A further increased with the concentration of FGO resulted in less agglomeration of particles, and reduced average particle size of 200 nm as characterized by FESEM shown in **Figure 4.31 (a and b)**. The CuO nanoparticles coated on FG sheets could be controlled by using a different mass ratio of FG and CuO. These images further proved the formation of CuO nanoparticles decorated FG sheets and further showing the intimate contact between CuO and FG. The TEM images of these nanocomposite are shown in **Figure 4.31 (c and d)**, where a large amount of spherical CuO nanoparticles was uniformly supported on FG sheets with less aggregation. This is because even though the concentration of FGO increased, the concentration of  $\text{Cu}^{2+}$  ions remain the same. Hence, this allows the same amount of

$\text{Cu}^{2+}$  ions to accommodate more nucleation sites on the FGO sheets, simultaneously hindering the agglomeration of nanoparticles.

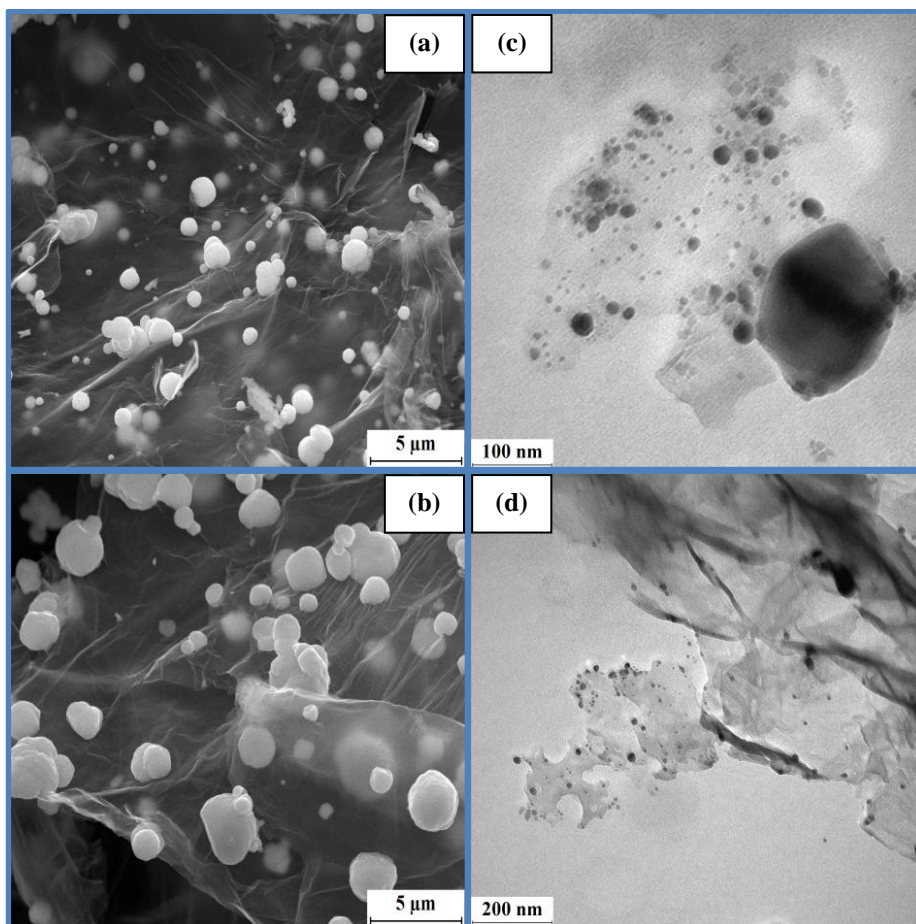


**Figure 4.31:** (a,b) FESEM and (c,d) TEM images of 30 mg FG/CuO nanocomposite.

A more careful and close-up view on the TEM images of rGO/CuO, 2 mg FG/CuO, 20 mg FG/CuO and 30 mg FG/CuO nanocomposites reveal that the average size of CuO nanoparticles is larger than 20 nm, almost 20 nm in diameter, 15 nm and less than 15 nm, respectively. These results are not in a good agreement with the measuring size based on FESEM results. We hypothesized that when we dispersed the samples in the ethanol, the bigger particles would wipe out thus leave only the smallest particles on the substrate. For the FESEM characterization, we tested the samples in the

powder form, therefore we proposed that the small particles had shielded by the bigger particles leading to the bigger particle sizes captured by FESEM.

#### 4.4.3 Formation mechanism of the nanocomposite

At first, GO dispersed in DIW became negatively charged due to the presence of more hydroxyl and carboxyl groups. Next, positively charged  $\text{Cu}^{2+}$  ions would mix with negatively charged GO in the presence of NaOH. By adding the NaOH into the mixture, a more negative charge would form on the surface of GO thus helped higher attachment of  $\text{Cu}^{2+}$  ions on GO surfaces which then served as a nucleation precursor. These attractions were induced by the electrostatic interaction. The process continued with the growth of CuO nanoparticles on the two-dimensional graphene nanosheets during the hydrothermal process. Upon the hydrothermal treatment,  $\text{Cu}^{2+}$  ions and GO would reduce to CuO and rGO, respectively due to the higher temperature which assist the hydrolysis process to occur.

The preparation of FGO and the adherence of CuO on the FG sheets are shown schematically in **Figure 4.32**. In general, GO contains abundant oxygen-containing functional groups on the surface, with the epoxy and C-OH functional groups attached above and below each carbon layer (the basal planes) and the -COOH groups linked to the edges of the basal planes (*Hu et al., 2011*). These functional groups provide feasibility for reactions with trialkoxy groups of silane to form silane linkages. After functionalization of GO, FGO surface contains a large amount of negatively charged functional carboxyl groups. The positively charged  $\text{Cu}^{2+}$  ions were attracted to the negatively charged FGO and deposited on the surface of FGO through electrostatic interaction. The hydrothermal condition reduced both the  $\text{Cu}^{2+}$  ions and FGO to CuO and FG, concurrently, without affecting functional carbonyl groups. Thus, the CuO

nanoparticles were expected to adsorb strongly on the FG surface even after hydrothermal reduction.

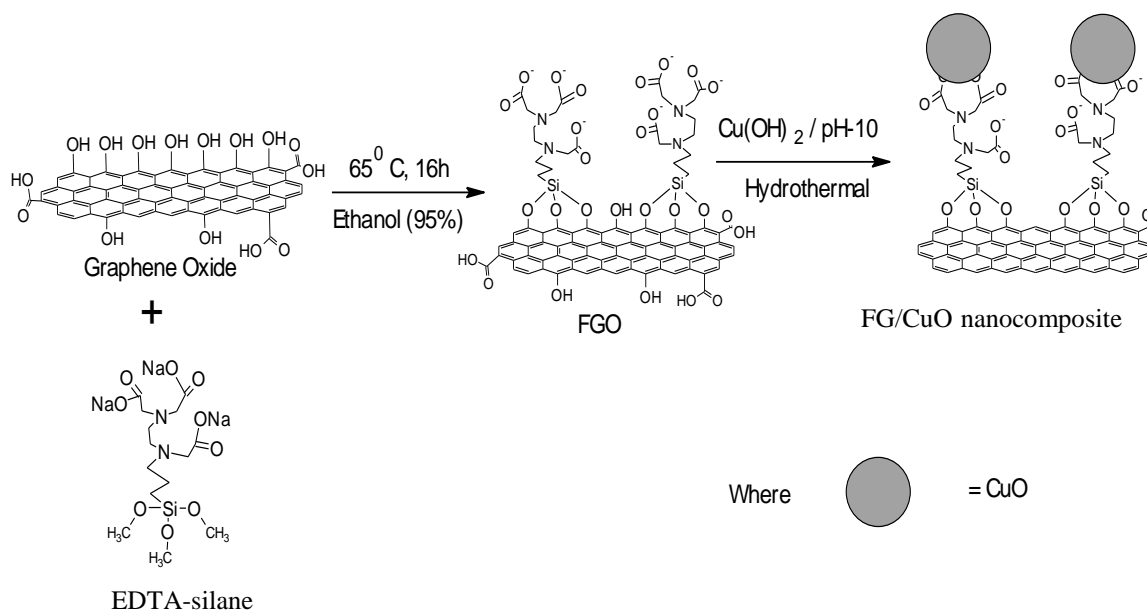


**Figure 4.32:** Formation of FG/CuO nanocomposite by hydrothermal method.

#### 4.4.4 Catalytic activity of rGO/CuO and FG/CuO nanocomposites

The catalytic activities of FG/CuO nanocomposites, examined by the degradation of MB in the presence of  $\text{H}_2\text{O}_2$  using UV-vis spectroscopy, are shown in **Figure 4.33**. Clearly, the intensity of the absorption peaks of MB at 665 nm decreases with respect to the reaction time for all the samples. During the 10 hours of reaction time, the blue color of MB solution gradually becomes less intense compared to the original solution suggesting that MB molecules has successfully decomposed from the aqueous solution. It further indicates that a strong oxidation of MB has occurred in the presence of rGO/CuO and FG/CuO nanocomposites.

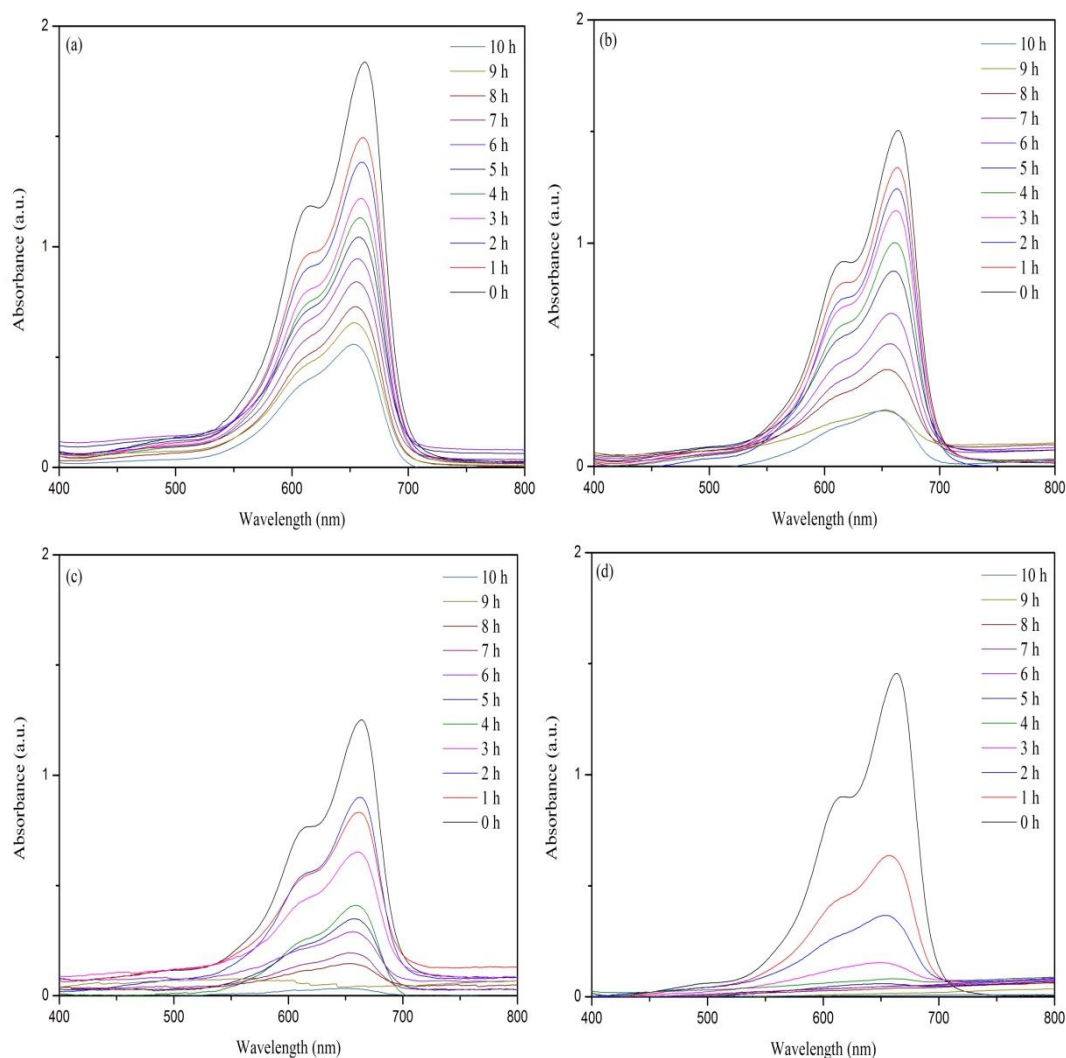


**Figure 4.33:** UV-vis absorption spectra of an aqueous solution of MB and  $\text{H}_2\text{O}_2$  in the presence of (a) rGO/CuO, (b) 2 mg FG/CuO, (c) 20 mg FG/CuO and (d) 30 mg FG/CuO nanocomposites at different reaction times.

**Figure 4.34** displays the single plot of degradation versus reaction time that is being translated from the UV profiles of the FG and nanocomposites on the degradation of MB. MB almost unaffected by  $\text{H}_2\text{O}_2$  alone and only 5.12 % of degradation are detected. The addition of FG and  $\text{H}_2\text{O}_2$  increases the degradation to 39.38 % after 10 hours, and increase to 61.11 % for CuO. It is worth noting that the slight enhancement in degradation of MB in the presence of CuO or FG is due to the catalytic oxidation of MB by CuO and adsorption of MB by FG, respectively (*Liu et al., 2012*). The degradation of MB is enhanced in the presence of rGO/CuO and FG/CuO

nanocomposites. The catalytic activity of the nanocomposites ascends in the following order: rGO/CuO (74.80 %) < 2 mg FG/CuO (87.50 %) < 20 mg FG/CuO (95.08 %) < 30 mg FG/CuO (99.06 %). According to the previous report, the fast absorption of MB by  $\pi$ - $\pi$  stacking interactions between MB and the  $\pi$  conjugation system of graphene/CuO nanocomposite may lead to its high catalytic activity (*Liu et al., 2012*).

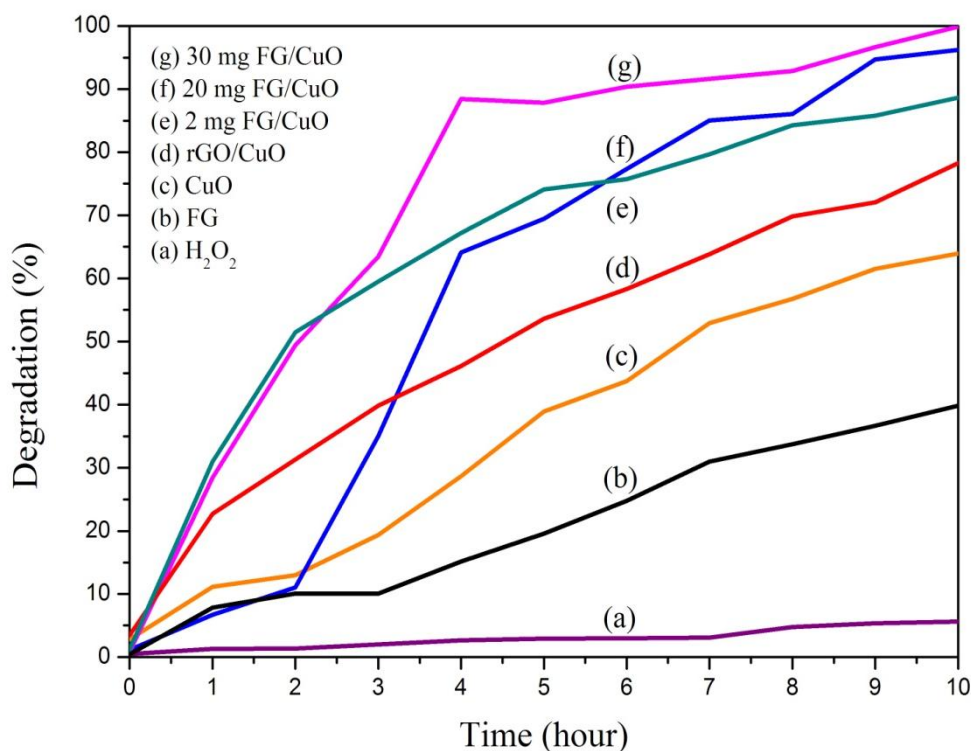


**Figure 4.34:** Time profile of MB degradation with the presence of nanocomposites.

For the sample prepared with 30 mg of FG, the degradation of MB reached 90% within 4 h, and achieved 99.06 % in 10 hours. This result suggests that the large surface of FG sheets plays an important role in the absorption of MB on the FG surface, whereupon it is degraded by CuO particles. This also indicates the intimate contact between CuO and FG, which is important for electronic interaction and interelectron transfer at the interface (*Xu et al., 2011*). Furthermore, the catalytic activity is dependent on the size of CuO particles and the FGO content. The smaller size of CuO

particles will also help to enhance the degradation of methylene blue due to the higher surface area. Therefore, we could conclude that the 30 mg FG/CuO nanocomposite with the smallest particle size and the strong interaction between the two materials exhibit the most excellent performance for degradation of MB compared to the others nanocomposites.

**Figure 4.35** illustrates the possible mechanism for the catalytic activity of FG/CuO nanocomposite with the presence of  $\text{H}_2\text{O}_2$ . This mechanism involves several steps where firstly MB and  $\text{H}_2\text{O}_2$  are absorbed on the surface of the FG due to the large surface area and numerous oxygenic groups that increase the adsorption ability of FG. The larger the surface area of FG so the more CuO particles that can be absorbed. Next,  $\text{H}_2\text{O}_2$  is decomposed into free radical species, such as  $\text{HO}\cdot$ ,  $\text{HOO}\cdot$  or  $\text{O}_2\cdot^-$  induced by the presence of CuO particles while MB is excited to  $\text{MB}\cdot$ . These free radical species have a powerful oxidative ability and cause destructive oxidation of the organic dye so the  $\text{MB}^+\cdot$  radical will degraded by the formed reactive oxidation species into  $\text{CO}_2$ ,  $\text{H}_2\text{O}$  and other mineralization (Li et al., 2012). The strong interaction and formation of a new oxygen bond between Cu particles and FG will promote electron transfer between Cu and C and prevents the recombination of electron-hole pairs. This will contribute to the enhancement of catalytic performance (Ge et al., 2011).

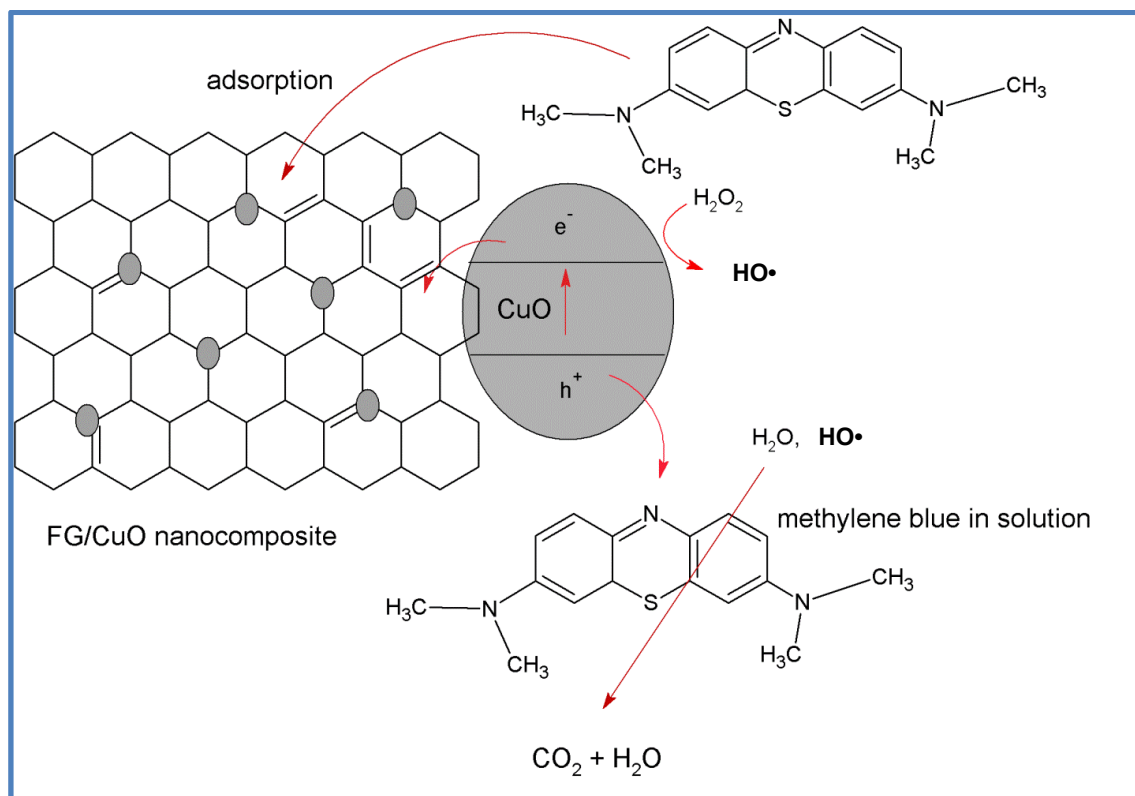


**Figure 4.35:** Purpose catalytic activity mechanism for degradation of MB over FG/CuO nanocomposite.

## Chapter 5 Conclusion

### 5.1 Conclusion

The overall goal of this research is to synthesize and characterize the properties of CuO, FG and its nanocomposites before further analyzing the relationship between its properties and catalytic activity. This goal is achieved through three steps which includes: 1) investigate the effect of synthesis approach on the CuO nanostructures and their catalytic performance 2) preparation of GO and FGO for study of their properties and 3) demonstrate the hydrothermal synthesis of FG/CuO and rGO/CuO nanocomposite for dye degradation. Each steps has its own specific set of objectives as mention in the earlier chapter.

In the first step, four synthesis methods were investigated for the fabrication of CuO nanostructures, namely reflux, hydrothermal, ultrasonication and two steps heating. These methods resulted in nanoflowers, nanorods and nanofibrils CuO that formed with various sizes, as observed under FESEM and TEM. Various morphologies due to the different operating conditions for growing the crystal such as heat, pressure and time required for growth. According to the XRD analysis, it can be conclude that higher reaction temperature will produce CuO nanostructures with a higher degree of crystallinity. The XRD analysis shows the intensity of the peaks are vary in the following order flower-like CuO < fibril-like CuO (two steps heating) < fibril-like CuO (ultrasonication) < rod-like CuO. The micro Raman measurement shows that similarity in morphology was reflected in the peak position of  $2B_g$  and the size of CuO also affected the intensity and shifted in position of peak  $2B_g$ . The catalytic activities of the CuO nanostructures were found to be directly correlated to the crystallinity of the CuO nanostructures. The hydrothermal method seems to be a feasible

method to produce scalable quantity of CuO nanorods and gives the best catalytic activity.

In the second step, the GO, FGO and FG had been synthesized and characterized in order to study and compare its properties. Based on the FESEM and TEM results, we can conclude that GO was formed from an overlapping of a few graphene layers with the cloudy-like structure on its surfaces. Upon functionalization, GO sheets transform to a well sheet-like structure with a reduction in its thickness as its TEM images show almost transparent image and also increase in its surface area compared to GO. The further reduction process will lead to the formation of thin FG sheets. The FT-IR result provided indirect evidence for 1) the existence of EDTA methylene groups in FGO sheets as well as the C-N bonds, 2) GO had partially reduced upon functionalization process when then further reduced by hydrothermal reaction, and 3) new reaction occurred between EDTA-silane and GO sheets and further react in the formation of FG, respectively. FT-IR analysis proved that the attachment of silane molecules on the GO sheets had occurred which then further reduced to form FG. Furthermore, TGA results also indicate that FG has the most thermally stable compared to GO and FGO. Among these three unique materials, FG shows the most excellent performance with the highest thermal stability, larger surface area with numerous amount as well as higher solubility in water and many solvents. Moreover, it is proven that with the presence of more oxygen functional groups on the surface, it gives the FGO sheets an advantage as a platform for the growth of nanoparticles.

In the third step, CuO nanoparticles had been successfully decorated on FG sheets using a simple hydrothermal technique. As for comparison, CuO nanoparticles encapsulated with rGO sheets was also being prepared using the similar procedure.

Unlike rGO/CuO nanocomposite that have lower solubility and hard to find the growth of CuO particles on its sheets, however, FG/CuO nanocomposite is observed to be easily dispersed in water by ultrasonication and the CuO nanoparticles are well distributed on the FG sheets as evidenced by the TEM and FESEM characterizations.

There are a few conclusions we can draw at this final stage. Firstly, FGO was proven to be the best anchoring side to decorate FGO with other organic or inorganic materials compared to GO due to the existence of abundant functional group on its surface. A simple and inexpensive method of fabricating FG/CuO nanocomposite via a hydrothermal process was carried out successfully. Next, the size of the CuO nanoparticles, anchored on the surface of FG sheets, could be tuned by controlling the amount of FGO used. FG decorated with CuO nanocomposite are most thermal-stable compared to rGO/CuO nanocomposite and FG itself. This experiment proves that the particles size, and the electronic interaction between the particles and FG sheets, plays an important role in catalysis where the 30 mg FG/CuO nanocomposite samples shows the best performance in catalytic activity.

## **5.2 Suggestions for future works**

Graphene or FG hybridized metal oxide demonstrates not only excellent properties but also show considerable promising as a candidate for wide field of application. It is believed that phenomena of graphene/functionalized graphene-based nanocomposite will keep growing up as there are a lot of new and interesting problems and stuffs needs to be solved and required further investigation. These become the driving force for researchers to keep on putting hundred percent afford toward this attractive material.

For future work, we also expect that this procedure of preparing CuO/FG nanocomposites could be extended to synthesize functionalized graphene decorated with other metal oxides. Thus to confirm the truth of this expectation, FG hybridized with other metal oxides can be fabricated by repeating the same procedure except by replacing CuO with other metal oxides such as ZnO, NiO, Fe<sub>3</sub>O<sub>2</sub> and etc. Besides that, this method also can be tested to synthesize FG complex oxide nanocomposite such as FG-CuFe<sub>2</sub>O<sub>4</sub>.

This FG-complex oxide system is worth to study as the combination of few materials, which also believed to be able combined in its properties forming unique integrated properties which provide a potential for wide applications. In terms of catalytic activity, FG-CuFe<sub>2</sub>O<sub>4</sub> nanocomposite have a great advantage as it possesses magnetic properties which important for repeated magnetic separation purposes. Moreover, their individual and integrated properties maybe could enhance the catalytic activity by generating stronger hydroxyl radicals and also the efficient separation of electrons and hole carrier in the FG-CuFe<sub>2</sub>O<sub>4</sub> coupling system.

---

**References****A**

Alexander, M., Beamson, G., Blomfield, C., Leggett, G., & Duc, T. (2001). Interaction of carboxylic acids with the oxyhydroxide surface of aluminium: poly (acrylic acid), acetic acid and propionic acid on pseudoboehmite. *Journal of Electron Spectroscopy and Related Phenomena*, 121(1), 19-32.

Ando, Y., & Zhao, X. (2006). Synthesis of carbon nanotubes by arc-discharge method. *New Diamond and Frontier Carbon Technology*, 16(3), 123-138.

**B**

Baby, T. T., & Sundara, R. (2011). Synthesis and transport properties of metal oxide decorated graphene dispersed nanofluids. *The Journal of Physical Chemistry C*, 115(17), 8527-8533.

Bakry, R., Vallant, R. M., Najam-ul-Haq, M., Rainer, M., Szabo, Z., Huck, C. W., & Bonn, G. K. (2007). Medicinal applications of fullerenes. *International journal of nanomedicine*, 2(4), 639.

Batchelor-McAuley, C., Du, Y., Wildgoose, G. G., & Compton, R. G. (2008). The use of copper(II) oxide nanorod bundles for the non-enzymatic voltammetric sensing of carbohydrates and hydrogen peroxide. *Sensors and Actuators B: Chemical*, 135(1), 230-235.

Bautista, C., & Mendoza, D. (2011). Multilayer Graphene Synthesized by CVD Using Liquid Hexane as the Carbon Precursor. *arXiv preprint arXiv:1109.1318*.

Becerril, H. A., Mao, J., Liu, Z., Stoltenberg, R. M., Bao, Z., & Chen, Y. (2008). Evaluation of Solution-Processed Reduced Graphene Oxide Films as Transparent Conductors. *ACS Nano*, 2(3), 463-470.

Bekyarova, E., Itkis, M. E., Ramesh, P., Berger, C., Sprinkle, M., de Heer, W. A., & Haddon, R. C. (2009). Chemical Modification of Epitaxial Graphene: Spontaneous Grafting of Aryl Groups. *Journal of the American Chemical Society*, 131(4), 1336-1337.

Bolotin, K. I., Sikes, K. J., Jiang, Z., Klima, M., Fudenberg, G., Hone, J., Kim, P., & Stormer, H. L. (2008). Ultrahigh electron mobility in suspended graphene. *Solid State Communications*, 146(9-10), 351-355.

Britnell, L., Gorbachev, R. V., Jalil, R., Belle, B. D., Schedin, F., Mishchenko, A., Georgiou, T., Katsnelson, M. I., Eaves, L., & Morozov, S. V. (2012). Field-Effect Tunneling Transistor Based on Vertical Graphene Heterostructures. *Science*, 335(6071), 947-950.

Brodie, B. C. (1859). On the Atomic Weight of Graphite. *Philosophical Transactions of the Royal Society of London*, 149, 249-259.

## C

- Cai, D., & Song, M. (2007). Preparation of fully exfoliated graphite oxide nanoplatelets in organic solvents. *Journal of Materials Chemistry*, *17*(35), 3678-3680.
- Cao, F., & Gong, J. (2012). Nonenzymatic glucose sensor based on CuO microfibers composed of CuO nanoparticles. *Analytica chimica acta*.
- Cao, M., Hu, C., Wang, Y., Guo, Y., Guo, C., & Wang, E. (2003). A controllable synthetic route to Cu, Cu<sub>2</sub>O, and CuO nanotubes and nanorods. *Chemical Communications*(15), 1884-1885.
- Carnes, C. L., Stipp, J., Klabunde, K. J., & Bonevich, J. (2002). Synthesis, Characterization, and Adsorption Studies of Nanocrystalline Copper Oxide and Nickel Oxide. *Langmuir*, *18*(4), 1352-1359.
- Carotenuto, G., & Nicolais, L. (2012). Graphene–Polymer Composites. *Wiley Encyclopedia of Composites*.
- Chandra, V., Park, J., Chun, Y., Lee, J. W., Hwang, I.-C., & Kim, K. S. (2010). Water-Dispersible Magnetite-Reduced Graphene Oxide Composites for Arsenic Removal. *ACS Nano*, *4*(7), 3979-3986.
- Che, G., Lakshmi, B., Martin, C., Fisher, E., & Ruoff, R. S. (1998). Chemical vapor deposition based synthesis of carbon nanotubes and nanofibers using a template method. *Chemistry of Materials*, *10*(1), 260-267.
- Chen, L., Lu, N., Xu, C., Yu, H., & Wang, T. (2009). Electrochemical performance of polycrystalline CuO nanowires as anode material for Li ion batteries. *Electrochimica Acta*, *54*(17), 4198-4201.
- Chen, L., Xu, Z., Li, J., Min, C., Liu, L., Song, X., Chen, G., & Meng, X. (2011). Reduction and disorder in graphene oxide induced by electron-beam irradiation. *Materials Letters*, *65*(8), 1229-1230.
- Chen, S., Zhu, J., Huang, H., Zeng, G., Nie, F., & Wang, X. (2010). Facile solvothermal synthesis of graphene–MnOOH nanocomposites. *Journal of Solid State Chemistry*, *183*(11), 2552-2557.
- Chen, W., Yan, L., & Bangal, P. R. (2010). Preparation of graphene by the rapid and mild thermal reduction of graphene oxide induced by microwaves. *Carbon*, *48*(4), 1146-1152.
- Cheng, M., Yang, R., Zhang, L., Shi, Z., Yang, W., Wang, D., Xie, G., Shi, D., & Zhang, G. (2012). Restoration of graphene from graphene oxide by defect repair. *Carbon*.
- Cho, S., Jang, J.-W., Jung, S.-H., Lee, B. R., Oh, E., & Lee, K.-H. (2009). Precursor Effects of Citric Acid and Citrates on ZnO Crystal Formation. *Langmuir*, *25*(6), 3825-3831.

Choi, B. G., Park, H. S., Yang, M. H., Jung, Y. M., Lee, S. Y., Hong, W. H., & Park, T. J. (2010). Microwave-assisted synthesis of highly water-soluble graphene towards electrical DNA sensor. *Nanoscale*, *2*(12), 2692-2697.

Cölfen, H., & Mann, S. (2003). Higher-Order Organization by Mesoscale Self-Assembly and Transformation of Hybrid Nanostructures. *Angewandte Chemie International Edition*, *42*(21), 2350-2365.

Cuong, T. V., Pham, V. H., Tran, Q. T., Chung, J. S., Shin, E. W., Kim, J. S., & Kim, E. J. (2010). Optoelectronic properties of graphene thin films prepared by thermal reduction of graphene oxide. *Materials Letters*, *64*(6), 765-767.

## D

Darvish, D. S., & Atwater, H. A. (2009). *Modeling, synthesis, and characterization of thin film Copper Oxide for solar cells*. Paper presented at the Photovoltaic Specialists Conference (PVSC), 2009 34th IEEE.

De Palma, R., Peeters, S., Van Bael, M. J., Van den Rul, H., Bonroy, K., Laureyn, W., Mullens, J., Borghs, G., & Maes, G. (2007). Silane ligand exchange to make hydrophobic superparamagnetic nanoparticles water-dispersible. *Chemistry of Materials*, *19*(7), 1821-1831.

Dong, L., Gari, R. R. S., Li, Z., Craig, M. M., & Hou, S. (2010). Graphene-supported platinum and platinum–ruthenium nanoparticles with high electrocatalytic activity for methanol and ethanol oxidation. *Carbon*, *48*(3), 781-787.

Du, Q., Zheng, M., Zhang, L., Wang, Y., Chen, J., Xue, L., Dai, W., Ji, G., & Cao, J. (2010). Preparation of functionalized graphene sheets by a low-temperature thermal exfoliation approach and their electrochemical supercapacitive behaviors. *Electrochimica Acta*, *55*(12), 3897-3903.

## E

Eigler, S., Dotzer, C., Hirsch, A., Enzelberger, M., & Müller, P. (2012). Formation and Decomposition of CO<sub>2</sub> Intercalated Graphene Oxide. *Chemistry of Materials*, *24*(7), 1276-1282.

Erdoğan, İ. Y., & Güllü, Ö. (2010). Optical and structural properties of CuO nanofilm: Its diode application. *Journal of Alloys and Compounds*, *492*(1), 378-383.

Ethiraj, A. S., & Kang, D. J. (2012). Synthesis and characterization of CuO nanowires by a simple wet chemical method. *Nanoscale research letters*, *7*(1), 70.

## F

Fan, W., Lai, Q., Zhang, Q., & Wang, Y. (2011). Nanocomposites of TiO<sub>2</sub> and reduced graphene oxide as efficient photocatalysts for hydrogen evolution. *The Journal of Physical Chemistry C*, *115*(21), 10694-10701.

Feng, C., Zhang, C., Zhang, R., Frauenheim, T., & Van Hove, M. A. (2008). Mechanical properties of solid C<sub>60</sub> studied with density functional tight binding method augmented by an empirical dispersion term. *Journal of Physics: Condensed Matter*, *20*(27), 275240.

- Fernandez-Merino, M., Guardia, L., Paredes, J., Villar-Rodil, S., Solis-Fernandez, P., Martinez-Alonso, A., & Tascon, J. (2010). Vitamin C is an ideal substitute for hydrazine in the reduction of graphene oxide suspensions. *The Journal of Physical Chemistry C*, *114*(14), 6426-6432.
- Ferrari, A., Meyer, J., Scardaci, V., Casiraghi, C., Lazzeri, M., Mauri, F., Piscanec, S., Jiang, D., Novoselov, K. S., & Roth, S. (2006). Raman spectrum of graphene and graphene layers. *Physical Review Letters*, *97*(18), 187401.
- Ferrari, A., & Robertson, J. (2001). Resonant Raman spectroscopy of disordered, amorphous, and diamondlike carbon. *Physical Review B*, *64*(7), 075414.
- Filipič, G., & Cvelbar, U. (2012). Copper oxide nanowires: a review of growth. *Nanotechnology*, *23*(19), 194001.
- Fuentes, S., Zarate, R. A., Munoz, P., & Diaz-droguett, D. E. (2010). Formation of hierarchical CCuO nanowires on a copper surface via a room-temperature solution-immersion process. *Journal of the Chilean Chemical Society*, *55*, 147-149.
- ## G
- Gao, X., Bao, J., Pan, G., Zhu, H., Huang, P., Wu, F., & Song, D. (2004). Preparation and electrochemical performance of polycrystalline and single crystalline CuO nanorods as anode materials for Li ion battery. *The Journal of Physical Chemistry B*, *108*(18), 5547-5551.
- Ge, L., Han, C., Liu, J., & Li, Y. (2011). Enhanced Visible Light Photocatalytic Activity of Novel Polymeric g/C<sub>3</sub>N<sub>4</sub> Loaded with Ag Nanoparticles. *Applied Catalysis A: General*.
- Geim, A. K., & Novoselov, K. S. (2007). The rise of graphene. *Nat Mater*, *6*(3), 183-191.
- Geng, J., Liu, L., Yang, S. B., Youn, S. C., Kim, D. W., Lee, J. S., Choi, J. K., & Jung, H. T. (2010). A Simple Approach for Preparing Transparent Conductive Graphene Films Using the Controlled Chemical Reduction of Exfoliated Graphene Oxide in an Aqueous Suspension. *The Journal of Physical Chemistry C*, *114*(34), 14433-14440.
- Georgakilas, V., Otyepka, M., Bourlinos, A. B., Chandra, V., Kim, N., Kemp, K. C., Hobza, P., Zboril, R., & Kim, K. S. (2012). Functionalization of Graphene: Covalent and Non-Covalent Approaches, Derivatives and Applications. *Chemical Reviews*.
- ## H
- Hong, Z., Cao, Y., & Deng, J. (2002). A convenient alcoholothermal approach for low temperature synthesis of CuO nanoparticles. *Materials letters*, *52*(1), 34-38.

- Hou, H., Zhu, Y., Tang, G., & Hu, Q. (2012). Lamellar  $\gamma$ -AlOOH architectures: Synthesis and application for the removal of HCN. *Materials Characterization*, 68, 33-41.
- Hou, S., Su, S., Kasner, M. L., Shah, P., Patel, K., & Madarang, C. J. (2010). Formation of highly stable dispersions of silane-functionalized reduced graphene oxide. *Chemical Physics Letters*, 501(1), 68-74.
- Hu, H., Wang, X., Wang, J., Liu, F., Zhang, M., & Xu, C. (2011). Microwave-assisted covalent modification of graphene nanosheets with chitosan and its electrorheological characteristics. *Applied Surface Science*, 257(7), 2637-2642.
- Huang, Y., Yan, W., Xu, Y., Huang, L., & Chen, Y. (2012). Functionalization of Graphene Oxide by Two-Step Alkylation. *Macromolecular Chemistry and Physics*.
- Huh, S. H. (2011). Thermal reduction of graphene oxide (Vol. 5): chapter.
- Hummers Jr, W. S., & Offeman, R. E. (1958). Preparation of graphitic oxide. *Journal of the American Chemical Society*, 80(6), 1339-1339.
- I**
- Iijima, S. (1991). Helical microtubules of graphitic carbon. *nature*, 354(6348), 56-58.
- Iijima, S., & Ichihashi, T. (1993). Single-shell carbon nanotubes of 1-nm diameter.
- J**
- Jeong, H., Jin, M., So, K., Lim, S., & Lee, Y. (2009). Tailoring the characteristics of graphite oxides by different oxidation times. *Journal of Physics D: Applied Physics*, 42(6), 065418.
- Ji, Z., Wu, J., Shen, X., Zhou, H., & Xi, H. (2011). Preparation and characterization of graphene/NiO nanocomposites. *Journal of Materials Science*, 46(5), 1190-1195.
- Jia, X., Fan, H., & Yang, W. (2010). Hydrothermal Synthesis and Primary Gas Sensing Properties of CuO Nanosheets. *Journal of Dispersion Science and Technology*, 31(7), 866-869.
- Jiang, J.-W., Wang, J.-S., & Li, B. (2009). Young's modulus of graphene: A molecular dynamics study. *Physical Review B*, 80(11), 113405.
- Jiang, X., Herricks, T., & Xia, Y. (2002). CuO nanowires can be synthesized by heating copper substrates in air. *Nano Letters*, 2(12), 1333-1338.
- Jisen, W., Jinkai, Y., Jinquan, S., & Ying, B. (2004). Synthesis of copper oxide nanomaterials and the growth mechanism of copper oxide nanorods. *Materials & design*, 25(7), 625-629.
- Ju, H. M., Huh, S. H., Choi, S. H., & Lee, H. L. (2010). Structures of thermally and chemically reduced graphene. *Materials Letters*, 64(3), 357-360.

**K**

- Karthika, P., Rajalakshmi, N., & Dhathathreyan, K. S. (2012). Functionalized Exfoliated Graphene Oxide as Supercapacitor Electrodes. *Soft Nanoscience Letters*, 2(4), 59-66.
- Katsnelson, M. I. (2007). Graphene: carbon in two dimensions. *Materials Today*, 10(1–2), 20-27.
- Khanra, P., Kuila, T., Kim, N. H., Bae, S. H., Yu, D.-s., & Lee, J. H. (2012). Simultaneous bio-functionalization and reduction of graphene oxide by baker's yeast. *Chemical Engineering Journal*, 183(0), 526-533.
- Kim, D. H., Ryu, H. W., Moon, J. H., & Kim, J. (2006). Effect of ultrasonic treatment and temperature on nanocrystalline TiO<sub>2</sub>. *Journal of Power Sources*, 163(1), 196-200.
- Krätschmer, W., Lamb, L. D., Fostiropoulos, K., & Huffman, D. R. (1990). C 60: a new form of carbon. *Nature*, 347(6291), 354-358.
- Kroto, H. W., Heath, J. R., O'Brien, S. C., Curl, R. F., & Smalley, R. E. (1985). C 60: buckminsterfullerene. *Nature*, 318(6042), 162-163.
- Kudin, K. N., Ozbas, B., Schniepp, H. C., Prud'Homme, R. K., Aksay, I. A., & Car, R. (2008). Raman spectra of graphite oxide and functionalized graphene sheets. *Nano letters*, 8(1), 36-41.

**L**

- Li, B., Cao, H., Shao, J., Qu, M., & Warner, J. H. (2011). Superparamagnetic Fe<sub>3</sub>O<sub>4</sub> nanocrystals@graphene composites for energy storage devices. *Journal of Materials Chemistry*, 21(13), 5069-5075.
- Li, B., Liu, T., Wang, Y., & Wang, Z. (2012). ZnO/graphene-oxide nanocomposite with remarkably enhanced visible-light-driven photocatalytic performance. *Journal of colloid and interface science*.
- Li, C. C., & Chang, M. H. (2004). Colloidal stability of CuO nanoparticles in alkanes via oleate modifications. *Materials Letters*, 58(30), 3903-3907.
- Li, D., Müller, M. B., Gilje, S., Kaner, R. B., & Wallace, G. G. (2008). Processable aqueous dispersions of graphene nanosheets. *Nature Nanotechnology*, 3(2), 101-105.
- Lian, P., Zhu, X., Xiang, H., Li, Z., Yang, W., & Wang, H. (2010). Enhanced cycling performance of Fe<sub>3</sub>O<sub>4</sub>-graphene nanocomposite as an anode material for lithium-ion batteries. *Electrochimica Acta*, 56(2), 834-840.
- Liao, L., Zhang, Z., Yan, B., Zheng, Z., Bao, Q., Wu, T., Li, C. M., Shen, Z. X., Zhang, J. X., & Gong, H. (2009). Multifunctional CuO nanowire devices: p-type field effect transistors and CO gas sensors. *Nanotechnology*, 20(8), 085203.

- Lim, H. N., Nurzulaikha, R., Harrison, I., Lim, S. S., Tan, W. T., Yeo, M. C., Yarmo, M. A., & Huang, N. M. (2012). Preparation and characterization of tin oxide, SnO<sub>2</sub> nanoparticles decorated graphene. *Ceramics International*, 38(5), 4209-4216.
- Liu, S., Tian, J., Wang, L., Luo, Y., & Sun, X. (2012). One-pot synthesis of CuO nanoflower-decorated reduced graphene oxide and its application to photocatalytic degradation of dyes. *Catalysis Science & Technology*, 2(2), 339-344.
- Liu, X., Geng, B., Du, Q., Ma, J., & Liu, X. (2007). Temperature-controlled self-assembled synthesis of CuO, Cu<sub>2</sub>O and Cu nanoparticles through a single-precursor route. *Materials Science and Engineering: A*, 448(1), 7-14.
- Liu, Y., Xie, B., Zhang, Z., Zheng, Q., & Xu, Z. (2012). Mechanical properties of graphene papers. *Journal of the Mechanics and Physics of Solids*.
- Lu, C., Qi, L., Yang, J., Zhang, D., Wu, N., & Ma, J. (2004). Simple template-free solution route for the controlled synthesis of Cu (OH)<sub>2</sub> and CuO nanostructures. *The Journal of Physical Chemistry B*, 108(46), 17825-17831.
- Lu, L. Q., & Wang, Y. (2011). Sheet-like and fusiform CuO nanostructures grown on graphene by rapid microwave heating for high Li-ion storage capacities. *Journal of Materials Chemistry*, 21(44), 17916-17921.
- Lu, T., Pan, L., Li, H., Zhu, G., Lv, T., Liu, X., Sun, Z., Chen, T., & Chua, D. H. C. (2011). Microwave-assisted synthesis of graphene-ZnO nanocomposite for electrochemical supercapacitors. *Journal of Alloys and Compounds*, 509(18), 5488-5492.
- Luo, D., Zhang, G., Liu, J., & Sun, X. (2011). Evaluation criteria for reduced graphene oxide. *The Journal of Physical Chemistry C*, 115(23), 11327-11335.
- M**
- Mai, Y. J., Wang, X. L., Xiang, J. Y., Qiao, Y. Q., Zhang, D., Gu, C. D., & Tu, J. P. (2011). CuO/graphene composite as anode materials for lithium-ion batteries. *Electrochimica Acta*, 56(5), 2306-2311.
- Maji, S. K., Mukherjee, N., Mondal, A., Adhikary, B., & Karmakar, B. (2010). Chemical synthesis of mesoporous CuO from a single precursor: Structural, optical and electrical properties. *Journal of Solid State Chemistry*, 183(8), 1900-1904.
- Malesevic, A., Vitchev, R., Schouteden, K., Volodin, A., Zhang, L., Van Tendeloo, G., Vanhulsel, A., & Van Haesendonck, C. (2008). Synthesis of few-layer graphene via microwave plasma-enhanced chemical vapour deposition. *Nanotechnology*, 19(30), 305604.
- Manna, S., Das, K., & De, S. (2010). Template-free synthesis of mesoporous CuO dandelion structures for optoelectronic applications. *ACS Applied Materials & Interfaces*, 2(5), 1536-1542.

- Marcano, D. C., Kosynkin, D. V., Berlin, J. M., Sinitskii, A., Sun, Z., Slesarev, A., Alemany, L. B., Lu, W., & Tour, J. M. (2010). Improved synthesis of graphene oxide. *Acs Nano*, 4(8), 4806.
- Marlinda, A. R., Huang, N. M., Muhamad, M. R., An'amt, M. N., Chang, B. Y. S., Yusoff, N., Harrison, I., Lim, H. N., Chia, C. H., & Kumar, S. V. (2012). Highly efficient preparation of ZnO nanorods decorated reduced graphene oxide nanocomposites. *Materials Letters*, 80(0), 9-12.
- Marques, P., Gonçalves, G., Cruz, S., Almeida, N., Singh, M., Grácio, J., & Sousa, A. (2011). Functionalized Graphene Nanocomposites.
- McAllister, M. J., Li, J. L., Adamson, D. H., Schniepp, H. C., Abdala, A. A., Liu, J., Herrera-Alonso, M., Milius, D. L., Car. R., & Prud'homme, R. K. (2007). Single sheet functionalized graphene by oxidation and thermal expansion of graphite. *Chemistry of Materials*, 19(18), 4396-4404.
- Morozov, S. V., Novoselov, K. S., Katsnelson, M. I., Schedin, F., Elias, D. C., Jaszczak, J. A., & Geim, A. K. (2008). Giant Intrinsic Carrier Mobilities in Graphene and Its Bilayer. *Physical Review Letters*, 100(1), 016602.
- Mu, Y., Yang, J., Han, S., Hou, H., & Fan, Y. (2010). Syntheses and gas-sensing properties of CuO nanostructures by using [Cu(pbbt)Cl<sub>2</sub>]<sub>2</sub>·CH<sub>3</sub>OH as a precursor. *Materials Letters*, 64(11), 1287-1290.
- Muhamad, E. N., Irmawati, R., Abdullah, A. H., Taufiq-Yap, Y., & Hamid, S. B. A. (2007). Effect of number of washing on the characteristics of copper oxide nanopowders. *Malaysian Journal of Analytical Sciences*, 11(1), 294-301.
- N**
- Neri, G., Leonardi, S. G., Latino, M., Donato, N., Baek, S., Conte, D. E., Russo, P. A., & Pinna, N. (2012). Sensing behavior of SnO<sub>2</sub>/reduced graphene oxide nanocomposites toward NO<sub>2</sub>. *Sensors and Actuators B: Chemical*(0).
- Nguyen, H. B., Ngo, T. T. T., Nguyen, N. T., Dang, T. T. H., Do, P. Q., Nguyen, X. N., . . . Phan, N. M. (2012). Graphene patterned polyaniline-based biosensor for glucose detection. *Advances in Natural Sciences: Nanoscience and Nanotechnology*, 3(2), 025011.
- Novoselov, K., Geim, A., Morozov, S., Jiang, D., Zhang, Y., Dubonos, S., Grigorieva, I., & Firsov, A. (2004). Electric field effect in atomically thin carbon films. *Science*, 306(5696), 666-669.
- P**
- Pan, K., Ming, H., Yu, H., Liu, Y., Kang, Z., Zhang, H., & Lee, S.-T. (2011). Different copper oxide nanostructures: Synthesis, characterization, and application for C-N cross-coupling catalysis. *Crystal Research and Technology*, 46(11), 1167-1174.
- Pan, Q., Jin, H., Wang, H., & Yin, G. (2007). Flower-like CuO film-electrode for lithium ion batteries and the effect of surface morphology on electrochemical performance. *Electrochimica Acta*, 53(2), 951-956.

- Paredes, J., Villar-Rodil, S., Martinez-Alonso, A., & Tascon, J. (2008). Graphene oxide dispersions in organic solvents. *Langmuir*, 24(19), 10560-10564.
- Paula Marques, G. G., Sandra Cruz, Nuno Almeida, Manoj Singh, José Grácio and António Sousa. (2011). Functionalized Graphene Nanocomposites. In D. A. Hashim (Ed.), *Advances in Nanocomposite Technology*.
- Pei, S., & Cheng, H.-M. (2012). The reduction of graphene oxide. *Carbon*, 50(9), 3210-3228.
- Pham, V. H., Cuong, T. V., Hur, S. H., Oh, E., Kim, E. J., Shin, E. W., & Chung, J. S. (2010). Chemical functionalization of graphene sheets by solvothermal reduction of a graphene oxide suspension in N-methyl-2-pyrrolidone. *J. Mater. Chem.*, 21(10), 3371-3377.
- Pimenta, M., Dresselhaus, G., Dresselhaus, M. S., Jorio, A., & Saito, R. (2007). Studying disorder in graphite-based systems by Raman spectroscopy. *Physical Chemistry Chemical Physics*, 9(11), 1276-1290.
- Pranowo, H. D., & Rode, B. M. (2001). Preferential Cu<sup>2+</sup> solvation in aqueous ammonia solution of various concentrations. *Chemical Physics*, 263(1), 1-6.
- Psarras, G., Tantis, I., & Tasis, D. Functionalized graphene–poly (vinyl alcohol) nanocomposites: Physical and dielectric properties. *eXPRESS Polymer Letters*, 6.
- R**
- Ramanathan T, Abdala, A. A., Stankovich S, Dikin, D. A., Herrera Alonso, M., Piner, R. D., Adamson, D. H., Schniepp, H. C., Chen, X., & Brinson, L. C. (2008). Functionalized graphene sheets for polymer nanocomposites. *Nat Nano*, 3(6), 327-331.
- Rao, A., Eklund, P., Bandow, S., Thess, A., & Smalley, R. E. (1997). Evidence for charge transfer in doped carbon nanotube bundles from Raman scattering. *Nature*, 388(6639), 257-259.
- Reimann, K., & Syassen, K. (1989). Raman scattering and photoluminescence in Cu<sub>2</sub>O under hydrostatic pressure. *Physical Review B*, 39(15), 11113.
- S**
- Scarselli, M., Castrucci, P., & De Crescenzi, M. (2012). Electronic and optoelectronic nano-devices based on carbon nanotubes. *Journal of Physics: Condensed Matter*, 24(31), 313202.
- Scott, C., Arepalli, S., Nikolaev, P., & Smalley, R. (2001). Growth mechanisms for single-wall carbon nanotubes in a laser-ablation process. *Applied Physics A: Materials Science & Processing*, 72(5), 573-580.
- Shao, G., Lu, Y., Wu, F., Yang, C., Zeng, F., & Wu, Q. (2012). Graphene oxide: the mechanisms of oxidation and exfoliation. *Journal of Materials Science*, 1-10.

- Shen, J., Shi, M., Li, N., Yan, B., Ma, H., Hu, Y., & Ye, M. (2010). Facile synthesis and application of Ag-chemically converted graphene nanocomposite. *Nano Research*, 3(5), 339-349.
- Shen, J., Yan, B., Shi, M., Ma, H., Li, N., & Ye, M. (2011). One step hydrothermal synthesis of TiO<sub>2</sub>-reduced graphene oxide sheets. *J. Mater. Chem.*, 21(10), 3415-3421.
- Socrates, G., & Socrates, G. (1994). *Infrared characteristic group frequencies: tables and charts*: John Wiley & Sons New York.
- Sprinkle, M., Ruan, M., Hu, Y., Hankinson, J., Rubio-Roy, M., Zhang, B., Wu, X., Berger, C., & De Heer, W. (2010). Scalable templated growth of graphene nanoribbons on SiC. *Nature nanotechnology*, 5(10), 727-731.
- Srivastava, R., Prathap, M., & Kore, R. (2011). Morphologically controlled synthesis of copper oxides and their catalytic applications in the synthesis of propargylamine and oxidative degradation of methylene blue. *Colloids and Surfaces A: Physicochemical and Engineering Aspects*.
- Stankovich, S., Dikin, D. A., Piner, R. D., Kohlhaas, K. A., Kleinhammes, A., Jia, Y., Wu, Y., Nguyen, S. & Ruoff, R. S. (2007). Synthesis of graphene-based nanosheets via chemical reduction of exfoliated graphite oxide. *Carbon*, 45(7), 1558-1565.
- Stankovich, S., Piner, R. D., Nguyen, S. B. T., & Ruoff, R. S. (2006). Synthesis and exfoliation of isocyanate-treated graphene oxide nanoplatelets. *Carbon*, 44(15), 3342-3347.
- Su, C. Y., Xu, Y., Zhang, W., Zhao, J., Tang, X., Tsai, C. H., & Li, L. J. (2009). Electrical and spectroscopic characterizations of ultra-large reduced graphene oxide monolayers. *Chemistry of Materials*, 21(23), 5674-5680.
- Sun, H., Cao, L., & Lu, L. (2011). Magnetite/reduced graphene oxide nanocomposites: One step solvothermal synthesis and use as a novel platform for removal of dye pollutants. *Nano Research*, 4(6), 550-562.
- Suslick, K. S., Didenko, Y., Fang, M. M., Hyeon, T., Kolbeck, K. J., McNamara, W. B., . . . Didenko, Y. (1999). Acoustic cavitation and its chemical consequences. *Philosophical Transactions of the Royal Society of London. Series A: Mathematical, Physical and Engineering Sciences*, 357(1751), 335-353.
- T**
- Teng, F., Yao, W., Zheng, Y., Ma, Y., Teng, Y., Xu, T., Liang, S., & Zhu, Y. (2008). Synthesis of flower-like CuO nanostructures as a sensitive sensor for catalysis. *Sensors and Actuators B: Chemical*, 134(2), 761-768.
- Trass, A., ElShamy, H., El-Mehasseb, I., & El-Kemary, M. (2011). CuO nanoparticles: Synthesis, characterization, optical properties and interaction with amino acids. *Applied Surface Science*.

## V

- Veillard, H. (1977). Hydration of the cations  $Al^{3+}$  and  $Cu^{2+}$ . A theoretical study. *Journal of the American Chemical Society*, 99(22), 7194-7199.
- Vila, M., Díaz-Guerra, C., & Piqueras, J. (2010). Optical and magnetic properties of CuO nanowires grown by thermal oxidation. *Journal of Physics D: Applied Physics*, 43(13), 135403.
- Volanti, D., Keyson, D., Cavalcante, L., Simoes, A., Joya, M., Longo, E., Varela, J. A., Pizani, P. S., & Souza, A. (2008). Synthesis and characterization of CuO flower-nanostructure processing by a domestic hydrothermal microwave. *Journal of Alloys and Compounds*, 459(1), 537-542.

## W

- Wang, B., Wu, X.-L., Shu, C.-Y., Guo, Y.-G., & Wang, C.-R. (2010). Synthesis of CuO/graphene nanocomposite as a high-performance anode material for lithium-ion batteries. *Journal of Materials Chemistry*, 20(47), 10661-10664.
- Wang, D., Kou, R., Choi, D., Yang, Z., Nie, Z., Li, J., Saraf, L. V., Hu, D., Zhang, J., & Graff, G. L. (2010). Ternary Self-Assembly of Ordered Metal Oxide–Graphene Nanocomposites for Electrochemical Energy Storage. *ACS Nano*, 4(3), 1587-1595.
- Wang, H., & Hu, Y. H. (2011). Effect of oxygen content on structures of graphite oxides. *Industrial & Engineering Chemistry Research*, 50(10), 6132-6137.
- Wang, H., Robinson, J. T., Li, X., & Dai, H. (2009). Solvothermal reduction of chemically exfoliated graphene sheets. *Journal of the American Chemical Society*, 131(29), 9910-9911.
- Wang, J., He, S., Li, Z., Jing, X., & Zhang, M. (2009). Synthesis of claw-like CuO and its catalytic activity in the thermal decomposition of ammonium perchlorate. *Materials Science-Poland*, 27(2).
- Wang, M., Liu, Q., Sun, H., Stach, E. A., & Xie, J. (2012). Preparation of High Surface Area Nano-Structured Graphene Composites. *ECS Transactions*, 41(22), 95-105.
- Wang, S., Xu, H., Qian, L., Jia, X., Wang, J., Liu, Y., & Tang, W. (2009). CTAB-assisted synthesis and photocatalytic property of CuO hollow microspheres. *Journal of Solid State Chemistry*, 182(5), 1088-1093.
- Wang, W., Zhou, Q., Fei, X., He, Y., Zhang, P., Zhang, G., Peng, L., & Xie, W. (2010). Synthesis of CuO nano- and micro-structures and their Raman spectroscopic studies. *CrystEngComm*, 12(7), 2232-2237.
- Wang, X., Fulvio, P. F., Baker, G. A., Veith, G. M., Unocic, R. R., Mahurin, S. M., Chi, M. F., & Dai, S. (2010). Direct exfoliation of natural graphite into

- micrometre size few layers graphene sheets using ionic liquids. *Chemical Communications*, 46(25), 4487-4489.
- Wang, X., Song, L., Yang, H., Xing, W., Kandola, B., & Hu, Y. (2012). Simultaneous reduction and surface functionalization of graphene oxide with POSS for reducing fire hazards in epoxy composites. *Journal of Materials Chemistry-A-Materials for Energy and Sustainability*, 22(41), 22037.
- Wang, X., You, H., Liu, F., Li, M., Wan, L., Li, S., Li, Q., Xu, Y., Tian, R., & Yu, Z. (2009). Large-Scale Synthesis of Few-Layered Graphene using CVD. *Chemical Vapor Deposition*, 15(1-3), 53-56.
- Wang, X., Zhi, L., & Mullen, K. (2007). Transparent, Conductive Graphene Electrodes for Dye-Sensitized Solar Cells. *Nano Letters*, 8(1), 323-327.
- Wang, Y., Shi, Z. X., & Yin, J. (2011). Facile synthesis of soluble graphene via a green reduction of graphene oxide in tea solution and its biocomposites. *ACS Applied Materials & Interfaces*, 3(4), 1127-1133.
- Williams, G., Seger, B., & Kamat, P. V. (2008). TiO<sub>2</sub>-graphene nanocomposites. UV-assisted photocatalytic reduction of graphene oxide. *Acs Nano*, 2(7), 1487-1491.
- Wu, C.-H., Wang, C.-H., Lee, M.-T., & Chang, J.-K. (2012). Unique Pd/graphene nanocomposites constructed using supercritical fluid for superior electrochemical sensing performance. *Journal of Materials Chemistry*, 22(40), 21466-21471.
- Wu, J., Shen, X., Jiang, L., Wang, K., & Chen, K. (2010). Solvothermal synthesis and characterization of sandwich-like graphene/ZnO nanocomposites. *Applied Surface Science*, 256(9), 2826-2830.
- X**
- Xiang, J., Tu, J., Zhang, L., Zhou, Y., Wang, X., & Shi, S. (2010a). Self-assembled synthesis of hierarchical nanostructured CuO with various morphologies and their application as anodes for lithium ion batteries. *Journal of Power Sources*, 195(1), 313-319.
- Xiang, J., Tu, J., Zhang, L., Zhou, Y., Wang, X., & Shi, S. (2010b). Simple synthesis of surface-modified hierarchical copper oxide spheres with needle-like morphology as anode for lithium ion batteries. *Electrochimica Acta*, 55(5), 1820-1824.
- Xiao, G., Gao, P., Wang, L., Chen, Y., Wang, Y., & Zhang, G. (2011). Ultrasonochemical-assisted synthesis of CuO nanorods with high hydrogen storage ability. *Journal of Nanomaterials*, 2011, 3.
- Xiao, H. M., Fu, S. Y., Zhu, L. P., Li, Y. Q., & Yang, G. (2007). Controlled synthesis and characterization of CuO nanostructures through a facile hydrothermal route in the presence of sodium citrate. *European journal of inorganic chemistry*, 2007(14), 1966-1971.

- Xiao, X., Miao, L., Xu, G., Lu, L., Su, Z., Wang, N., & Tanemura, S. (2011). A facile process to prepare copper oxide thin films as solar selective absorbers. *Applied Surface Science*, 257(24), 10729-10736.
- Xu, C., Wang, X., & Zhu, J. (2008). Graphene– metal particle nanocomposites. *The Journal of Physical Chemistry C*, 112(50), 19841-19845.
- Xu, H., & Suslick, K. S. (2011). Sonochemical preparation of functionalized graphenes. *Journal of the American Chemical Society*, 133(24), 9148-9151.
- Xu, J., Ji, W., Shen, Z., Li, W., Tang, S., Ye, X., Jia, D., & Xin, X. (1999). Raman spectra of CuO nanocrystals. *Journal of Raman spectroscopy*, 30(5), 413-415.
- Xu, L., Sithambaram, S., Zhang, Y., Chen, C. H., Jin, L., Joesten, R., & Suib, S. L. (2009). Novel urchin-like CuO synthesized by a facile reflux method with efficient olefin epoxidation catalytic performance. *Chemistry of Materials*, 21(7), 1253-1259.
- Xu, T., Zhang, L., Cheng, H., & Zhu, Y. (2011). Significantly enhanced photocatalytic performance of ZnO via graphene hybridization and the mechanism study. *Applied Catalysis B: Environmental*, 101(3–4), 382-387.
- Y**
- Yang, C., & Li, S. (2008). Size-dependent raman red shifts of semiconductor nanocrystals. *The Journal of Physical Chemistry B*, 112(45), 14193-14197.
- Yang, H., Li, F., Shan, C., Han, D., Zhang, Q., Niu, L., & Ivaska, A. (2009). Covalent functionalization of chemically converted graphene sheets via silane and its reinforcement. *J. Mater. Chem.*, 19(26), 4632-4638.
- Yang, H., Shan, C., Li, F., Han, D., Zhang, Q., & Niu, L. (2009). Covalent functionalization of polydisperse chemically-converted graphene sheets with amine-terminated ionic liquid. *Chemical Communications*(26), 3880-3882.
- Yang, M., & He, J. (2011). Fine tuning of the morphology of copper oxide nanostructures and their application in ambient degradation of methylene blue. *Journal of colloid and interface science*, 355(1), 15-22.
- Yang, Z., Xu, J., Zhang, W., Liu, A., & Tang, S. (2007). Controlled synthesis of CuO nanostructures by a simple solution route. *Journal of Solid State Chemistry*, 180(4), 1390-1396.
- Yoshida, T., Tochimoto, M., Schlettwein, D., Wöhrle, D., Sugiura, T., & Minoura, H. (1999). Self-assembly of zinc oxide thin films modified with tetrasulfonated metallophthalocyanines by one-step electrodeposition. *Chemistry of materials*, 11(10), 2657-2667.
- Yu, T., Zhao, X., Shen, Z., Wu, Y., & Su, W. (2004). Investigation of individual CuO nanorods by polarized micro-Raman scattering. *Journal of crystal growth*, 268(3), 590-595.

- Yuen, S. M., Ma, C. C. M., & Chiang, C. L. (2008). Silane grafted MWCNT/polyimide composites—Preparation, morphological and electrical properties. *Composites Science and Technology*, 68(14), 2842-2848.
- Yun, Y. S., Bae, Y. H., Kim, D. H., Lee, J. Y., Chin, I.-J., & Jin, H.-J. (2011). Reinforcing effects of adding alkylated graphene oxide to polypropylene. *Carbon*, 49(11), 3553-3559.
- Yusoff, N., Huang, N. M., Muhamad, M. R., Kumar, S. V., Lim, H. N., & Harrison, I. (2013). Hydrothermal synthesis of CuO/functionalized graphene nanocomposites for dye degradation. *Materials Letters*, 93(0), 393-396.
- Z**
- Zaman, S., Zainelabidin, A., Amin, G., Nur, O., & Willander, M. (2012). Efficient catalytic effect of CuO nanostructures on the degradation of organic dyes. *Journal of Physics and Chemistry of Solids*.
- Zhan, R. Z., Chen, J., Deng, S. Z., & Xu, N. S. (2010). Fabrication of gated CuO nanowire field emitter arrays for application in field emission display. *Journal of Vacuum Science & Technology B: Microelectronics and Nanometer Structures*, 28(3), 558-561.
- Zhang, D. D., Zu, S. Z., & Han, B. H. (2009). Inorganic–organic hybrid porous materials based on graphite oxide sheets. *Carbon*, 47(13), 2993-3000.
- Zhang, H., Lv, X., Li, Y., Wang, Y., & Li, J. (2009). P25-Graphene Composite as a High Performance Photocatalyst. *ACS Nano*, 4(1), 380-386.
- Zhang, Q., Liu, S. J., & Yu, S. H. (2008). Recent advances in oriented attachment growth and synthesis of functional materials: concept, evidence, mechanism, and future. *J. Mater. Chem.*, 19(2), 191-207.
- Zhang, W., Wang, H., Yang, Z., & Wang, F. (2007). Promotion of H<sub>2</sub>O<sub>2</sub> decomposition activity over  $\beta$ -MnO<sub>2</sub> nanorod catalysts. *Colloids and Surfaces A: Physicochemical and Engineering Aspects*, 304(1–3), 60-66.
- Zhang, W., Yang, Z., Wang, X., Zhang, Y., Wen, X., & Yang, S. (2006). Large-scale synthesis of  $\beta$ -MnO<sub>2</sub> nanorods and their rapid and efficient catalytic oxidation of methylene blue dye. *Catalysis Communications*, 7(6), 408-412.
- Zhang, Y., Tan, Y. W., Stormer, H. L., & Kim, P. (2005). Experimental observation of the quantum Hall effect and Berry's phase in graphene. *Nature*, 438(7065), 201-204.
- Zhang, Y., Tang, T. T., Girit, C., Hao, Z., Martin, M. C., Zettl, A., Crommie, M. F., Shen, Y. R., & Wang, F. (2009). Direct observation of a widely tunable bandgap in bilayer graphene. *Nature*, 459(7248), 820-823.

- Zhao, J., Pei, S., Ren, W., Gao, L., & Cheng, H. M. (2010). Efficient preparation of large-area graphene oxide sheets for transparent conductive films. *ACS nano*, *4*(9), 5245-5252.
- Zhao, Y., Song, X., Song, Q., & Yin, Z. (2012). A facile route to the synthesis copper oxide/reduced graphene oxide nanocomposites and electrochemical detection of catechol organic pollutant. *CrystEngComm*, *14*(20), 6710-6719.
- Zhou, J., Ma, L., Song, H., Wu, B., & Chen, X. (2011). Durable high-rate performance of CuO hollow nanoparticles/graphene-nanosheet composite anode material for lithium-ion batteries. *Electrochemistry Communications*, *13*(12), 1357-1360.
- Zhou, J., Song, H., Ma, L., & Chen, X. (2011). Magnetite/graphene nanosheet composites: interfacial interaction and its impact on the durable high-rate performance in lithium-ion batteries. *RSC Advances*, *1*(5), 782-791.
- Zhou, K., Wang, R., Xu, B., & Li, Y. (2006). Synthesis, characterization and catalytic properties of CuO nanocrystals with various shapes. *Nanotechnology*, *17*(15), 3939.
- Zhou, K., Zhu, Y., Yang, X., & Li, C. (2010). One-pot preparation of graphene/Fe<sub>3</sub>O<sub>4</sub> composites by a solvothermal reaction. *New Journal of Chemistry*, *34*(12), 2950-2955.
- Zhou, T., Chen, F., Liu, K., Deng, H., Zhang, Q., Feng, J., & Fu, Q. (2010). A simple and efficient method to prepare graphene by reduction of graphite oxide with sodium hydrosulfite. *Nanotechnology*, *22*(4), 045704.
- Zhou, X., Xu, W., Liu, G., Panda, D., & Chen, P. (2009). Size-Dependent Catalytic Activity and Dynamics of Gold Nanoparticles at the Single-Molecule Level. *Journal of the American Chemical Society*, *132*(1), 138-146.
- Zhou, Y., Bao, Q., Tang, L. A. L., Zhong, Y., & Loh, K. P. (2009). Hydrothermal dehydration for the “green” reduction of exfoliated graphene oxide to graphene and demonstration of tunable optical limiting properties. *Chemistry of Materials*, *21*(13), 2950-2956.
- Zhu, J., Bi, H., Wang, Y., Wang, X., Yang, X., & Lu, L. (2008). CuO nanocrystals with controllable shapes grown from solution without any surfactants. *Materials Chemistry and Physics*, *109*(1), 34-38.
- Zhu, J., Wei, S., Ryu, J., Budhathoki, M., Liang, G., & Guo, Z. (2010). In situ stabilized carbon nanofiber (CNF) reinforced epoxy nanocomposites. *Journal of Materials Chemistry*, *20*(23), 4937-4948.
- Zhu, Y., Murali, S., Stoller, M. D., Velamakanni, A., Piner, R. D., & Ruoff, R. S. (2010). Microwave assisted exfoliation and reduction of graphite oxide for ultracapacitors. *Carbon*, *48*(7), 2118-2122.
- Zi, J., Buscher, H., Falter, C., Ludwig, W., Zhang, K., & Xie, X. (1996). Raman shifts in Si nanocrystals. *Applied Physics Letters*, *69*(2), 200-202.

Zou, Y., & Wang, Y. (2011). NiO nanosheets grown on graphene nanosheets as superior anode materials for Li-ion batteries. *Nanoscale*, 3(6), 2615-2620.